Title
Functionalization of Resonant Interactions in Coupled Quantum Dots

Author
Czarnocki, Cyprian Julian

Publication Date
2017

Peer reviewed|Thesis/dissertation

FUNCTIONALIZATION OF RESONANT INTERACTIONS IN COUPLED QUANTUM DOTS

A DISSERTATION
SUBMITTED TO THE SCHOOL OF NATURAL SCIENCES
AND THE COMMITTEE ON GRADUATE STUDIES
OF UNIVERSITY OF CALIFORNIA, MERCED
IN PARTIAL FULFILLMENT OF THE REQUIREMENTS
FOR THE DEGREE OF
DOCTOR OF PHILOSOPHY

by

Cyprian Czarnocki
August 2017

I certify that I have read Cyprian Julian Czarnocki's dissertation and that, in my opinion, it is fully adequate in scope and quality as a dissertation for the degree of Doctor of Philosophy.

(Professor Michael Scheibner) Principal Advisor

I certify that I have read Cyprian Julian Czarnocki's dissertation and that, in my opinion, it is fully adequate in scope and quality as a dissertation for the degree of Doctor of Philosophy.

(Professor Jay E. Sharping) Committee Chair

I certify that I have read Cyprian Julian Czarnocki's dissertation and that, in my opinion, it is fully adequate in scope and quality as a dissertation for the degree of Doctor of Philosophy.

(Professor Sayantani Ghosh)

I certify that I have read Cyprian Julian Czarnocki's dissertation and that, in my opinion, it is fully adequate in scope and quality as a dissertation for the degree of Doctor of Philosophy.

(Professor Tao Ye)

Approved for the University of California, Merced Graduate Studies

_____

Abstract

The focus of this dissertation is discovering and finding functional uses of resonant interactions that occur in coupled quantum dots (i.e. quantum dot molecules, **QDMs**). Coupled quantum dots compared to individual quantum dots offer a more versatile platform to study interactions between photons, charges, and phonons. Applying an electric field in a QDM system allows tuning of the electronic energy states and controls particle tunneling between quantum dots, thus coupling the quantum dots. For the past two decades, extensive research into coupled quantum dot systems has led to a deeper understanding and control of the charge, spin and photonic properties of single quantum states. This dissertation continues the pursuit to further understand these QDM systems with a particular emphasis on exploring the physics of resonant interactions between electronic states, phononic states, and optical transitions. This work consists of three components, the first is a novel experimental method that is capable of achieving high resolution spectra. The second addresses the resonant interaction between discrete neutral exciton and optical phonons that generates a molecular polaron, which can be tuned to render QDM emissions transparent or amplify weak transitions. The final component addresses ultrafast optical charging into specific charge states of a QDM.

In the first research chapter we report on an optical spectroscopy method which is capable of resolving spectral features beyond that of the spin fine structure and homogeneous linewidth of single quantum dots using a standard, easy to use spectrometer setup. This method incorporates both laser and photoluminescence spectroscopy, combining the advantage of laser linewidth limited resolution with multi-channel photoluminescence detection. Using this method allows the ability of greatly improving

the resolution beyond that of a common single stage spectrometer. The method uses phonons to assist in the measurement of the photoluminescence of a single quantum dot after resonant excitation of its ground state transition. The phonons allow us to separate and filter out the elastically scattered excitation laser light. An advantageous feature of this method is that it is easily incorporated into standard spectroscopy set-ups, being accessible to a number of researchers.

In the second research chapter we report on the coherent interaction between photons and phonons mediated by quantum dot molecular excitons. Fano resonances occur between an indirect discrete state and the optical phonon band's continuum of states. This quantum interference is highly tunable with excitation energy and laser power and allows for the phonons to behave in a coherent and non-dissipative manner. This feature has led to rendering QDM optical transitions transparent and can alternately be used to amplify weak coupling channels. This finding, using phonons in a coherent manner, can lead to new technologies in the emerging field of phononics.

In the third research chapter we report on optical charging of quantum dot molecules. The excited state spectra of the neutral and singly charged excitons in QDMs are being studied via photoluminescence excitation spectroscopy (**PLE**). We find an anti-correlated behavior of the resonances in the PLE spectra of different charge states, allowing for selective optical charging of the QDMs. The PLE spectra are analyzed across the regions of resonances between the indirect exciton and excited direct transitions of the low energy dot of the dot pair. The charging process seen in the excited state spectra of the trion and neutral exciton is explained by the competition between various transition rates at the resonance between the two charge states. These distinct resonances are examples of optical charging and de-charging process within the QDM. We present the experimental results and mathematical model describing this charging process.

This dissertation is dedicated to my parents

Acknowledgments

First of all, I would like to thank my adviser Professor Michael Scheibner for his endless support throughout my graduate studies at UC Merced. I feel very grateful for the opportunity to work in his research group over the past 6 years, and it would not be possible for me to write this dissertation without his guidance. I would also like to thank my graduate committee; Chair Professor Jay Sharping, Professor Sayantani Ghosh and Professor Tao Ye, for their helpful guidance, challenging questions and support offered in my journey to becoming a physicist. I would also like to thank our collaborators at the Naval Research Laboratory Dan Gammon, Sam Carter, and Alan Braker and the entire UC Merced Physics department.

I would like to thank my lab mates from the Quantum Matter Group and other friends who made the experience enjoyable and gave me an escape from the lab when I needed it most; above all Dana Burow, Leily Kiani, Mark Kerfoot, Eric Chiu, and Jonathan Boyajian.

And finally I would especially like to thank my family, for their love and encouragement for without them this accomplishment could never have been possible.

Cyprian J. Czarnocki

cczarnocki@ucmerced.edu

EDUCATION

University of California Merced, Merced, CA,
PhD, Physics (2017)
California State University San Marcos, San Marcos, CA,
Bachelor of Science, Physics May 2010
Bachelor of Science, Mathematics May 2010

EXPERIENCE

Graduate Researcher 8/11 - Present
University of California Merced, Physics Department
Merced, CA

- Graduate research focuses on charge, photon, and phonon interactions in self-assembled quantum dot molecules.
- Designed and built experimental optical set-ups at the Quantum Matter Group lab.
- Extensive experience in data collection and data analysis using both Python and Matlab.
- Advised 6 undergraduate students with their undergraduate thesis research.

Visiting Graduate Researcher 5/15 - 8/15
Naval Research Laboratory
Washington, DC

- Introduced to sample fabrication of quantum dot molecules embedded in mechanical resonators. Growth via molecular beam epitaxy, patterning with electron beam lithography and wet-chemical etching.
- Conducted optical spectroscopy for sample characterization and time correlated single photon counting experiments.

Teaching Assistant 8/11 - 5/16
University of California Merced, Physics Department
Merced, CA

- Physics 8, Introductory calculus based mechanics
- Physics 19, Introductory calculus based electromagnetism and optics for pre-medical and biosciences students
- Physics 9, Calculus based electromagnetism and optics for physics and engineering students
- Introduction to Astronomy, Introductory astronomy course for non-science majors
- Physics 9 Honors, Introductory calculus based mechanics

Interim Laboratory Instructor 3/11 - 5/11
California State University San Marcos Physics Department
San Marcos, CA

Instructional Laboratory Technician & Teaching Assistant 1/11 - 5/11
CSU San Marcos Physics Department

San Marcos, CA

- Assist instructor with digital electronics course; grading and helping students with their coursework and projects
- Responsible for managing laboratory equipment used in the undergraduate physics program
- Assist in facilitation of laboratories and implementation of proper laboratory practices among students

Undergraduate Research Assistant 5/8 -11/10
CSU San Marcos Applied Hydrodynamics and Plasma Physics Laboratory
San Marcos, CA

- Developed protocol and improved plasma experimental apparatus; played integral role in testing and troubleshooting the vacuum/pneumatic system and custom high voltage AC power supply.
- Employed Matlab for analyzing both fluid turbulence and RF driven plasma structures; implementing statistics, data analysis, and image processing

Mathematics Tutor 5/06 - 5/10
CSU San Marcos Mathematics Laboratory
San Marcos, CA

- Tutored students in mathematics from beginning algebra to multivariable calculus, instilling in them the importance of a mathematical foundation and good problem solving skills

Undergraduate Research Assistant 5/09 - 8/09
Princeton Plasma Physics Laboratory (PPPL)
Princeton, NJ

- Installed Miranov Coil Arrays within the Princeton Magneto-Rotational Instability (MRI) Experiment implemented to measure magnetic field fluctuations
- Analyzed Ekman Circulation; using a Laser Doppler Velocimeter (LDV) and Python to analyze the data
- Assisted with the design and construction of the plasma globe apparatus (see 2009 DPP Conference)

Learning Assistant 9/08 - 5/09
California State University San Marcos Physics Department
San Marcos, CA

- Assisted students in solving physics problems; provided conceptual and mathematical insight, encouraged teamwork and effective problem-solving techniques, assisted instructors with educational research

PUBLICATIONS

- C. Czarnocki, M.L. Kerfoot, J. Casara, A. Jacobs, C. Jennings, M. Scheibner, High Resolution Phonon-Assisted Quasi-Resonance Fluorescence Spectroscopy, *JoVE*, 2016, Vol. 112 doi: 10.3791/53719
- M.L. Kerfoot, A.O. Govorov, C. Czarnocki, D. Lu, Y. Gad, A.S. Bracker, D. Gammon, M. Scheibner. Optophononics with coupled quantum dots. *Nature Communications*, 2014, Vol. 5, 3299
- M.J. Burin, C. Czarnocki. Subcritical transition and spiral turbulence in circular Couette flow. *Journal of Fluid Mechanics*, 2012, Vol. 709, pp. 106-122.

Invited Talk

- *Optophononics with Coupled Quantum Dots.* Frontiers in Science Seminar, California State University San Marcos April 2017

PRESENTATIONS

- S. Carter, A. Bracker, M. Kim, C.S. Kim, M. Zalalutdinov, B. Pursley, S. Economou, C. Czarnocki, C. Jennings, M. Scheibner, D. Gammon, *Coupling a single InAs quantum dot to mechanical motion of a photonic crystal membrane*
  APS March Meeting, Baltimore, Maryland March 2016

- C. Czarnocki, C. Jennings, M.L. Kerfoot, J. Casara, A. Jacobs, A.S. Bracker, S. Carter, D. Gammon, M. Scheibner *Phonon and Strain Measurements for Quantum Enhanced Motion Sensing Using Entangled Spins in Quantum Dots*
  DTRA Basic Research Technical Review, Ft. Belvoir, Virginia July 2015

- C. Czarnocki, M.L. Kerfoot, A.S. Bracker, D. Gammon, M. Scheibner *0-D to 2-D Transitions in Epitaxially Grown Quantum Dot Pairs* Electronics Material Conference, Materials Research Society June 2014

- C. Czarnocki, M.L. Kerfoot, A.S. Bracker, D. Gammon, M. Scheibner *0D to 2D Transitions in Stranski-Krastanov Quantum Dots*
  APS March Meeting, Denver, Colorado March 2014

- C. Czarnocki, M.J. Burin *Characterization of RF-driven Plasma Filaments in a Plasma Globe*
  American Physical Societies 52nd Division of Plasma Physics Meeting, Chicago, Illinois Nov. 2010

- M.J. Burin, C. Czarnocki, T. DaPron, K.R. McDonald *Subcritical Transition and Spiral Turbulence in Taylor-Couette Flow*
  APS 63rd Division of Fluid Dynamics Conference Nov. 2010

- C. Czarnocki, P. Humanik , A. Roach , M. Nornberg , E. Spence , M. Burin , H. Ji *Experimental Characterization of Azimuthal Velocity with Varying Reynolds Numbers in short Taylor-Couette Flow*
  APS 51st Division of Plasma Physics Conference, Atlanta, Georgia Nov. 2009

- C. Czarnocki, M.J. Burin *Experimental Characterization of Velocity Variations within a Rotating Fluid*
  Southern California Conference for Undergraduate Research, Dominguez Hills, CA Nov. 2009

- C. Czarnocki, M.J. Burin *Experimental Characterization of Velocity Variations within a Rotating Fluid*
  CSU San Marcos, Frontiers of Science Seminar, San Marcos, CA Sept. 2009

AFFILIATIONS

- Member, Materials Research Society

- Member, Optical Society of America

- Treasurer & Vice President (2012 - 2015), UC Merced Chapter Optical Society of America
- Member, Sigma Pi Sigma
- Member, American Physical Society
- College Reading and Learning Association
- Vice-President & Secretary (2008 - 2010), CSU San Marcos Chapter Society of Physics Students

SKILLS

- Research experience with optical spectroscopy(ultrafast spectroscopy, single-molecule spectroscopy, atomic force microscopy, scanning tunneling microscopy, vacuum technology, cryogenics and control systems
- In-depth knowledge of NI Labview, MATLAB, Python
- Experience in technical writing and research presentations
- Leadership and project management experience in academics and in the work place

COMPUTER SKILLS

Languages & Software: MATLAB and Simulink, C/C++, PYTHON, NI LabVIEW, LaTeX, MultiSim, Maple, Mathematica,
Operating Systems: Linux (Ubuntu), Mac OS X, Windows

REFERENCES

Available Upon Request

Contents

List of Figures

Chapter 1

Introduction

Over the past few decades, technology has enabled the miniaturization of devices. Since the invention of the semiconductor transistor, miniaturization has followed Moore's law, which states that every 18 months the number of transistors per integrated circuit doubles as does the circuit's computational power. [1] We are now able to build structures at the nanometer length scale. When electrons (or holes) are confined to such small regions (on the order of the De Broglie wavelength) it leads to quantum-mechanical effects such as discrete energy spectra and wavelike interference among the charged particles. Quantum dots (QDs) are structures wherein charge carriers are confined in three spatial dimensions so that the device exhibits such quantum-mechanical effects. Due to their quantum mechanical properties quantum dots hold a great promise for a number of new technologies. Since Bell's theorem proved that quantum properties are real and can be harnessed for a variety of real world applications. Quantum technologies are currently being used; from ultra-precise atomic clocks, uncrackable quantum key distribution, super-powerful quantum computers, and improved entanglement enhanced microscopes. [2] [3] [4] [5]

Ongoing research is highly motivated to incorporate these tiny systems for practical applications. These microscopic systems exhibit useful properties that can be exploited, such as quantum coherence, where elementary particles with their wave like behaviors can interfere due to the coherent nature of their wave functions leading to novel macroscopic phenomenas. Another property that of quantum entanglement,

where two elementary particles can form an entangled state where it is very difficult to describe the state of each particle individually. By measuring a property of one of the particles leads to the other particle having properties that exactly mirror that of the first, even though their is no physically observed link. These two properties provide the fundamentals that are leading the way for these quantum enhanced technologies.

The potential of quantum enhanced technologies is most evident in the field of information technologies. In these new systems quantum mechanics defines the fundamental limits of their performance. For example, in quantum computation, interference between different processing pathways will drive future computers to solutions more quickly than with today's fastest algorithms. [6] Another example is quantum cryptography where quantum dot generated photons act as excellent information carriers over long distance and can be employed with a cryptographic key that is guaranteed by fundamental laws of physics. [7]

QDs have been a highly active area of research for the past few decades. QDs were first discovered by Louis E. Brus while he was researching at AT& T Bell Laboratories. He referred to his discovery as 'small semiconductor crystallites'. [8] It was not until the early 1990's that self-assembled QDs were fabricated. [9] [10] Self-assembled QDs are different from the QDs that Brus discovered in the sense that they are assembled and exist locked within a crystal matrix. The distinction between the different QDs will be addressed in chapter 2. On the individual level, a single QD is well understood by its discrete level structure that give it the nickname of 'artificial atom'. Over the last three decades research has studied the optical properties of QDs and their interactions and response at varying temperature, electric, and magnetic fields. [11] [12] [13]

My dissertation's focus is within this quantum realm and focuses on research into the semiconductor nanostructures of coupled quantum dots (CQD), also called quantum dot molecules (QDM). QD research reaches into various branches of physics, from harvesting energy from the sun, to improving display technologies, they also hold great potential to emerging fields in quantum computing and quantum cryptography. My research's goal is to continue to grow our understanding of these QDM systems, with a common theme of my research being the investigation of resonant interactions between

different electronic states, phononic states, and optical transitions. [14] [15] [10] [16] Throughout the dissertation presentation of the physical concepts that are most relevant to the work will be presented. The work draws from concepts throughout physics from quantum mechanics, condensed matter, atomic, molecular, and optical physics (AMO), classical electrodynamics and electronics. Prevailing as the foundation of the research of QDs is by far quantum mechanics. From the concepts of energy level quantization to Pauli's exclusion principle these quantum concepts rule the behavior of charge carriers in the QD. An outline of the work is provided below.

Chapter 2 introduces the background material to the topics covered throughout this dissertation. It begins by giving an introduction to semiconductors and band theory. Leading to quantum confinement effects that occur as charge carriers are confined to one, two and three dimensions, respectively describing quantum wells, quantum wires and finally QDs. Then a description of QDs and their fabrication methods is given. The effect of temperature, lattice vibrations and phonons are also discussed. The chapter then closes with the application of QDs, along with recent research results.

Chapter 3 covers the experimental methods used for this dissertation. From equipment necessary to cool and focus the sample, to the laser excitation path and the detection path is explained. Then the two main experimental methods; photoluminescence and photoluminescence excitation spectroscopy are covered.

The next chapter dives into the first research topic; an experimental method we termed phonon-assisted quasi-resonant fluorescence. [17] The experimental method describes a technique where a discrete state is resonantly excited. By monitoring the spectra an LO phonon's energy below the excitation leads to very high resolution spectra. This allows for us to combine the added benefits of both laser and photoluminescence spectroscopy by being able to resonantly excite through a specific discrete transition and observe the -1 LO photon emission since the emission is only visible when at resonance with the transition. This method employs optical filters to separate the elastically scattered laser light from the detection. The method offers resolutions of better than 1 μeV and can be incorporate in any standard spectroscopy setup.

Chapter 5 begins with an introduction to Fano interference, which is a quantum interference effect between a discrete state and a continuum of states. In the QDM Fano interferences arise when an indirect discrete state is in resonance with the optical phonon band. At these locations we realize the formation of a molecular polaron due to the Fano interference making the phonons non-dissipative and coherent. Experimentally we show that this interference can produce a phonon transparency that can effectively turn off our discrete state. On the other hand the interference can be used to amplify very weak channels.

The following chapter covers optical charging. It has been observed that when different charge states come into resonance interesting charging behaviors occur that lead to the charging of a single charge's ground state. We show that this charging is due to the metastability of the charge states and the optical fields driving power. We report on the experimental results and mathematical rate equation that explains this charging process.

The final chapter summarizes and concludes the dissertation. Also giving a direction for future research.

Chapter 2

Background

This chapter provides the background material to the research presented. The main purpose is to garner an understanding in quantum and condensed matter physics in regards to photon, phonon, and charge interactions within coupled QDs. This basis of knowledge will be helpful to understand and interpret the results of the following chapters and in understanding the various resonant interactions between different states.

2.1 Semiconductor Physics

In order to understand semiconductor physics one must learn about the band theory of solids. [18] It describes how electrons in a crystal with a periodic potential have Bloch wave functions. [19] These wave functions create forbidden regions that make up their band structure. Consider bringing two atoms together so that their wave functions combine to form bonding and anti-bonding orbitals. When the number of atoms increases their atomic orbitals form bands due to the Pauli's exclusion principle. Conductors have overlapping conduction and valence bands that allow for electrons to freely move, where as insulators have much larger band gaps than semiconductors. Figure 2.1 show the alignment of the bands for insulators, semiconductors, and metals. Semiconductor materials have properties between that of insulators and conductors. The most common types of semiconductor materials come from the elements found

in group IV of the periodic table or compounds of the group III-V or II-VI elements. [18] [19] [20]

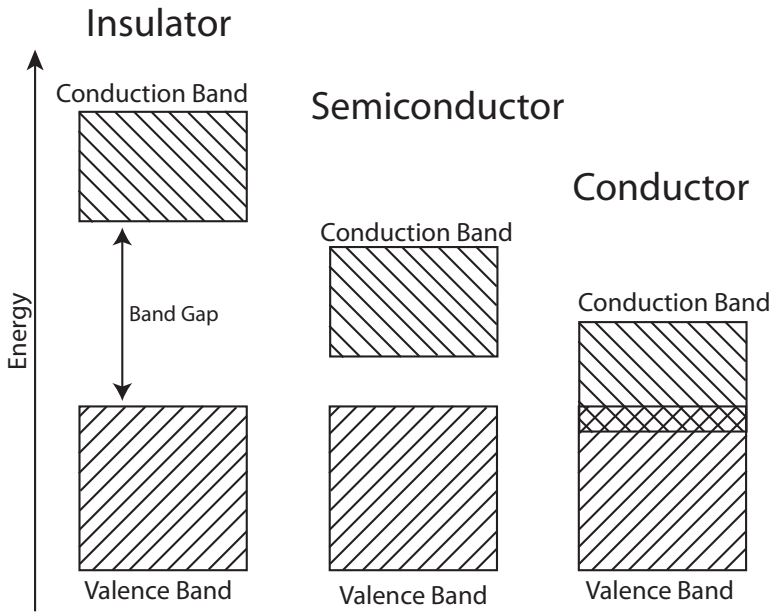

Figure 2.1: Schematic of energy bands for an insulator, a semiconductor, and a conductor.

Each different semiconductor has a specific band gap for the specific material. A semiconductor's band gap is less than 4 meV. The semiconductors InAs and GaAs used in the research presented in this dissertation have band gaps of 0.43 meV and 1.424 meV at 300 K respectively. [21] [22] At low temperatures these semiconductors are non-conducting with all the electrons in the valence band of the material. [23] When a photon with energy of equal or greater value than the band gap interacts with the system, it lifts an electron out of the valence band and into the conduction band. Thus leaving behind a missing electron in the valence band. This deficit of electron can be viewed as a quasiparticle and is referred to as a hole.

In order to understand how these electrons and holes occupy valence and conduction bands it is necessary to consider that both are fermions with spin of 1/2, and are governed by the Pauli's exclusion principle dictating that no two particles can fill the same quantum state. [24] [25] Fermions such as electrons and holes are governed

by the Fermi-Dirac distribution:

$$\bar{n}_i = \frac{1}{e^{\frac{\varepsilon_i - \mu}{kT}} + 1} \tag{2.1}$$

where k is the Boltzmann's constant, T is the temperature. ε_i is the energy for the state i, and μ is the total chemical potential. At low temperatures μ is equal to the Fermi energy. In semiconductors the Fermi energy lies between the conduction and valence bands. [18]

2.2 Quantum Confinement

The confinement properties are well understood. The most basic situation where confinement arises is for a 0D confinement of a particle in a box, this being the simplest model of a quantum dot. The potential is defined as

$$U(\mathbf{r}) = \begin{cases} 0, & \text{if x,y,z are between 0 and L} \\ \infty, & \text{otherwise} \end{cases}$$

The solution for the potential leads to the solutions of the stationary states are:

$$\psi_{n_x,n_y,n_z}(r) = \sqrt{\frac{8}{L^3}} sin(\frac{n_x \pi x}{L}) sin(\frac{n_y \pi y}{L}) sin(\frac{n_z \pi z}{L}) \tag{2.2}$$

$$\varepsilon_{n_x,n_y,n_z} = \frac{\pi^2 \hbar^2}{2 m_{eff} L^2} (n_x^2 + n_y^2 + n_z^2) \tag{2.3}$$

where the n_x, n_y, and n_z are the quantum number that are associated to the confinement of that particular dimension. The m_{eff} corresponds to the particles effective mass. The significance of this solution is that it leads to discrete energy levels and the quantization of the confinement energies $\varepsilon_{n_x,n_y,n_z}$ increases with a decreasing well width. This occurs for all three dimensions, as the size decreases and restricts the charge carriers to a confined region, a distinct set of energy levels (i.e. quantization) occurs. This leads to the atom-like density of states.

2.2.1 Density of States

The density of states is defined as the number of available states per unit volume of the semiconductor. Calculating the density of states for semiconductors is important in bulk material this is defined as

$$g(k)dk = (\frac{V}{2\pi^2})k^2dk \tag{2.4}$$

in reciprocal space (k-space); where V is defined as the volume, m is the effective mass of the particles, either electrons or holes, and E is the energy. In energy space the density of states is:

$$g(E)dE = (\frac{1}{2\pi^2})(\frac{2m}{\hbar^2})^{\frac{3}{2}}E^{\frac{1}{2}}dE \tag{2.5}$$

Interesting physics occurs as we head toward lower dimensionality.

2.2.2 Quantum Wells

Starting with a bulk semiconductor and confinement in a single dimension leads to a quantum well. Quantum wells have been extensively researched for the last half century. A quantum well is defined as an object where charges are only free to move in two dimensions. The confinement of a quantum well as a first order approximation can be the commonplace result of the particle in a box where:

$$E_n = \frac{\hbar^2\pi^2n^2}{2m^*L^2} \tag{2.6}$$

where n is the states energy level. This gives us the various energy levels where we use the effective mass (m^*) [1] and L is the size of the box. This defines a quantum well and the density of states of a quantum well is defined as:

$$g(E)dE = (\frac{m^*}{\pi\hbar})^{1/2}dE \tag{2.7}$$

[1]The effective mass of a semiconductor is obtained by fitting the dispersion relation around the conduction band minimum or valence band maximum. The effective mass may differ significantly from the free electron/hole mass.

Quantum wells have found their place in many modern technological devices such as optical detectors, thermoelectric and even in lasers.

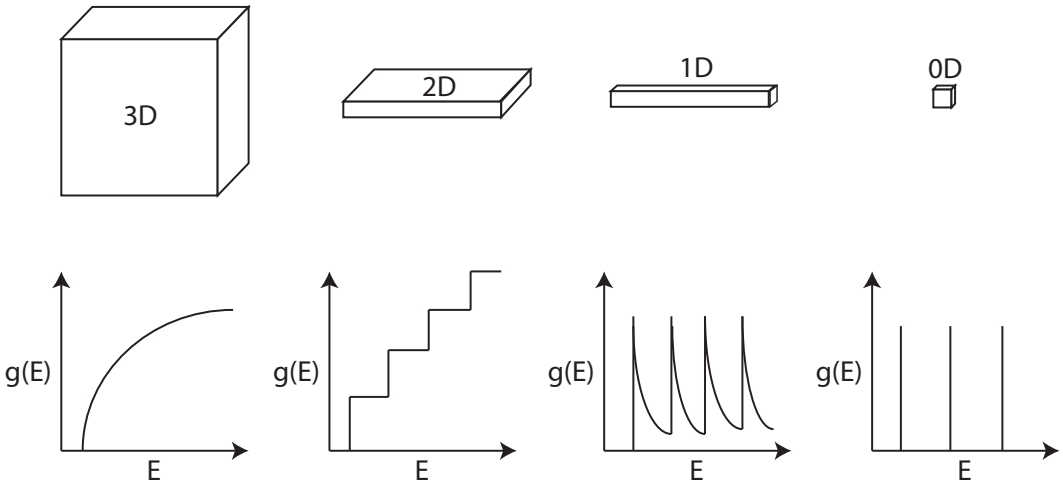

Figure 2.2: Density of states for bulk , 2D, 1D and 0D geometries.

2.2.3 Quantum Wires

From the quantum well if we add another level of confinement we achieve a material that is confined in two dimensions. We call such a material a quantum wire or nano wire. This can be modeled by two dimensional wells, and offer very interesting properties such as quantized conductivity if the size of the wire is much smaller than the mean free path leading them to being non-ohmic. [26] This leads to the charges being confined in one dimension an expression for their density of states is:

$$g(E)dE = (\frac{1}{\pi})(\frac{2m}{E\hbar^2})^{\frac{1}{2}}dE \tag{2.8}$$

Quantum wires have found application in electronics in particular they have been found as great options as transistors and have great potential in being incorporated into electronic devices. [27] They also have found application in optical devices. [28]

2.3 Quantum Dots

Quantum dots (QDs) are man-made nanostructures that are often referred to as artificial atoms. They are often called artificial atoms due to their discrete energy level structure that is reminiscent of atom-like spectra. [29] This analogy is due to the charge carriers being confined in three-dimensions, hence they are called zero-dimensional due to the minuscule region of space that is comparable to the exciton Bohr radius. Their electronic characteristics are closely correlated to the size and shape of the individual crystal, and the inverse relation between physical size and quantum confinement enables them to be fabricated with customized energy level spacing.

Figure 2.3 shows that this confinement can be modeled with a band gap diagram where the charge is confined in three dimensions due to the use of two semiconductor materials that have different materials. If a material of smaller band gap is sandwich between a material of larger band gap then we create a potential trap for charge carriers as depicted in figure 2.3. With the discrete energies the density of states of a QD is denoted with the delta function.

$$g(E)_{0D} = 2\delta(E - E_c) \tag{2.9}$$

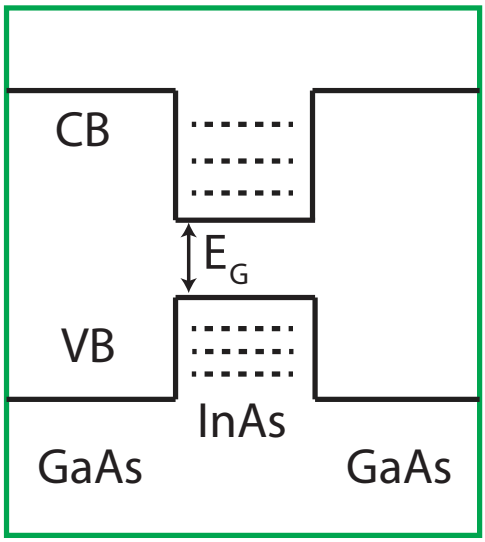

Figure 2.3: Energy Band Schematic for a Single Quantum Dot

QDs have nanometer size in all three dimensions, the dimensions of a QD range from 2 to 100 nm. The number of atoms a QD is made up of ranges from 10^3 to 10^6. The confinement of a QD can be simply modeled with the particle in a box in equation 2.3 another popular way to model a QD is with a harmonic oscillator potential in all three dimensions with the following Hamiltonian:

$$\bar{H} = \frac{p^2}{2m} + \sum_{1}^{3} \frac{1}{2} m\omega_0^2 r_i^2 \tag{2.10}$$

With the oscillator being in three dimensions sets the dimensionality parameter, r is the size of the dot in the z direction and m is the effective mass of the electron or hole within the material. The eigenenergies are given by:

$$E_n = (n + 3/2)\hbar\omega_0 \tag{2.11}$$

This is one of the many models that one can solve for the energy eigenvalues; there are other more accurate models that take into account the actual geometry of the QDs. Other potential models can be used such as a particle in a cone, [9] particle in a pyramid, [30] and particle in a parabolic potential [31]. Even though these different potentials each are a more accurate representation of QDs, it is important

to note that real QDs are more complicated due to their slight variations in size and atom configuration. [32] These ever so small discrepancies lead to variations in their energy levels.

All of these potentials are due to the spatial confinement that leads to quantization and gives discrete energy levels. This can be compared to that of the excitonic Bohr radius, that is defined by the separation between the electron and hole. Semiconductors QDs are often favored for their larger size that makes them easier to fabricate and control. For QDs the density of states has the form of delta like functions. Compared to the higher dimensional structures mentioned before; bulk, quantum wells, and quantum wires all have continuous density of states in their unconfined dimensions, which leads to them having a continuous absorption unlike QDs that have discrete spectra. QD emission line widths compared to that of real atoms are a few orders of magnitude larger due to the QDs shorter lifetime. The shorter lifetime in QDs can be due to mechanisms such as phonon interactions that are non-existent in atoms.

QDs due to the spatial confinement have distinct spectral emissions. As a photon excites an electron from the valence band it leaves behind a hole. The electron and hole within a QD are Coulomb bound and the electron-hole pair or exciton is responsible for the QD's emission spectrum. The exciton's relaxation in the QD is very quick occurring in the time span of a few picoseconds leaving most electrons in the ground state prior to radiative recombination. Interestingly due to the small inhomogeneities in the dot size with a QD ensemble this leads to spectrum broadening. Other sources of broadening exist, such as thermal, electric field fluctuations, and strain. In a large ensemble the broadening of the order of 50 meV obscures other effects such as multiple excitons in the QDs and charging effects that are normally on the order of 10meV. Thus to study individual QDs a few techniques must be employed, special growth steps must be taken to prepare a low density sample and/or an aperture mask must be employed to optically excite individual QDs. These QDs at low temperature have line widths of a few μeV.

2.3.1 Types of Quantum Dots

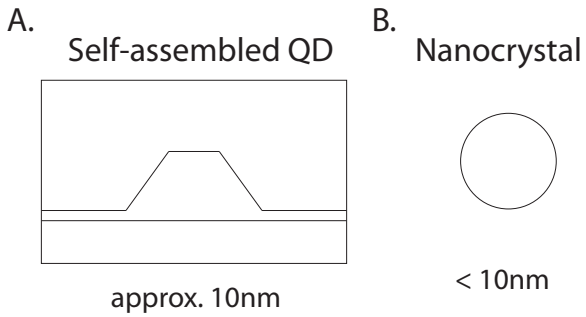

Figure 2.4: Schematic of Quantum Dots, A) Self-assembled QD, grown within a crystal matrix with an associated wetting layer trapezoidal in shape B) Colloidal QDs are nano crystals with a core and shell and are spherical in shape. Both types of QDs energy spectrum is governed by semiconductor type and size.

There are three major types of QDs; colloidal QDs, electrostatically defined QDs, and self-assembled QDs. All three of these QDs though similar with their discrete energy levels from the confinement of charge carriers are still quite different in fabrication and makeup. The schematic for two of the QDs is portrayed in figure 2.4.

2.3.2 Colloidal QDs

Colloidal QDs are chemically synthesized; they are formed from chemical solutions, where the reaction neither precipitates a solid nor remains dissolved. Thus creating these nanocrystals. [33] [34]

Colloidal quantum dots are grown by the quick addition of reagents in a very hot solvent. When the reagents are added and the temperature of the solvent is hot enough then the reagents decompose resulting in supersaturation that nucleates the nanocrystals. [35] The method is best used for II-VI semiconductors due to their ability to easily crystallize. For III-V the configurations are covalent thus leading to very large energies to crystallize. [36] The size of the colloidal quantum dots is controlled by parameters of the experiment such as the time, temperature and concentration of reagents. Large QDs are grown by increasing the temperature and reaction time of the reaction. [37]

2.3.3 Electrostatically defined QDs

These QDs are fabricated by electron beam lithography. Starting with a doped quantum well the electron or hole gas can be formed. Then the surface of the sample is coated with a photo resist. Electron beam lithography is used to pattern the resist. The pattern can then be transferred onto the electron or hole gas or it can be used for the deposition of electrodes. [38] The electrodes are used to apply a voltage potential that can trap charge carriers in a zero-dimensional trap. Electrostatically defined QDs are often used to study charge phenomena such as charge transport. [39]

2.3.4 Self-assembled QDs

The QDs studied here are formed by an epitaxial process in self assembling fashion. This entails building the QD from the ground up. There are two main ways to make QDs using this method, the first is metalorganic chemical vapor deposition (MOCVD). This epitaxial growth method is used to grow semiconductor thin films from the surface reactions of metal organics and hydrides. It is a highly complicated process that grows crystals by chemical reaction not by physical deposition. The reactions occur at high temperatures above the surface of the substrate. This technique unlike others is not done in vacuum pyrolysis occurs at pressures ranging from 10 to 760 Torr. Using this growth process it is possible to grow QDs, but it is not a primary growth technique as it is most commonly used for fabricating thin films. [36]

The main method for producing self-assembled quantum dots is by molecular beam epitaxy (MBE). MBE was first developed in Bell Laboratories in the late 1960's by J.R. Arthur and A.Y. Cho. [40] MBE is done at ultra high vacuum where growth on a substrate is gained by slow deposition of atoms. Atom layer resolution is achievable with rates ranging from 0.001 and 0.3 micrometers per minute. [41] Effusion cells contain pure elements like In, Ga, and As. Each individual effusion cell can be heated individually by heating a filament and using it to evaporate the desired material. This material is then deposited on the substrate wafer where it is left to react and condenses at the substrate.

The growth of the atom layers is monitored by reflection high energy electron

diffraction (RHEED). When the surface of the material is smooth the pattern produces a pattern of lines. But when QD's are formed a rough surface produces a RHEED pattern of dots. Monitoring of the RHEED pattern is then readout at the computer in a feedback loop to control the shutters of the effusion cells. [42]

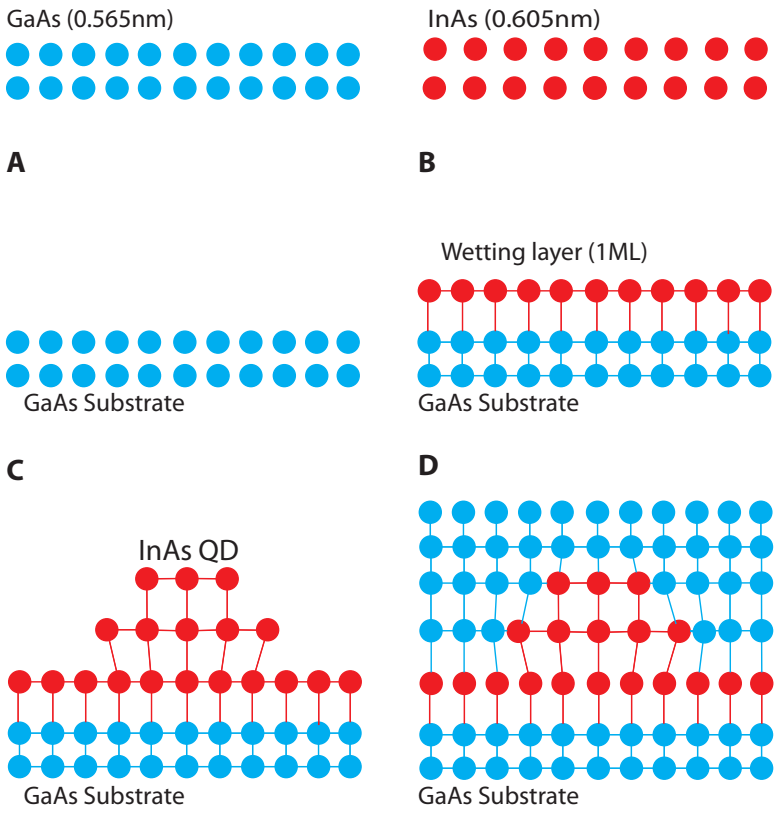

Figure 2.5: Schematic of QD Growth model, A) starting with GaAs substrate, B) first InAs layer is deposited on the GaAs called the wetting layer, C) with added InAs leads to nucleation of a QD, D) the InAs QD is then capped with GaAs.

There are three main growth modes using MBE. They are Frank-van der Merwe, Volmer-Weber, and Stranski-Krastanov (SK). The first Frank-van der Merwe mode grows atom layer by atom layer with the resulting surface being atomically smooth thin layers due to the atoms attaching preferentially to substrate surface sites. The second growth mode is the Volmer-Weber growth were the added atoms have a stronger interaction between each other and this leads to clusters and islands on the substrate surface. And the final mode that is a combination of the layer and

island formation is the Stranski-Krastanov mode. In SK mode, initial atoms are deposited layer by layer on the substrate until reaching a critical layer thickness. At this specific thickness the nucleation of the islands occurs. [43] [44] The SK growth mode is currently the most popular way to make self-assembled dots.

2.3.5 Quantum Dot Molecules

After the discovery of the QD and garnering a basic understanding of QDs, researchers next step was to scale the system up. This lead to creation of coupled QDs creating a quantum dot molecule (QDM). Research has shown the controlled coupling of these stacked QDs via Coulomb related interactions such as the dipole-dipole interaction, resonant Förster transfer process and via tunneling process whereby electron or hole or both can move from one dot to the other. [45] [46] [47] These processes are governed by properties of the given QD system, the individual dot parameters, similarity of dots, and inter-dot barrier properties. The tunnel coupling between the two dots can be mediated either by the size of the QDs and by the application of an externally applied electric field. This electric field is created by placing the QDs in a diode like structure. These properties are then optically studied by using photoluminescence (PL) spectroscopy. Using an excitation laser to generate the electrons and holes in the conduction and valence bands, the recombination of these charge carriers then produces the PL spectra displaying the energy levels of the QDM.

A QDM is formed by having two or more QDs in close proximity; the QDs share charge carriers. Similar to that of an actual molecule. Atoms can bond covalently when each atom equally shares the electron or an ionic bond where a complete transfer of the valence electrons occurs. The proposed study of quantum coupling between QDs is fundamental and analogous to that of real atoms, to produce artificial molecules, or even to produce artificial solids [29]. Coupling QDs can be achieved via either having two QDs that have been grown in close proximity with each other (laterally), or grown by adding a second QD layer atop the previous self-assembled QDs (vertically). The schematic of the QDMs and the corresponding band diagram is depicted in figure 2.6.

Some QDM research has focused on coupling laterally positioned QDs. Similarly to vertical the QDs coupling should be possible and could similarly be achieved via placing electrodes between the two dots. One issue with lateral QDMs is that due to the flat shape of SK QDs the coupling may radically differ from vertical QDMs. [48] [49] Theoretical work has calculated PL of a laterally coupled QDMs. [50] Though experimentally not many reportings of lateral coupling have been presented. [48] But one paper in particular has shown that similar to vertical QDMs there has been a report that due to a Stark shift by applying a lateral electric field that emission lines where due to either recombination in one or the other QD. [50]

Though lateral coupled QDs pose interesting research questions the focus for this dissertation and all research presented was performed on vertically grown self-assembled QDMs.

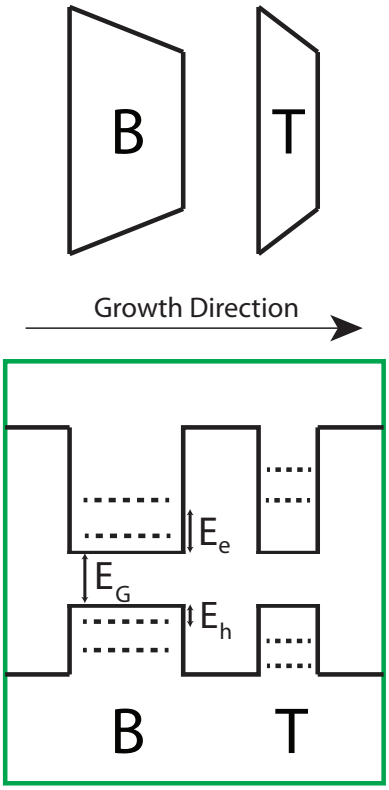

Figure 2.6: Energy Band Schematic for a Quantum Dot Molecule

The QDMs are composed of GaAs and InAs that have band gap energies of 1.42

eV and 0.35 eV respectively. [21] [22] The samples studied were fabricated by our collaborators at the United States Naval Research Laboratory (NRL). The samples where grown via molecular beam epitaxy using the Stranski-Krastanov growth mode. The sample is grown on a GaAs substrate. Growth of the InAs QDs occurs due to the lattice mismatch between GaAs and InAs. GaAs has a lattice constant of $5.65\mathring{A}$ and InAs has a lattice constant of $6.05\mathring{A}$. As the InAs is deposited the first layer formed is called the wetting layer and evenly distributes over the GaAs substrate. When this wetting layer reaches a critical height around 1 ML the nucleation of the InAs QDs begins to alleviate the strain caused by the lattice mismatch. Figure 2.5 demonstrates this process. The dot layer is grown with density gradients, which is achieved by interrupting the wafer rotation during the respective molecular beam epitaxy growth steps. The density of the QDs in the region of the wafer where the samples were taken from was 10^8 and 10^9 cm^{-2}.

The heights of the dots were controlled by the indium flush technique. [51] [52] [53] For this technique capping of the dots with GaAs is interrupted at a layer that defines the desired height. Then the temperature is raised allowing the exposed InAs to redistribute and evaporate before the regular growth of the GaAs barrier is continued. For the generation of a QDM this process is repeated. Due to the remnant strain field generated by growth of the first QD the second QD preferentially grows directly above the bottom QD. The thickness of the GaAs between the two QDs governs the charge carriers tunneling between the QDs. The height of dots in both layers was nominally set to 2.5 nm. Dots in the second layer were found to exhibit higher band gaps than dots in the first layer, which is attributed to large lateral growth of dots in the second layer causing a different evolution of dots during the indium flush. For the QDMs that are discussed throughout the dissertation they had either a 4nm, 6nm, or 8nm GaAs tunnel barrier.

Additional steps can be taken to grow the QDs in more defined locations. One such technique is patterning the GaAs substrate prior to growth with nanoholes. These nanoholes act as a favorable location for the growth of the QDs. This allows for much more accurate positioning. [54]

The full sequence of layers deposited on top of the GaAs substrate was 500nm n+

GaAs buffer, 80nm i-GaAs, 2.5nm InAs QDS, 2, 4, or 6nm GaAs barrier, 2.5nm InAs QDs, 230nm GaAs, 40nm AlGaAs, 10nm GaAs, 8nm titanium and 120nm aluminum. The schematic of the samples layer sequence is represented in figure 2.7.

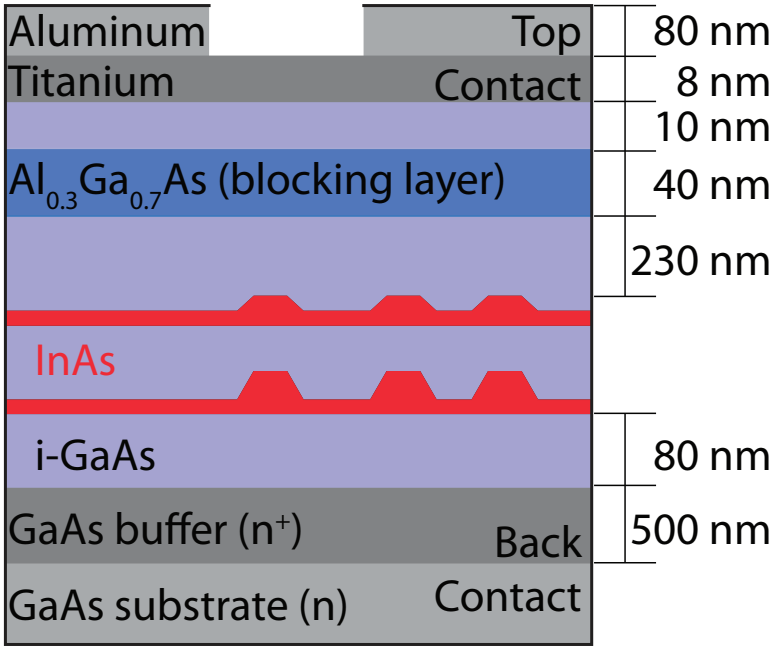

Figure 2.7: Schematic of the QDM sample structure

As mentioned, the density of these QDMs on the sample is 10^8 to $10^9 cm^{-2}$ this makes optical excitation of a single QDM a challenge depending on the focal spot size of the excitation laser. To eliminate the excitation of multiple QDMs an aperture mask was placed over the sample the mask has $1\mu m$ sized apertures. The aluminum aperture masks offers two advantages the first is excitation of individual QDMs becomes possible and secondly the aperture mask can be marked in a grid like fashion to allow for finding a specific QDM repeatable. Figure 2.8 shows a aperture map that was placed on some of the samples.

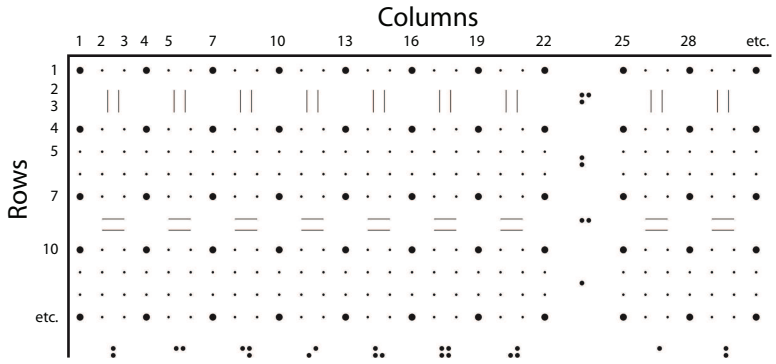

Figure 2.8: Schematic of the Aperture Mask that makes optically addressing a single QDM a possibility

2.4 Schottky Diode

The QDM are embedded in a Schottky diode structure to allow for electric field control of the QDM's states. The n-i Schottky diode is made up of the n+ GaAs buffer and the titanium contact layer. These contact layers provide an electric field in the growth direction when a bias is applied. A blocking layer exists in the growth structure, this layer is the $Al_{0.3}Ga_{0.7}As$ which has a large band gap and prevents charges to tunnel to the metal contacts.

The Schottky diode operates in two modes; in forward bias charge is allowed to freely pass through the material as a current runs through the device. In the reverse bias direction a current does not flow but a controllable electric field is applied. Figure 2.9 at the positive biases when the Schottky diode is in Forward bias we can see that a current is flowing. The region of interest is slightly in the negative bias direction where the IV curve is relatively flat is where we are applying a electric field that allows for controlled tunning of the electrons and holes within the QDM.

This application of field with the diode structure is crucial to charging and generating specific charge states within the QDM. The bias regions where specific charge configurations are dominant are called their charge stability regions. These regions are due to the QDM engineered in a way that hole tunneling is preferential, this happens when the top QD has a higher confinement than the bottom dot. This naturally

occurs in our situation; note that the QDs are grown to the same height. In our case this occurs due to the larger lateral growth of the initial QD relative to the top dot. Thus the top dot has greater confinement. This allows for the hole energy of the bottom and top QD be tuned into resonance when in reverse bias.

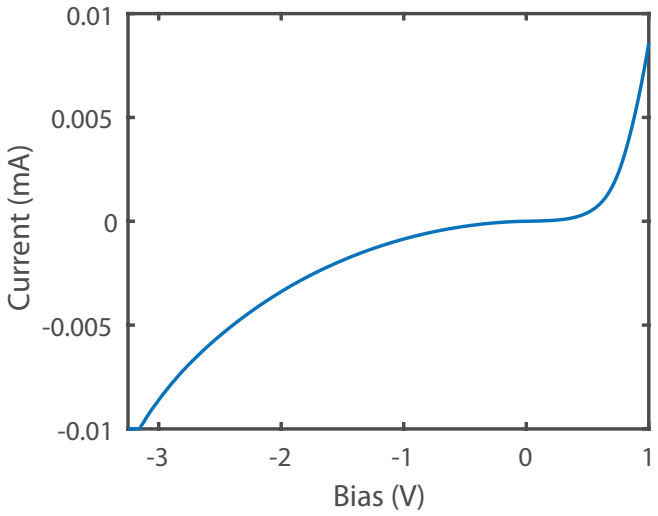

Figure 2.9: Current vs. bias of the sample's Schottky diode.

2.5 Charging of QDMs

Charging of the QDMs is an important tool for much of the optical studies pertaining to QDMs and leads to very interesting physics. Three major methods exist for having charges enter a QD or QDM. These three methods are via optical excitation, via electrical leads or delta-doping.

The first most common way that charge is induced is via optical means. The optical excitation of a photon when it is absorbed generates an exciton which is an electron-hole pair; an electron gets excited from the valence band of the QDM into the conduction band leaving behind a hole. Purely optical excitations generally does not change the net charge of the QDM, more on this in chapter 6.

A second way to charge the QDM is by delta-doping. Delta-doping is part of the growth technique that is used to get thin layers of high dopant concentrations within

a structure. This allows for charges to easily enter the QDs or QDMs. [55]

The last method of charging QDMs was mentioned in the previous section. By embedding the QDs inside electric field effect devices, such as p-i-n diodes or Schottky diodes, control over the band alignment is gained, allowing to adjust the predominant charge state of the QD. [56] Allowing for charges to tunnel in via the electrical leads. The charging structure is clearly seen in a bias map of a QDM. By applying a field to the structure this tilts both the conduction and valence bands of the QDM. Based on the relative location of energy levels of the bottom and top dot with that of the Fermi level of the structure dictates regions where we are more likely to get charges to tunnel into or out of the QDM. These charge stability region for the specific different charge states can be seen in Figure 3.6 in the photoluminescence spectra of a QDM molecule. At the low bias values the energy level of the dots are near level with the Fermi level of the doping of the GaAs substrate. As the QDM is exposed to larger fields in reverse bias the energy levels for the electrons is far out of tune with the Fermi level and holes are more likely to tunnel in. All three methods may be combined to achieve a certain variety of charge states but not by purely optical means. [53]

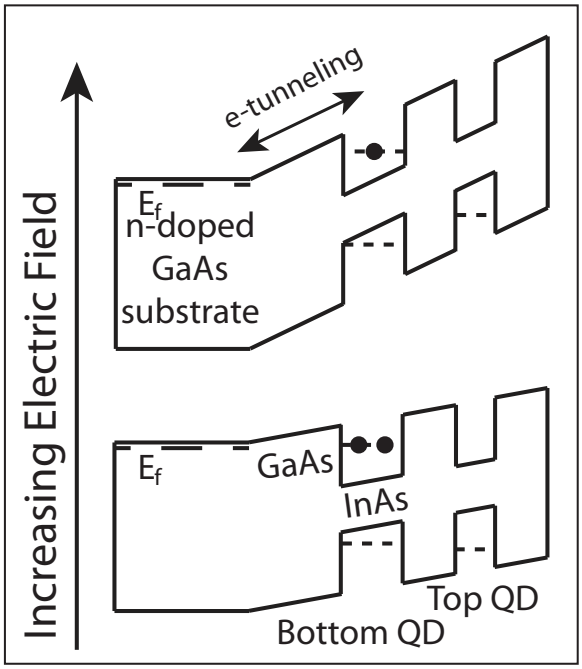

Figure 2.10: Schematic representation of the band gap diagram of a QDM under varying electric fields. At low field the conduction band electron level is aligned with the Fermi level allowing for electrons to easily tunnel into the QDM. At larger fields the electron energy levels are further tuned away from the Fermi level making it less likely for an excess charge to overcome the energy barrier and tunnel into the QDM.

2.6 Coulomb Interactions in a QDM

Due to the nature of charges being within close proximity; Coulomb forces become a major factor to the energy levels of the different charge states. These Coulomb interactions can be seen experimentally via the large energy shifts between the different charge states. In semiconductor nanostructures such as QDs or QDMs, the electrons and holes are in close vicinity which leads to large Coulomb potentials that shift the excitonic emission energy of the different charge configurations. [57] [58] In a typical QDM that is studied we see that the negative trion is about 6 meV below the neutral exciton. And the neutral exciton is within 1 meV of the positive trion. For the QDMs studied in this dissertation these differences between the charge states is due to the added Coulomb interaction of the charges. Overlap between the different

charge states is for the most part non-existent for the ground states.

2.7 Stark Shift

QDMs allow for transitions not only within one dot but between both the top and bottom QD. An intradot transition takes place in the bottom dot has a much smaller energy shift with respect to applied electric field than an interdot transition between the two dots. Both types of transitions are displayed in the QDM spectra; with the interdot transitions having much larger energy shifts with change of electric field. This allows for the transitions to be easily differentiated experimentally by the slopes of the lines. This effect can be explained by the large dipole moment of an interdot transition. The dipole moment is defined as $p = \pm ed$, where e is the charge of the electron and d is the distance between the electron and hole. With the larger separation a larger dipole is created leading to greater energy shift with larger electric fields.

The following relation allows using the slopes of the interdot transition as a method of getting the electric field value.

$$\triangle E = \pm \triangle F \cdot p$$

The electric field ($\triangle F$) is related to the length of the diode structure (L) and the amount of bias applied ($\triangle U$). Where

$$\triangle F = \frac{\triangle U}{L}$$

This leads to

$$\pm p = e \cdot d = \frac{\triangle E \cdot L}{\triangle U}$$

This tuning of the transition energy provides a useful tool for studying many

interesting physics of the QDM systems. The PL spectra of a QDM in a vertical electric field shows the intradot and interdot behavior as a function of applied electric field. The intradot transitions are only slightly effected by the applied electric field due to the small dipole moment. Whereas the interdot transitions are greatly effected by the electric field with their dipole moment of the electron and hole being much larger due to the separation being across both QDs. Of particular interest is what happens when these transitions comes into resonance. This leads to tunnel coupling of the QDMs.

2.7.1 Molecular States

Optical spectroscopy has portrayed many interesting properties of the QDMs and they can be described analogously to atomic molecules. For large inter-dot separation the exciton states of individual QDs will not interact and will remain localized. But, decreasing the inter-dot separation, at the nano-scale the exciton can become delocalized with the electron or hole wave functions spread across both QDs via quantum mechanical tunneling. This process is analogous to covalent bonding between identical atoms. While on the other hand, if the wave function of the charge carrier is localized predominantly in an individual dot the coupling more closely resembles an ionic bond. By introducing a perturbation, such as an electric field, the inter-dot coupling can be controlled and transformed between ionic and covalent bonds. [59]

This coupling of QDs was first reported in 2001. [60] Since then the discovery of using an external tuning parameter such as applying an external electric field to the QDM clearly displays the coupling.

Tunnel coupling can be understood by analyzing a two state system. We can consider a single exciton in a QDM, where for simplicity the hole alone is able to tunnel between the two dots. If we consider vertically stacked QDMs, then we can consider two localized basis states as shown in figure 2.11

Figure 2.11: Base states for direct and indirect exciton

When the QDM is excited, an electron (black circle) populates the conduction band. The remaining hole in the valence band (white circle) can be either in the bottom dot (Intradot exciton) or top dot (Interdot exciton). The Hamiltonian for this system is given by the following matrix in the localized basis.

$$H = \begin{bmatrix} E_1 & t_h \\ t_h & E_2 - edF \end{bmatrix}$$

Here E_1 and E_2 are the energies that correspond to the intradot and interdot excitons, respectively, in the absence of an external electric field, F. For the indirect exciton, due to its large electric dipole moment $p = ed$ where e is the elementary charge, d the interdot separation, and application of an external electric field, F, produces a large Stark shift edF. The influence of the tunneling between the separate dots, where th is the tunneling amplitude, generates new eigenstates and eigenenergies of the system, given below:

$$E_{\pm} = \frac{E_1 + (E_2 - edF) \pm \sqrt{(E_1 - (E_2 - edF))^2 + (2t_h)^2}}{2}$$

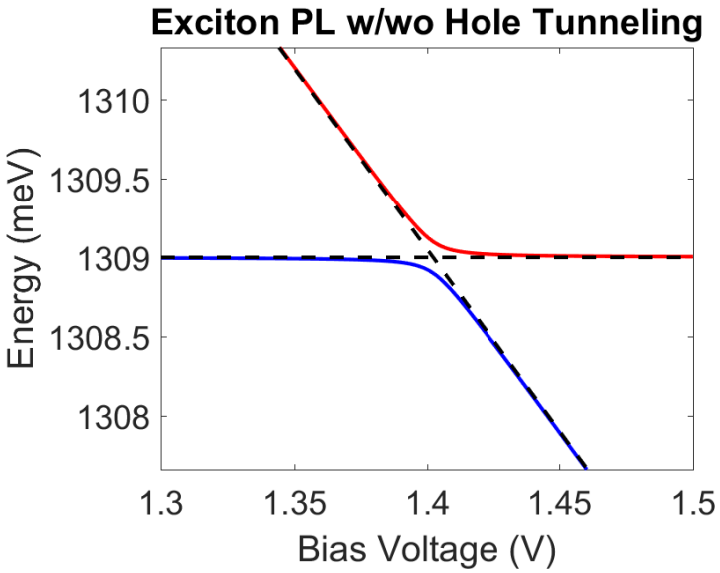

Figure 2.12: Base states for direct and indirect exciton

This solution is plotted in figure 2.12, alongside the solution for without hole tunneling (dashed lines). The location of the energy crossings show where the two states are at resonance. In the presence of tunnel coupling, there is an avoided crossing and the energies of the two states are split by $2t_h$ at resonance. The resulting states are symmetric and anti-symmetric states superpositions of the localized base states, forming bonding and anti-bonding states analogous to real molecules as mentioned above. The above theoretical description is clearly evidenced in photoluminescence (PL) scans of a QDM sample, where the QDM is excited via laser and the emission spectra are plotted vs. electric field. It is seen that two PL lines form an anti-crossing in exceptional agreement with the theory, see figure 2.13.

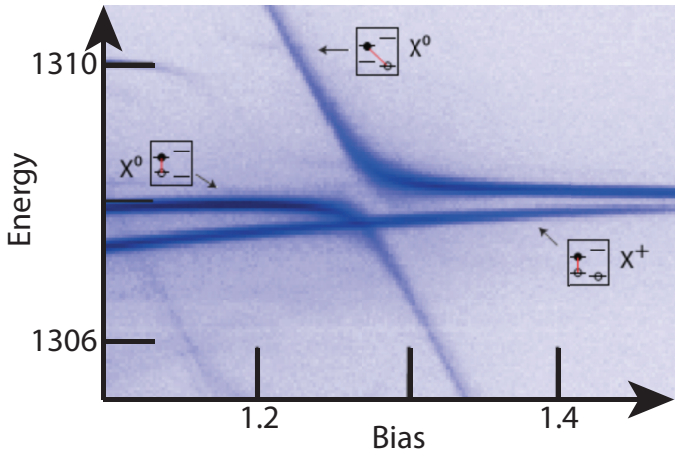

Figure 2.13: Base states for direct and indirect exciton

2.7.2 Level Anticrossing Spectroscopy

The tunnel coupling has increasingly become a huge tool for the mapping of a QDM. Level anticrossing spectroscopy (LACS) uses PL spectroscopy to map the excited states of a QDM. It allows to monitor the indirect excited states at the higher excitation energies and map them into the anticrossings of the ground state. Each QD even in a single molecule has largely differing electronic structures making it crucial to map these differences. LACS uses the ladder of orbital energy levels of a single quantum dot to probe that of another nearby QD. [61] This method allows for a spectroscopic mapping of a nearby QD's energy level structure. The LACS method uses the neutral exciton of the bottom QD (direct exciton) as the probe for mapping the excited states of the top QD's energy levels (indirect). LACS can be described by using the recombination of the electron and hole in the bottom QD neutral exciton as a probe when the electric field is tuned and the hole tunnels through to the top QD when the energies are in resonance. This is portrayed in the spectra as a series of anti-crossings in the ground state of the bottom dot, allowing for a mapping of the top dots excited energy levels.

2.8 Varshni Law

Temperature greatly affects the band gap of semiconductors. The Varshni law describes the band gaps size as a function of temperature. [62] This was empirically shown by Varshni. The energy band gap of semiconductors tends to decrease as the temperature is increased. This can be understood by looking at the interatomic spacing and how it increases due to the larger amplitude of atomic vibrations from the increased thermal energy. With the increased interatomic spacing a decrease of the potential is seen by electrons in the material and this in turn reduces the size of the energy band gap. The following equation describes the band gap energy as a function of temperature.

$$E_g(T) = E_g(0) - \frac{\alpha T^2}{T + \beta} \tag{2.12}$$

$E_g(0)$ is the band gap at 0 K, α, and β are the fitting parameters characteristic of a given material. [63] The following figure 2.14 is a plot of Varshni's relation for GaAs.

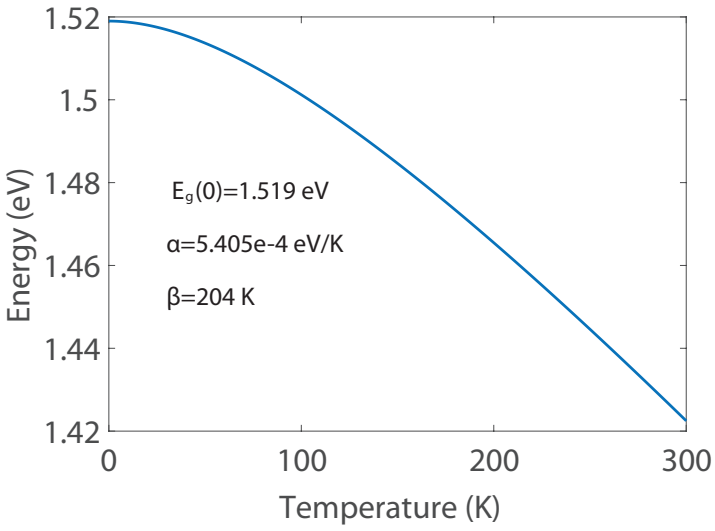

Figure 2.14: Band gap energy as a function of temperature for GaAs.

2.9 Lattice Vibrations

Another part of the system that we need to consider is crystal vibrations. Previously discussed electronic states of the QDM were shown considering the crystal lattice is stationary. We know that in reality the atoms of the crystal lattice are vibrating and in constant motion.

2.9.1 Classical Approach

We can better understand the lattice vibrations by considering a one-dimensional lattice where in the case of InAs or GaAs we have two different atoms with different mass such as In and As in a single unit cell. Figure 2.15 shows the 1D diatomic lattice where each of the two different atoms have a different mass m_1 and m_2 separated by a distance a. By taking the harmonic approximation for the atoms interconnected by elastic springs with their interatomic spring constant k.

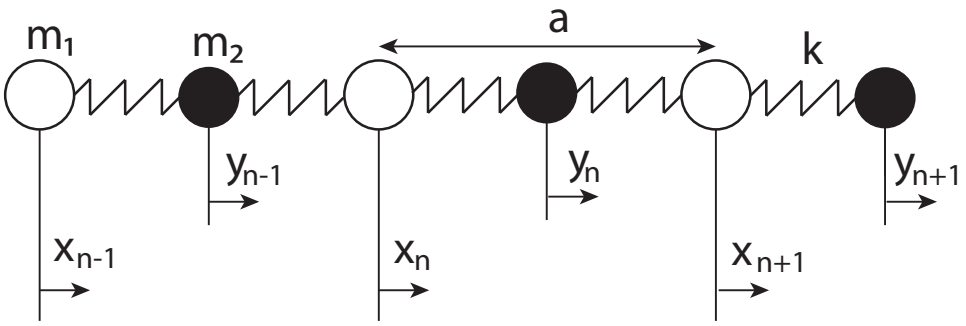

Figure 2.15: 1D Schematic of a diatomic lattice

From the equations of motion one can solves for the dispersion being:

$$\omega^2 = k(\frac{1}{m_1} + \frac{1}{m_2}) \pm k[\frac{1}{m_1^2} + \frac{1}{m_2^2} + \frac{2}{m_1 m_2} cosqa]^{1/2}$$

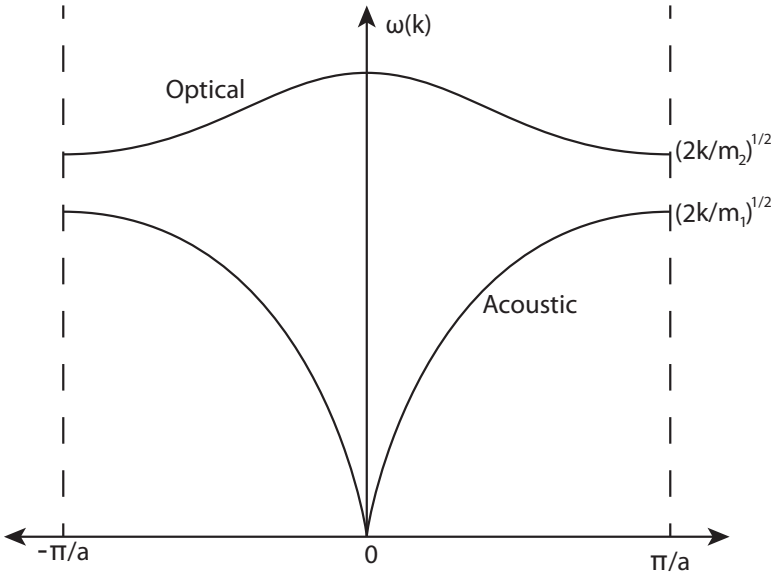

Figure 2.16: Dispersion curves of the optical and acoustic phonon branches for a diatomic chain

This leads to two solutions. The first solution for the negative sign describes the dispersion of the acoustic phonons. In acoustic modes the two different atoms are in phase with each other. The positive solution on the other hand describes the optical phonons, these lattice vibrations occur when the two different atoms are out of phase. These two solutions of the dispersion are plotted for both acoustic and optical phonons in figure 2.17.

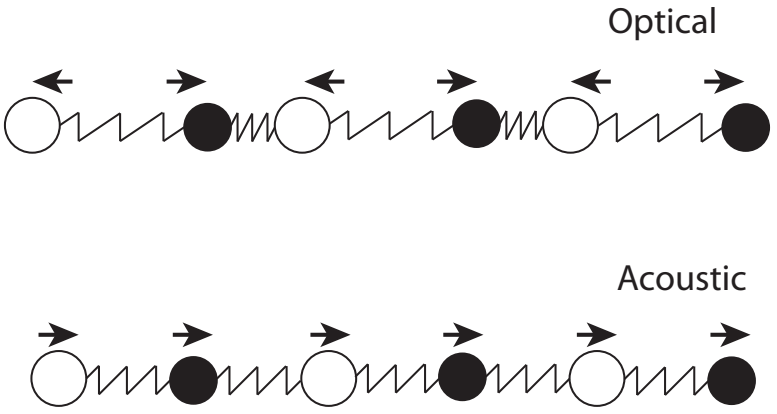

Figure 2.17: Schematic of acoustic and optical lattice vibrations

This approach can be scaled to a three dimensional lattice. The mathematical details are omitted here, but can be found in standard solid state textbooks. [18] [19] The solutions can be represented in terms of

$$\mathbf{u} = \mathbf{A}e^{i(\mathbf{q}r-\omega t)}$$

where the wave vector $\mathbf{q}$ specifies the wavelength and the propagation. The vector $\mathbf{A}$ determines the amplitude as well as the direction of the vibration of the atoms. Both the wave vector and the vector $\mathbf{A}$ dictates the polarization of the wave, whether it is longitudinal where $\mathbf{A}$ is parallel to $\mathbf{q}$ or transverse when $\mathbf{A}$ is perpendicular to $\mathbf{q}$.

Substituting the solution and solving for $\mathbf{A}$, we get three components for each dimension, A_x, A_y, and A_z. giving three different dispersion relations. Since both InAs and GaAs are diatomic lattices with two different atoms this leads to a factor of two more dispersion curves for each atom leading to six total dispersion curves. Our final modes in the acoustic branch consist of two transverse acoustic (TA) and one longitudinal acoustic (LA) and the remaining branches being in the optical either longitudinal optical(LO) and transverse optical(TO).

2.9.2 Phonons

From quantum mechanics it is known that the energy levels of a harmonic oscillator are quantized. Similarly energy levels of the lattice vibrations are also quantized. We call these quantized vibrations of a crystal lattice phonons. They can be thought of as analogous with the photon which is a quantum of an electromagnetic wave.

We know that for the harmonic oscillator the allowed energy levels are:

$$E = (n + \frac{1}{2})\hbar\omega$$

where $n = 1, 2, 3...$ is the quantum number. And ω is the frequency of the normal vibration mode in the crystal defined in:

$$u = Ae^{i(qr-\omega t)}$$

where A is the amplitude, u is the displacement of the atom from the equilibrium position x. Averaged over time the energy of this vibrational mode is:

$$E = \frac{1}{2}M\omega^2 A^2 = (n + \frac{1}{2})\hbar\omega$$

From this relationship we can see that classically any amplitude of vibration is allowed whereas in quantum mechanics only discrete values are allowed.

Phonons are often a nuisance in quantum systems due to their interactions with the quantum states leading to decoherence. But these phonons can also be coupled to electronic states forming hybridized quasiparticle called polarons that will be mentioned in chapter 5.

Chapter 3

Experimental Methods

Optical spectroscopy has been used throughout all branches of science, from cataloging individual elements spectra, to studying novel materials, to analyzing the composition of stars. [64] [65] [66] Spectroscopy greatly advances our understanding of the world around us. A few different optical measurement techniques were used throughout the experimental work covered in this dissertation and they will be described in this chapter.

Most of the equipment used in the experiments were controlled using customized software written in LabView. Appendix B describes the software that was used to control and automate the equipment.

Fig 3.1 shows a schematic of the general spectroscopy setup used for this work. Our samples are mounted in a microscopy cryostat, and the setup has two optical branches. The first being the excitation side which begins with a light source, in this case a laser. The laser light travels through a number of optical components. Some of the optical components commonly used are a wave meter, power meter, neutral density filter, short pass filter, polarizer, liquid crystal retarder, quarter wave plate and a focus lens. On the detection side, the light is collected with a high numerical aperture microscope objective. The light then passes through a liquid crystal retarder and polarizer and finally through a long-pass filter before being focused into the spectrometer; where it is spectrally dispersed by the diffraction grating and it is collected by a liquid nitrogen cooled CCD. The spectra that is collected, is then

displayed on the computer and stored for further analysis.

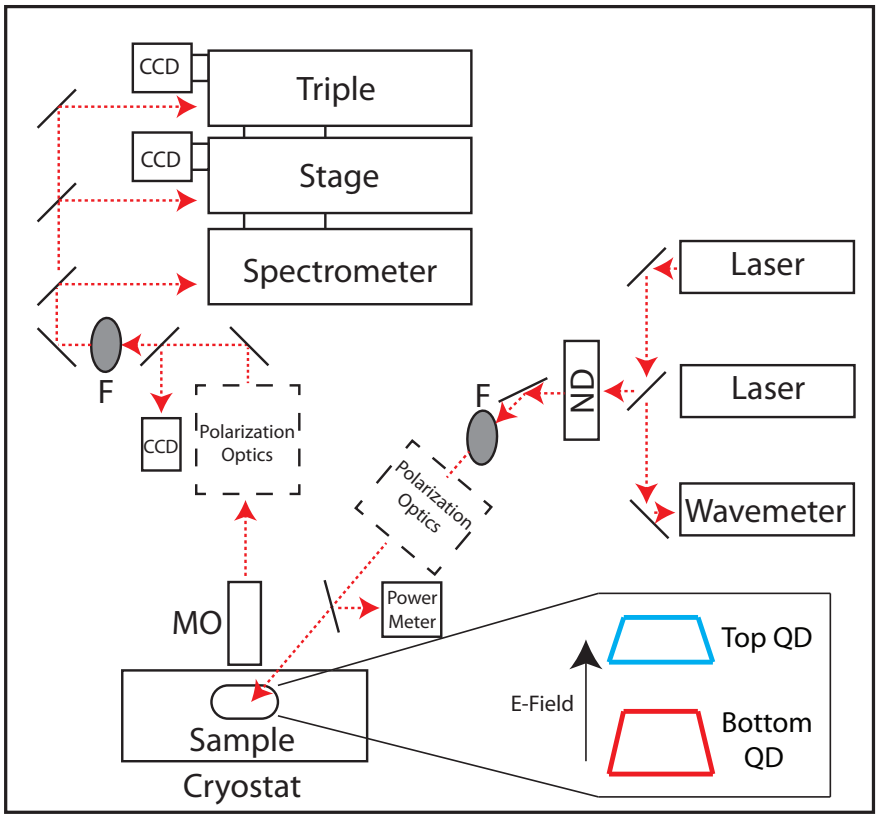

Figure 3.1: Spectroscopy setup that is used for a majority of research covered in this dissertation. The sample is excited with a laser, which goes through various optical components such as neutral density (ND) filter, optical filter (F) to the sample. The emitted light from the sample is collected by a microscope objective (MO) and is also sent through more components to the spectrometer where the light is dispersed and collected by a CCD.

3.1 Equipment

3.1.1 Cryostat and Sample

The cryostat used is a closed cycle helium cooled cryostat that is outfitted with a microscopy option. The microscopy option allows optical access to the sample. The

cryostat is necessary for getting higher emission intensities and well resolved spectra from the QDMs. At low temperatures the signal to noise ratio for the QD emission is much higher due to the lack of thermal noise. [67] The QDM samples are mounted in a chip header as mentioned in chapter 2. The chip header is then pressure mounted to a sample holder that is on the cold finger. Indium foil is used as an interface to achieve good thermal contact between the different interfaces due to Indium being highly ductile. These few steps are portrayed in figure 3.2.

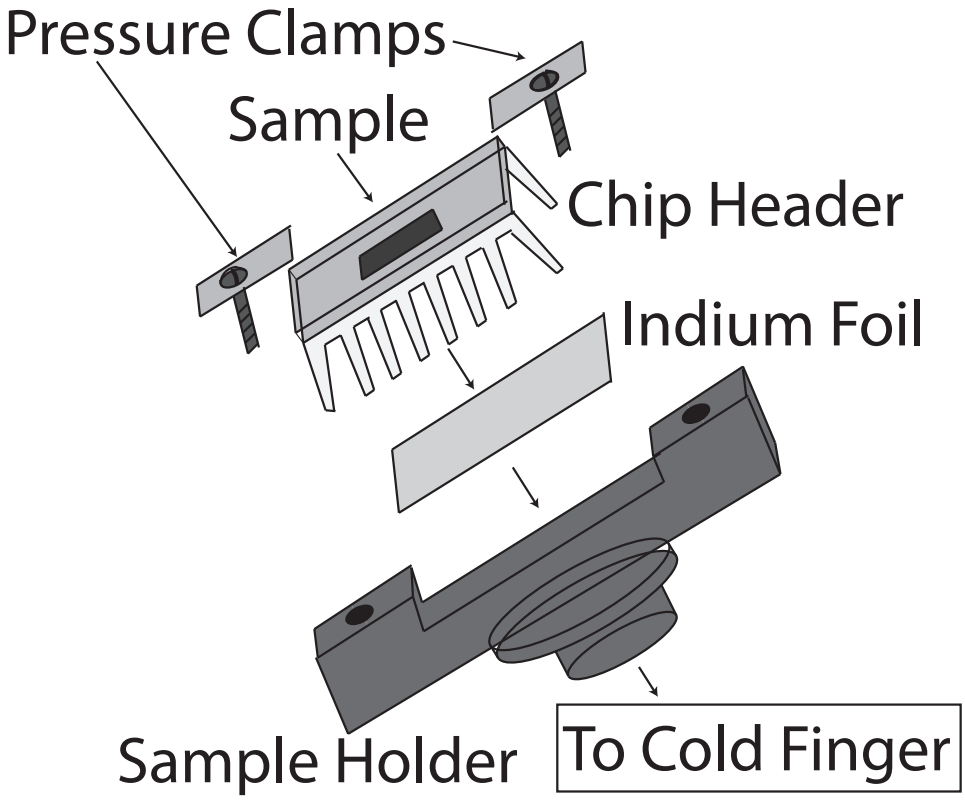

Figure 3.2: Schematic of sample mounting; using Indium foil as a interface to achieve good thermal contact.

The cryostat is capable of reaching a low temperature of 18 K and has a temperature stability of 0.1 K that is governed by a PID control. The cryostat has wire feeds that allow to connect electrical leads from the sample to a source meter. The wiring is then connected to the pins of the chip header that the sample is mounted to, allowing for electric bias to be applied across the samples growth direction. As

mentioned in chapter 2 this bias corresponds to an electric field the QDMs experience. The Keithley source meter used is able to apply 20 V with a minimum step size of 0.1 mV. For positioning the sample, the cryostat is mounted to a xyz-translation mount. The mount makes fine positioning of the samples location possible and allows to control the focus of with respect to the microscope objective.

3.1.2 Excitation Path

The excitation path comprises of the following components: Laser, neutral density filters, optical filters, polarizer, liquid crystal retarder, quarter wave plate, wave meter, power meter and pellicle beam splitters. Starting at the light source, optical excitation was achieved using two different light sources. Depending on the application either a continuous wave (CW) Ti: Sapphire laser or a tunable diode laser was used. The Titan Ti:Sapphire laser has three different mirror sets; short-band, mid-band, and long-band depending on wavelength range needed to excite the sample. The corresponding wavelengths for the three mirror sets are 700-820nm, 780-900nm, and 890-1020nm respectively. Along with the tunability of the Ti-Sapphire laser's energy, it also offers excitation powers of up to 500 mW. The other excitation option that is extensively used is a Toptica tunable-diode laser, this laser is tunable between 890 nm and 990 nm and has a line width of $<$300 kHz and offers powers of up to 150 mW. The beam path splits at a 92/8 beam splitter, which directs 8% of the laser to a wave meter. The wave meter offers an accurate excitation energy reading up to $\pm$ 0.0001 nm this offers feedback that is used in the computer software's PID control that sets and scans the excitation energy. The remainder of the laser passes through a filter wheel with varying neutral density filters, this allows to control the excitation's laser power for studying power dependence of the samples. Next, the laser passes through a short-pass filter, this optical component greatly helps eliminate any sideband laser light that might be detectable at the higher detection wavelengths. This filter is a nice addition to non-resonant photoluminescence sand also the phonon assisted quasi-resonance fluorescence spectroscopy mentioned in chapter 4.

If polarization studies are being completed, polarization components such as linear

polarizers, liquid crystal retarder, and quarter wave plate can be added at this stage. The combination of these components allows to put the light in any polarization state desired and make up the polarization control components of the setup. These components allow for total polarization control of the excitation laser light. Prior to the laser exciting the sample a small portion of light is split off and sent to a power meter. Knowing the power of the laser right before excitation is important for quantifying the power densities that the sample is excited with. Finally the remainder of the light is sent to excite the sample.

3.1.3 Oblique Incidence Excitation

Depending on the experiment there are two optical paths for directing the laser onto the sample in the cryostat. The first is to have a focus lens that sends the laser toward the sample obliquely, this path comes in at about a 45° angle passing by the microscope objective. An advantage of exciting the sample obliquely is that a majority of the reflected laser light does not enter the detection path. This gives the oblique geometry an advantage when it comes to minimal stray laser light making its way to the spectrometer. Though the method has the limitation of offering lower power densities since the spot size is diffraction-limited by the lens.

3.1.4 Normal Incidence Excitation

The other excitation path that is easily incorporated into the setup sends the laser through the microscope objective. Additional optical components of a mirror and pellicle beam splitter are needed. The beam splitter is placed in the detection path, in combination with the mirror this allows to walk the laser beam and align the laser through the microscope objective. Excitation through the microscope objective is capable of attaining much larger power densities due to the smaller focal point of a microscope objective. The major challenge with this method is that a large amount of laser light gets reflected back down the detection path. Often other optical techniques are needed to eliminate the stray laser light when use this excitation scheme. Some techniques to eliminate the reflected laser are to use high extinction cross polarizers

and spatial filters.

3.1.5 Detection Path

On the detection side, for collection of the QDM's emission we use a high numerical aperture 50x magnification microscope objective. This light can then be analyzed with respect to polarization; by sending it through a polarizer, liquid crystal retarder, and quarter wave plate. Similarly to the excitation side the polarization components are optional and only needed when polarization information is necessary. The light is then sent through a long-pass optical filter which complements the short-pass filter on the excitation side and provides additional means to eliminate the elastically scattered laser light from making it to the spectrometer. The light then goes through a focusing lens into the spectrometer, the spectrometer used is a Princeton Instruments triple spectrometer. The spectrometer can be run in three operational modes.

3.1.6 Single Stage Mode

The first operational mode is when the light is only dispersed by the third stage, this is equivalent to just a single spectrometer. Each stage has the choice of spectrally dispersing the light using one of three diffraction grating mounted on a turret. The following diffraction gratings can be chosen for the first stage: 750, 1,100 and 1,800 cm^{-1} line gratings. For the other two stages the diffraction gratings that can be selected are: 750, 900, and 1,800 cm^{-1} line gratings. It is also important to note that the resolution of the spectral features is limited by the dispersing power of the spectrometer along with the sensitivity of the CCD. The maximum spectral resolution for a single stage is 26 μeV. The other operational mode is subtractive mode.

3.1.7 Triple Subtractive Mode

Subtractive mode effectively makes the first two stages of the spectrometer a high-quality band pass filter to assist in the suppression of scattered laser light. This feature is very favorable when near resonant experiments are being run or when the

sample is being excited through the microscope as mentioned in the normal incidence section, since it greatly helps eliminate the scattered laser light.

3.1.8 Triple Additive Mode

The third operational mode of a triple spectrometer is running it in triple additive mode. This mode allows us to use all three stages to disperse the light attaining much higher spectral resolutions. The maximum spectral resolution in triple additive for our spectrometer is around 10 μeV.

The emission is then finally captured by a liquid nitrogen cooled charge coupled device(CCD). The CCD's chip is 1340 X 100 pixel large. The CCD's data is then collected by the computer software. The raw data from the CCD is displayed as intensities per each individual pixel. An advantage of using a CCD chip is that one can vertically bin regions of the chips pixels greatly increasing the sensitivities and getting much higher intensities. The other dimension of the CCD chip is calibrated to the spectrometer's dispersion thus relating the individual pixels to detection energies or wavelengths being collected.

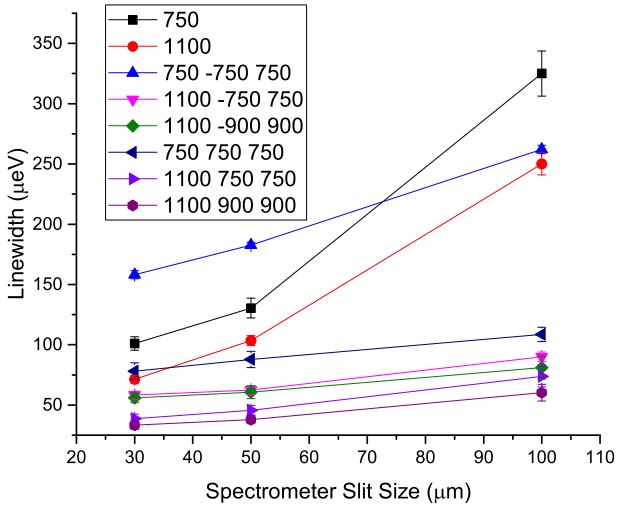

Figure 3.3: Linewidth as a function of spectrometer slit width. The instrument response function for the spectrometer's various diffraction gratings and operational modes is plotted.

3.2 Photoluminescence Spectroscopy

Photoluminescence (PL) is one of the most commonly used spectroscopic techniques for the study of nanostructures, including QDMs. It is a greatly utilized technique for studying and characterizing QDMs. Photoluminescence is non-invasive and non-destructive technique. Non-resonant photoluminescence emission occurs when an incoming non-resonant photon of higher energy excites an electron from the valence band into a continuum of states such as the wetting layer or other excited state of the QDM. The excited state is very short lived, as the electron or hole relaxes back to the ground state via phonon interactions. Then recombination occurs with the emission of a photon and the process is continued. These re-emitted photons are collected to make up the spectra. This process is shown in figure 3.4. Non-resonant PL has the added benefits of an energy separation between the excitation and detection. This allows the added use of optical long-pass and short-pass filters to help eliminate the residual laser sideband photons. This provides large relative emission intensities when

compared to the zero level background.

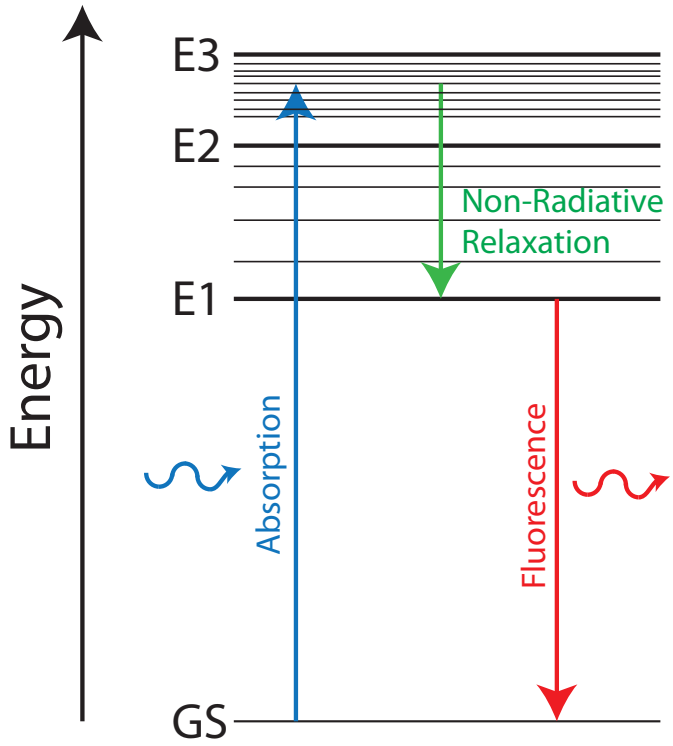

Figure 3.4: Optical process for photoluminescence; with absorption, non-radiative relaxation, and fluorescence being presented.

The photoluminescence provides a plethora of information about the QDM; from the energy level structure, excited state lifetimes, fine structure and relative intensities. Figure 3.4 shows an example of a PL spectra of a QDM. In this figure one can see the most notable features of delta like emission of the discrete energy levels of QDs and QDMs; giving them the designation 'artificial atoms'.

In figure 3.5 the spectra has other charge states that are visible. From a single spectrum it can be very difficult to be able to discern the many different charge states. As mentioned in chapter 2 the QDM samples are embedded in a Schottky diodes that allows to apply an electric field to the QDM. This electric field in turn greatly shifts the band gaps and shows some very interesting physics that was presented in chapter 1. By changing the applied bias/electric field and recording a spectrum at each bias step and assembling all spectra in an intensity matrix, allows for a very insightful way

of displaying the opto-electronic properties of QDMs. By taking an individual PL spectrum at different biases can greatly simplify and assist the process of identifying the many different charge states of a QDM. For the extent of this thesis the bias ranges varied between -2.5V to -0.5V as mentioned in chapter 2. After the computer software collects the spectrum at each bias, the software stitches the spectra together creating a bias map. A lot of the charging map of the QDM begins to be resolved when the full picture is put together. As mentioned in chapter 1 the different charge states have favorable charging plateaus due to the relative distance that the bottom QD's conduction bands energy level is with the Fermi level in the doped substrate. The typical laddering of the charge states in a PL spectra has more negatively charged states being stable near forward bias due to the electron levels being near level with the Fermi level. As the bias is adjusted toward reverse bias it is more likely for the electrons to tunnel out of the QDs; thus leaving positive charge states to be formed.

Bias maps are a very insightful way to study the physics of the QDMs. It is also very handy in identifying and monitoring the various indirect transitions that are mentioned in chapter 1. The indirect transitions are particularly distinguishable due to their large slopes. With the indirect line, charge stability plateaus and some Coulomb potential calculations we can identify the charge states of each transition. Figure 3.6 shows a bias map of a QDM, the complexity of the different charge states is easy to see and also the laddering and progression from negative to positive charge states as the bias is set higher in reverse bias.

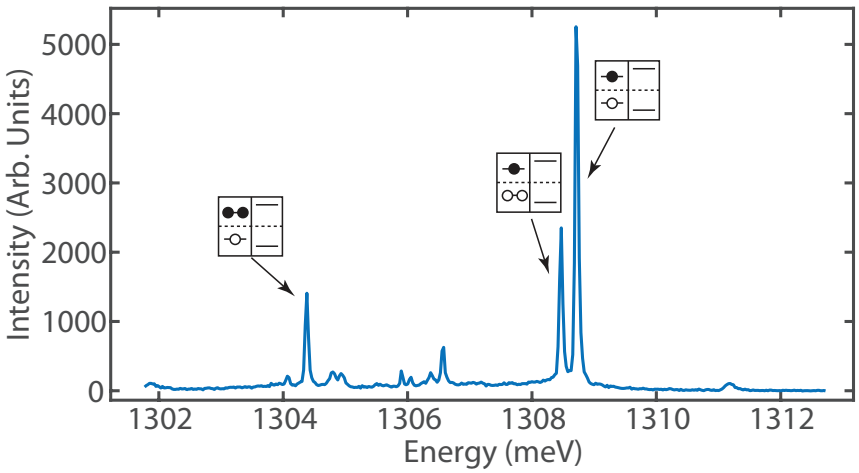

Figure 3.5: PL spectrum of a single QDM. The spectrum was obtained with an excitation wavelength of 918 nm and and intensity of 0.8 mW.

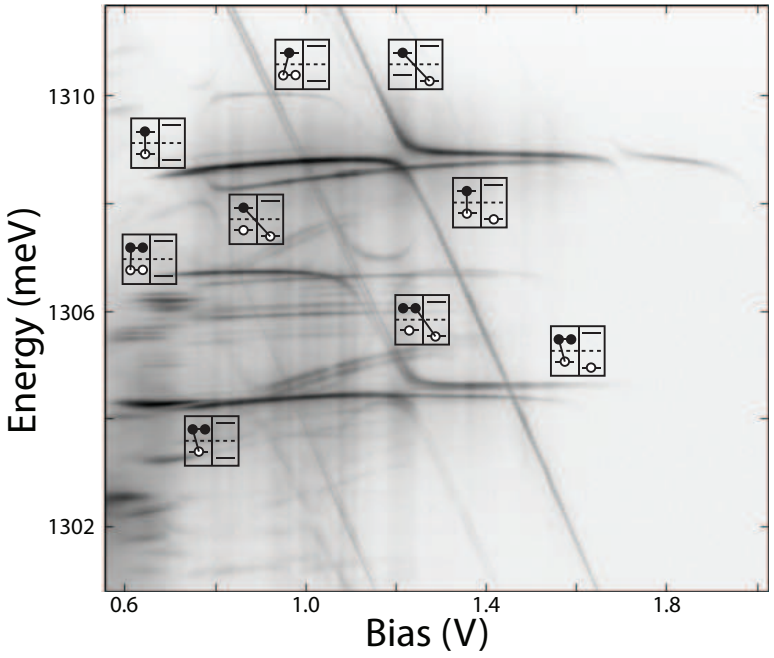

Figure 3.6: Electric field dispersed spectra for a QDM. A plethora of different charge states are visible. The data was taken with an excitation energy of 918 nm and power at 20 mW.

3.3 Photoluminescence Excitation Spectroscopy

Photoluminescence excitation spectroscopy (PLE) is another optical spectroscopy technique we often used. This experimental technique is an extension of PL and another way to map the energy level structure of a QDM. [61] PLE spectra represents the absorption spectrum of a material or QDM, it also has the added benefit of attaining better resolution than PL. To generate a PLE measurement the laser energy is scanned across an energy range of interest. At each different excitation energy a bias map is generated. The method's increase of resolution is due to it being similar to a resonant measurement, it is when the laser is resonant with an excited state when a strong signal is emitted from the ground state, hence achieving laser-limited line-width resolution. Figure 3.7 demonstrates schematically the optical process of PLE spectroscopy, where a laser is scanned across excited energy levels of a QDM and a non-radiative relaxation process occurs into the metastable ground state. Radiative relaxation then occurs and is collected as PL.

The process is described by a laser coming into resonance with an excited state a very quick non-radiative relaxation process populates the ground state of the specific charge state. At this point the emitted photons from the ground state are collected. Upon generating a complete bias map we can monitor the specific charge states of the QDM. This method will be greatly used in chapter 5 and 6 when phonon induced transparencies and optical charging will be discussed. By monitoring a specific charge transition's emission at all the different excitation energies a PLE map can be generated. Figure 3.8 shows a QDM's PLE map. The PLE map shown is for the neutral exciton charge state, where a single electron was excited into the conduction band. The bright lines in the PLE figure 3.8 show the absorption of the laser light into these excited states. In the PLE map both direct and indirect excited neutral exciton states are clearly visible. Even the associated phonon band's which will be a major focus of chapter 4 and 5 are clearly seen.

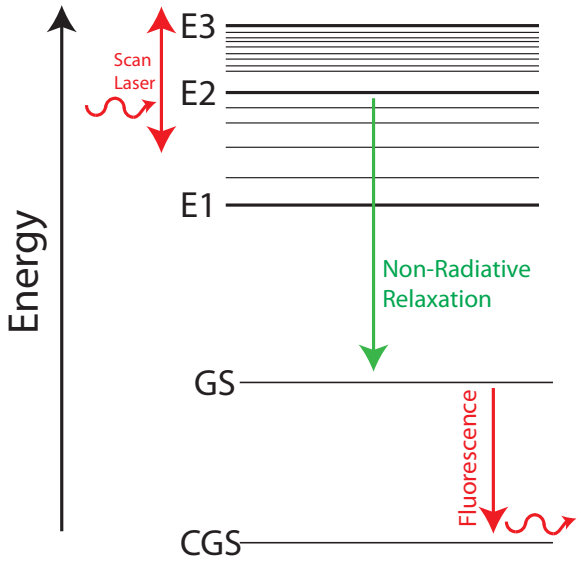

Figure 3.7: Schematic of PLE process. Laser is scanned across excited states, when resonant with an excited state non-radiative relaxation into the ground state occurs where the PL is collected from exciton recombination.

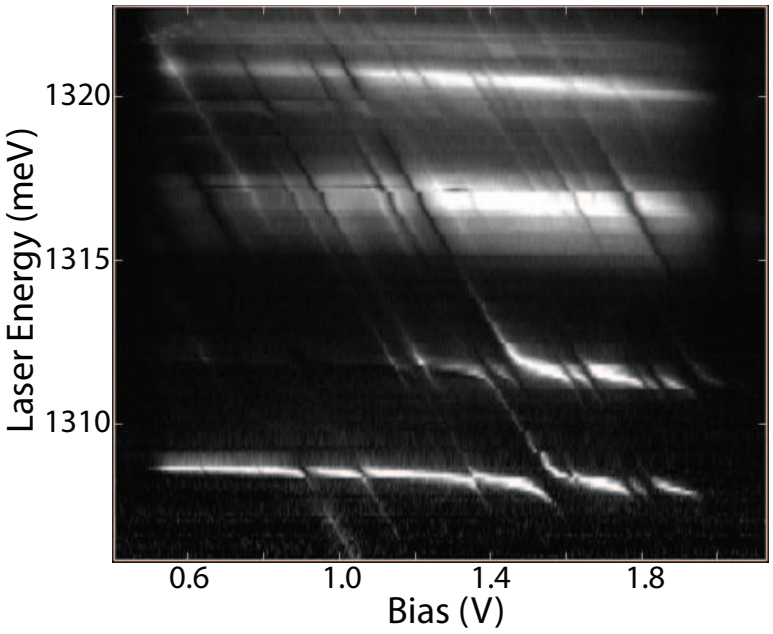

Figure 3.8: Experimental PLE map for a QDM. The excited states of the neutral exciton are visible along with the continuum of the optical polaron band. Both direct and indirect excited states are visible.

Chapter 4

Phonon-Assisted Quasi-Resonant Fluorescence Spectroscopy

4.1 Introduction

Improvement in spectral resolutions is always viewed in a positive light. This chapter will present an optical technique similar to those mentioned in the previous chapter but with a much higher spectral resolution capabilities. Introduced is a method for making high resolution spectral measurements by using the intrinsic properties of the semiconductor's associated optical phonon band. By resonantly exciting into a transition and monitoring 1 LO (Longitudinal Optical) phonon energy below the excitation the experiment is able to generate high resolution spectra. The technique adds advantages from both laser and PL spectroscopy. The method exploits the advantageous features of both optical techniques and provides a method to attain high resolution spectra with basic equipment available in most optics labs. This work was published in 2016 in the Journal of Visualized Experiments (JoVE). [17]

High resolution is the key to unlocking new knowledge. With this knowledge, new technologies can be developed such as better sensors, more precise manufacturing tools, and more efficient computational devices. Generating this key, however, often comes at a high cost of resources, time or both. This issue is omnipresent across all scales from the atomic physics of resolving the lifted degeneracies of electron spins,

to astronomy where a small spectral shift can lead to detection of planets next to distant stars. [68] [69] [70]

This chapter's focus is on using a standard spectrometer setup to resolve spectral features below the spectrometer's resolution limit. The example presented is that of anisotropic electron-hole (e-h) exchange splitting in InAs/GaAs quantum dots (QDs), which is on the order of a few μeV. [68] The resolution limit of the spectrometer can be overcome by combining standard PL and laser spectroscopy techniques. This method of quasi-resonance fluorescence has the added benefit of achieving laser limited resolution using a commonplace single-stage spectrometer.

4.2 Setup

The key advantage of this technique is that it can be easily incorporated into a standard optical spectroscopy system such as described in the previous chapter. PL spectroscopy of a single QD normally consists of a single-stage 0.3 m - 0.75 m monochromator and a CCD detector along with an excitation laser source and optics. Such a system is at best capable of resolving 50 μeV in the near-infrared spectrum around 950 nm. With the additional use of statistical and deconvolution techniques, a single monochromator setup is capable of resolving to around 20 μeV resolution in PL measurements. [71] This resolution can also be improved by using a triple spectrometer, in triple additive mode, where the spectrum is successively dispersed by all three gratings. The triple spectrometer has the advantage of increased resolution, capable of resolving around 10 μeV. In an alternative configuration, triple subtractive mode, the first two gratings behave as a band pass filter, giving the added feature of being able to separate the excitation and detection by less than 0.5 meV. The drawback of the triple spectrometer is that it is a costly system.

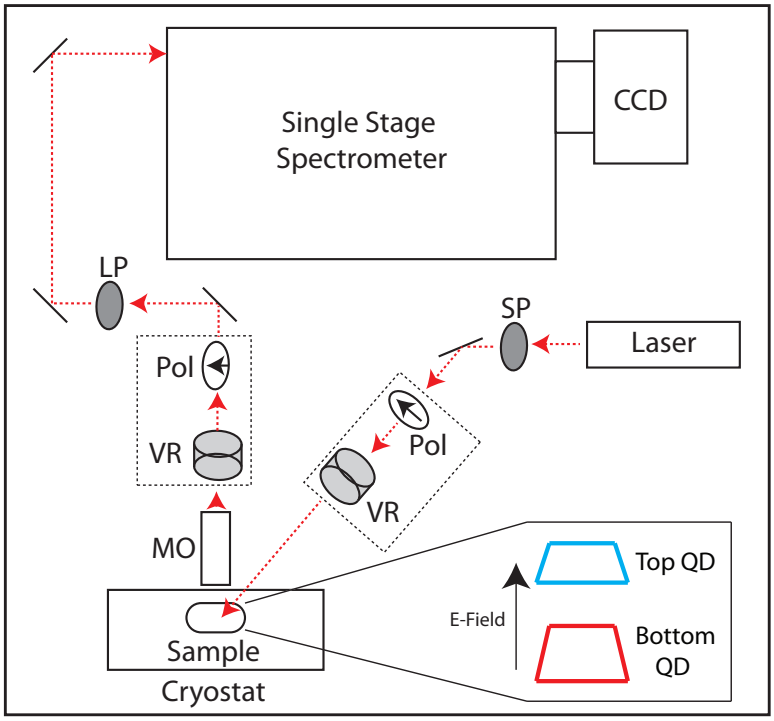

Figure 4.1: Experimental Set-up Schematic Schematic representation of the simple spectrometer set-up that is used for the LO phonon assisted measurements. Indicated are the tunable diode laser, both long-pass (LP) and short-pass (SP) filters used for tuning the region of detection, the microscope objective (MO), the spectrometer, and liquid nitrogen cooled CCD. The dashed boxes on both the excitation and detection represent the optional components of a variable retarder (LCR) and polarizers (Pol) necessary for polarization measurements.

4.3 Comparison to Other Methods

Before presenting the method of interest, we briefly discuss other experimental approaches that, with added complexity, achieve better spectral resolution and are able to resolve the fine structure of single QDs. Elements of these methods are relevant to the presented method.

4.3.1 Fabry-Perot Interferometer

One such method is adding a Fabry-Perot interferometer (FPI) in the detection path of a single spectrometer setup. [72] Using this method the resolution is set by the finesse of the FPI. Thus, the spectrometers resolution is improved to 1 μeV, at the cost of added complexity and lower signal intensity. [73] The interferometer method also changes the general operation of the spectrometer with the CCD camera, effectively becoming a single point detector, and the tuning through various energies is achieved by adjusting the FPI cavity itself.

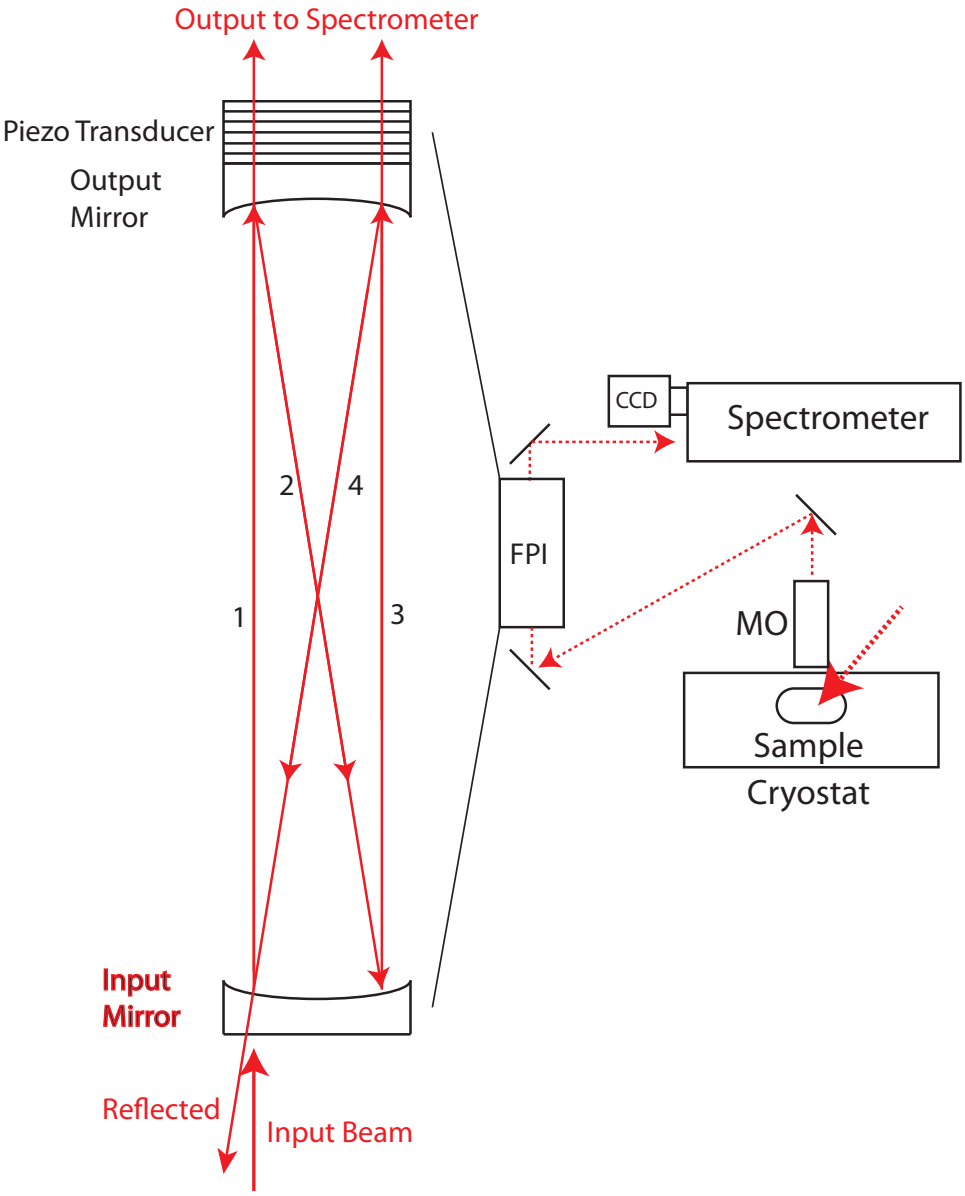

Figure 4.2: Experimental Set-up with additional Fabry-Perot Interferometer (FPI) in the detection path. Schematic of optical path in the FPI. Output mirror attached to piezo-transducer ring that allows to scan the Fabry-Perot. Input beam offset from optical axis is exaggerated for portrayal of optical path.

4.3.2 Resonance Fluorescence Spectroscopy

Resonance fluorescence (RF) spectroscopy, another method where a single optical transition is both excited and monitored also offers the promise of high-resolution spectroscopy. The spectral resolution is only limited by the laser line width and keeps the CCD as a multi-channel detector, where not just one sensor is detecting the signal but a number of CCD pixels. This multichannel detection is advantageous in terms of signal averaging. The challenge in RF spectroscopy is separating the PL signal from the larger background of the scattered laser light, especially when measuring at the single QD level. A number of techniques can be used to lower the ratio of signal to scattered laser light, which involve either polarization, [74] spatial, [75] or temporal separation [76] of the excitation and detection or combination thereof. The first is to use high extinction polarizers to suppress the scattered light, but this method has the unfavorable outcome of losing polarization information from the PL. [74] Another possible method to obtain resonance fluorescence is to engineer semiconductor systems that are coupled to optical cavities where the excitation and detection paths are spatially separated. This eliminates the issue of having to resolve the PL signal from the large laser background. However, this method is limited to intricate sample fabrication which is in general resource intensive in addition, polarization is an issue here, as the cavities are polarization selective. [75]

4.3.3 Differential Transmission

Another class of methods that is also able to resolve minute energy differences is that of pure laser spectroscopy, such as differential transmission, which has the benefit of achieving laser-limited resolution with complete polarization information. This method typically requires lock-in detection to observe minuscule changes in the transmission signal compared to that of the large laser background. [77] Lately, advances in nanofabrication have led to a boost of the fraction of laser light that interacts with the QD(s) to values up to 20%, by either using index-matched solid immersion lenses or embedding the dots in photonic crystal waveguides. [78]

Even though these methods have the capability of achieving high energy resolution, they come at the cost of expensive equipment, complex sample fabrication and loss of information. The method in this chapter combines elements from these three methods without adding complexity in instrumentation or sample fabrication to a regular PL setup.

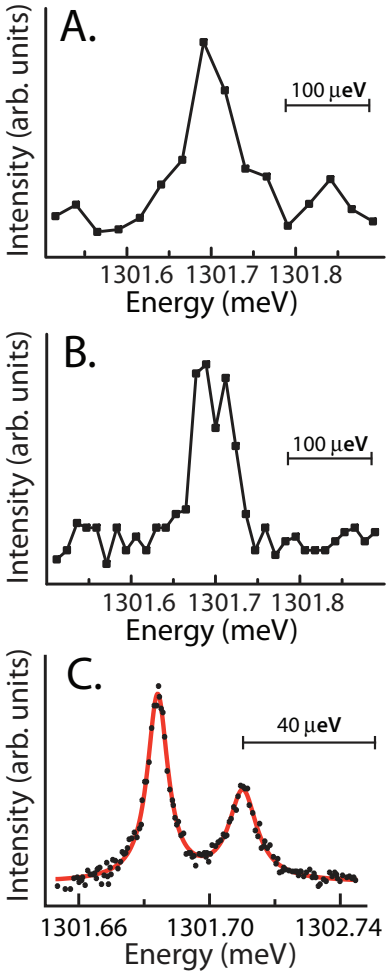

Figure 4.3: Spectral Resolution Comparison of Three PL-based Methods Example of the achievable resolution using different methods; in A and B, the spectrometer gratings and the CCD pixel width limit the resolution. All three scans are of the neutral exciton A) Single spectrometer with non-resonant excitation around 918nm. The spectral resolution is about 26 μeV per pixel. B) The same spectral region and excitation as in (A) but with the spectrometer set in triple additive mode, where the resolution is 10 μeV. C) Neutral exciton transition as resolved by using the quasi-resonant phonon assisted spectroscopy method. The two peaks are well resolved and fit by a double Lorentzian function, which yields an e-h exchange splitting of $23.3 \pm 0.1\mu$eV. The extracted FWHM values for lower and higher energy peaks are $7.3 \pm 0.1\mu$eV and $9.6 \pm 0.4\mu$eV, respectively.

4.4 Method

We will focus on a simple spectrometer setup that will incorporate many of the advantages that the other high resolution methods possess. Additionally the CCD will remain as a multi-channel detector. The experimental setup can also be kept fairly inexpensive relative to other high-resolution spectroscopy methods. The underlying key is to make use of the LO-phonon satellite associated with the semiconductors and related alloys that make up semiconductor samples. The energy separation between LO-phonon satellite and the zero-phonon line (ZPL) is on the order of tens of meV for such samples, allowing the use of a single-stage spectrometer. [79] This energy separation allows for use of the proposed quasi-resonance spectroscopy method by resonantly driving a transition and monitoring the -1LO photon emission below the excitation by an energy equal to one LO phonon. This technique is analogous to that of PL excitation where one excites into an excited transition and monitors the ground state transition. [80] The separation between the transition being excited and that of the LO-phonon satellite allows for the use of edge pass filters to suppress the elastically scattered light. This method of using the phonon satellite provides laser line-width limited resolution, since resonantly exciting the transition is typically the only time that the LO-phonon satellite emission becomes visible. The complete protocol of the procedure can be found in Appendix A.

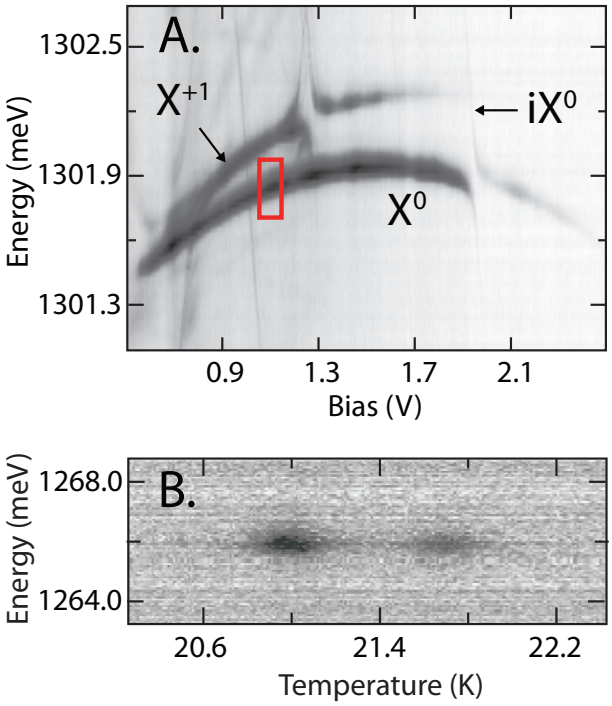

Figure 4.4: PL map of a QDM and associated phonon assisted measurement A) Regular resolution bias map of the QDM under non-resonant excitation. The bias map shows emission from the neutral direct (X0) and indirect (iX0) exciton, as well as the positive trion (X+). Also, the bias at which the laser is scanned through is indicated by the red box at around 1.1 V. B) High resolution PL at -1 phonon satellite below the excitation through the direct neutral exciton. The transition energy was tuned through a fixed laser energy of 951.657nm (1302.824 meV) by stepping the temperature. The -1 phonon satellite is seen to be about 36 meV below the zero phonon lines.

4.5 Results

By exciting into a QD discrete state, one can monitor the phonon emission line, achieving high resolutions. Figure 4.5 provides a schematic representation of the phonon-assisted method. With the laser exciting a discrete state the monitoring of

the PL is done one LO phonon energy below. This method has many similarities with Raman spectroscopy where the inelastic scattering of monochromatic light gives information regarding the vibrational modes in a system. In the example provided, by using phonons it is even possible to resolve the lifetime-limited linewidth of the neutral exciton visible in experiments. The method is easy to incorporate into existing PL spectroscopy setups. As mentioned, once the energy of the desired transition line is identified via non-resonant spectroscopy, the center wavelength of the spectrometer is established by setting it -1 LO phonon below that transition. This energy difference is used to make the measurement by employing short pass and long pass filters on the excitation and detection path, respectively. The filters are necessary to suppress any side modes of the laser light that might reach the spectrometer due to the relatively close proximity of both the excitation and detection energies. This reduction of stray laser light is a crucial element that maximizes the detected signal.

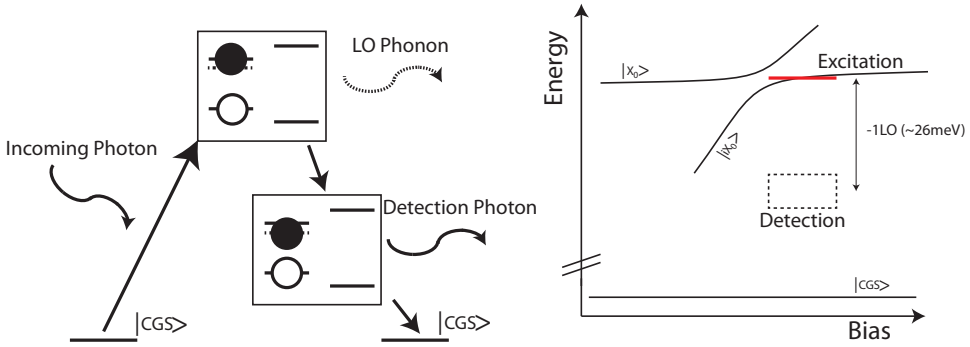

Figure 4.5: (Left) Schematic of the phonon assisted process. An empty QDM absorbs a photon generating an exciton in the metastable ground state. The exciton loses an LO phonon amount of energy to a lattice vibration dropping the exciton into a virtual state where resulting recombination has an energy of -1LO of the transition. (Right) Schematic representation of where excitation and detection occurs.

By tuning the laser through the transition energy, the -1 phonon satellite will emit when the laser is in exact resonance with the desired transition; this is due to the -1 LO phonon being a higher-order process. This crucial feature of the measurements is what allows for the experimental system to have laser limited resolution. Scanning the laser through the transition can be completed in two different ways.

4.5.1 Laser Tuning

The first way is to use a tunable diode laser that allows to tune the excitation energy across the discrete state. Using a tunable diode laser allows for tuning the excitation energy step size by which the laser can be varied, along with the laser linewidth these laser features govern the resolution that will be achievable.

4.5.2 Transition Tuning

Alternatively, a second method is to keep the laser energy fixed and scan the transition energy. In most systems this can be achieved in two different ways: first, by changing the sample temperature, which tunes the band gap as described by the Varshni law and consequently sweeps the transition energy through the excitation; [62] second, by applying an electric field, which Stark shifts the exciton transition energy and allows tuning of the transition through the laser energy. [81] A useful feature of the Stark shift method is higher spectral resolution for smaller Stark shifts; this is due to the laser-limited nature of the measurement.

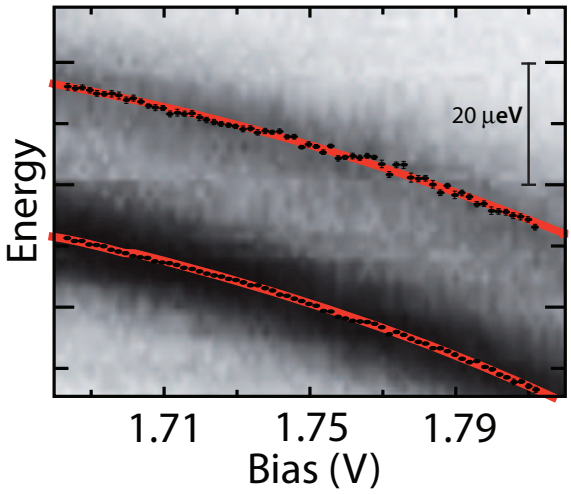

Figure 4.6: Bias Map of Anisotropic e-h Splitting Bias map of the anisotropic e-h exchange splitting, centered at 1302.28 meV. The bias map was made by incrementing the voltage applied by 2 mV increments at each laser energy and stepping the laser energy 37 times across the energy range, roughly changing about 1.7 μeV in each step. The average of the e-h exchange energy is 25.4 eV with a standard deviation of 0.8 μeV over this bias region. The fitting of the Stark shift is displayed.

This optical spectroscopy method has many favorable properties. It is a convenient method of investigating the anisotropic e-h exchange splitting energy, lifetime-limited line width and has the potential to resolve even smaller energy differences. Another favorable aspect of this experimental technique is that full polarization information can be accessed. In the presented example of a coupled QD, the neutral exciton ground state has a bright doublet that is distinguished by its spin configuration. The degeneracy of this doublet is lifted in QDs due to strain and shape anisotropies. Electron-hole anisotropies for these samples range from near zero up to tens of μeV. If both branches of the e-h exchange splitting doublet are excited, polarization information in the photoluminescence can be obtained by utilizing a polarization analyzer, consisting of a polarizer and variable retarder in the detection path. This is due to the phonons not carrying any spin information, [18] thus the complete polarization information of the spectra would be contained in the optical emission. On the other hand, using this setup allows for selective polarization excitation by having the liquid crystal retarder rotate the polarization on the excitation side to coincide with individual branches of the splitting. Polarization control is achieved by adding both a variable retarder and linear polarizer in both the excitation and detection paths. This allows for excitation and detection of select polarizations, giving both absorption and emission polarization information about the sample.

The main limitation of this high resolution measurement method is the restriction to materials that support optical phonons, such as semiconductors. For such a measurement to be completed, the material must have an optical phonon energy associated with it, since this energy difference enables performing the measurement with a standard single spectrometer. This method allows for taking high resolution spectra of quantum dots and other zero-dimensional systems. For example, the method can just as well be applied to study atomic defects in materials, such as nitrogen vacancy centers in diamond and defects in silicon carbide. [82] [83] While the method works great for low-dimensional semiconductor structures, it is not necessarily of benefit to the study of other structures or materials, as spectral broadening may eliminate the need for high resolution or coupling to LO-phonons may be too weak. Aside from these limitations the measurement technique holds several advantages over the other

methods mentioned in the manuscript.

Recent work has also shown that this method can be incorporated with a triple spectrometer system in subtractive mode, it is possible to visualize the singlet-triplet fine structure in the two-photon transition spectrum of a quantum dot molecule (QDM). [84] The involved energy splitting on the order of a few to tens of μeV were resolved using a triple subtractive mode, which allowed to excite the transitions resonantly and detect within less than a meV. The spectral information was extracted by monitoring below the transition using acoustic phonons and other lower-lying exciton transitions. This method can also be applied to resolve the anisotropic e-h exchange splitting and even the lifetime-limited line width of the exciton transition of 8μeV and 4μeV, respectively as seen in figure 4.7.

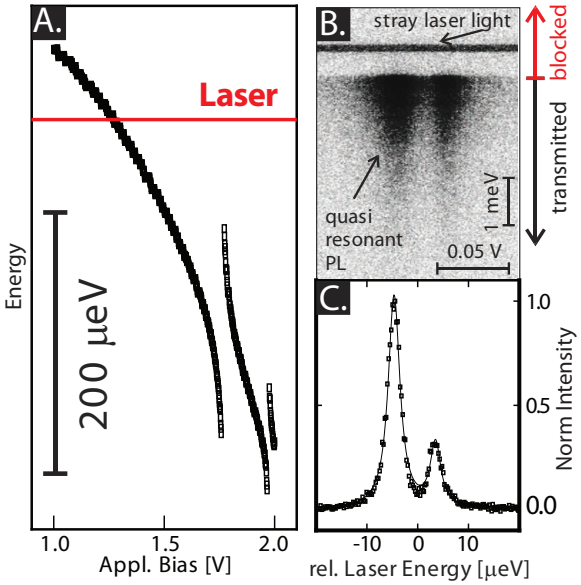

Figure 4.7: Acoustic Phonon Assisted Measurement A) Peak intensity of the ground state neutral exciton of a QDM as seen in photoluminescence. The red line indicates the quasi-resonance excitation. B) PL in the tail of the exciton transition as the transition is tuned into resonance with the laser. Using a triple spectrometer in triple subtractive mode the excitation and detection are separated by less than a meV. C) Summed quasi-resonant PL from (b), shows that it is able to resolve the features of the anisotropic electron hole splitting and the lifetime limited line-width of the transition.

4.6 Conclusion

This chapter has demonstrated a highly functional resonant fluorescence spectroscopy method, providing laser limited resolution with standard PL gathered by a single stage spectrometer by using material properties of the -1 optical phonon satellite. This method is a powerful tool with many uses in resolving energy features that are less than 10 μeV while retaining polarization information in the collected spectra, as demonstrated by resolving the anisotropic e-h exchange splitting of QDs. It has many advantageous features and can be used to study a large variety of different nanostructures that have optical and acoustic phonons.

Chapter 5

Phonon Induced Transparency

A common theme and major research question of this dissertation is gaining a better understanding of different resonant interactions that arise in semiconductor QDMs spectra. This chapter focuses on the resonance between a continuum of states and a discrete state, which enables a coherent quantum interference. The underlying physical effect is a widespread phenomenon in physics, which has gained interest in the solid state research community over the past few years. [85] [86] [87] This resonant interaction is called the Fano effect. The work presented in this chapter was published in 2014 in Nature Communications. [80]

The Fano effect is observed in a wide range of spectroscopy studies; [88] [89] [85] it is apparent in atoms, solids, semiconductor heterostructures and a number of other nanostructures. From atomic physics, nuclear physics, condensed matter physics, circuits, microwave engineering, nonlinear optics, nanophotonics the Fano effect is exhibited throughout them all. The original paper [90] describing this resonance phenomena has become one of the most cited papers in science since the 1980s. It has been shown that Fano resonance is a universal phenomenon and its presence exists in a number of systems regardless of material. [91] [92] [87] The Fano effect is an example of a resonant scattering process that gives rise to an asymmetric line-shape in the spectra. This asymmetry arises due to two competing pathways between a discrete state and a continuum of states; when the two pathways are at resonance in a certain parameter regime the asymmetric line shape is observed. The line shape

can be described with three parameters; the first parameter being the composite Fano parameter q, the second being the central energy position and the third being the width. All these parameters will be explained with more detail in the coming sections.

5.1 Background

The Fano effect is named after Italian physicist Ugo Fano who first explained the effect. He came to view this effect in photoionization spectra of helium. It is a very prominent phenomena throughout all of atomic, molecular and optical physics, as well as condensed matter. Though the phenomena was first observed by Ettore Majorana, [93] it was named after Fano due to his qualitative explanation of the phenomena. Ugo Fano in his 1961 paper, [90] claimed that the interference of a discrete state with a continuum gives rise to the asymmetric peaks in the absorption spectra of helium. Fano noticed this and came up with a theoretical fit to the shape of the 2s2p P resonance of helium from the inelastic scattering of electrons. [90] He extends this theory to the interaction of one discrete state to two or more continua and also to a set of discrete states to a single continuum.

Fano's theory also gives rise to the position and intensity shifts that are produced in a Rydberg series of discrete levels by interaction with a level of another configuration. The asymmetric line shape arises from the quantum interference that takes place between two competing optical pathways.

Fano's original theory pertained to the linear regime at low power. The Fano effect leads to the asymmetric profile due to interference between resonant and background scattering probabilities. The following is a description of the effect as provide in the reference. [94] The scattering cross section can be described by:

$$\sigma = \frac{(\varepsilon + q)^2}{\varepsilon^2 + 1} \tag{5.1}$$

This defines the Fano profile where q is the shape parameter or coupling parameter

and ε is the reduced energy. The reduced energy is

$$\varepsilon = 2\frac{E - E_f}{\Gamma} \tag{5.2}$$

were E_f is the resonant energy and Γ is the width of the resonance. To be able to compare different values of q then it is necessary to normalize the value of the Fano profile by dividing by $(1 + q)^2$. This gives an expression for the normalized Fano profile [95]

$$\sigma_{norm} = \frac{1}{(1 + q^2)} \frac{(\varepsilon + q)^2}{\varepsilon^2 + 1} \tag{5.3}$$

The plots for the three different Fano parameters is presented in figure 1. For the three cases presented the first has a very large q parameter this is the weak coupling regime. As q approaches infinity the discrete state dominates giving a Lorentzian linewidth. The second case is when the q parameter is greater than zero the classic asymmetric line shape exists. The last case is when q = 0, an antiresonance exists, there is a prominent antiresonance centered at the reduced energy of the system.

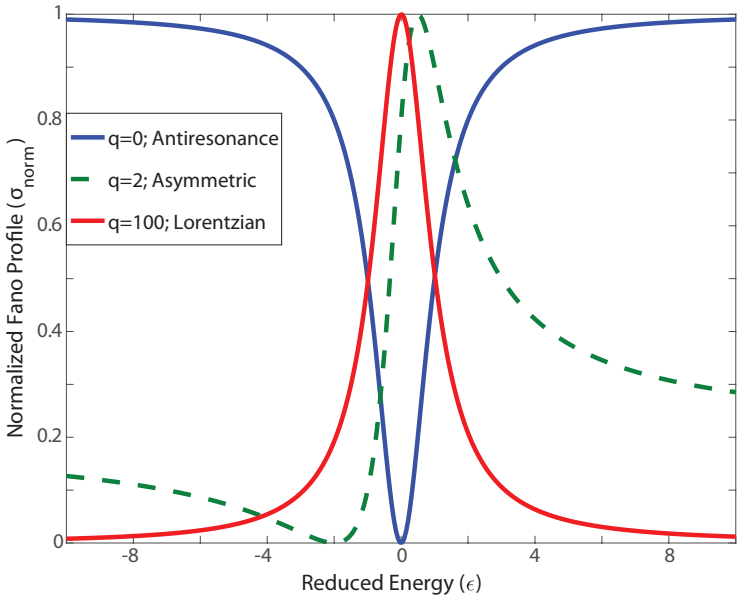

Figure 5.1: Fano line shape for different Fano parameters. A Lorentzian line shape is visible for large Fano parameters, for small Fano parameters the line shape resembles an antiresonance, and for values in between the classic asymmetry is portrayed.

5.2 Recent Fano Resonance Research

Fano resonances are visible in a number of physical systems. Previously the study has been limited to gas types and atomic transitions. Now we can apply it to a number of nanostructured materials, [91] [92] [87] especially since the technological abilities to engineer these structures to exploit competing optical pathways between discrete and continuum states are possible.

Most recent research has been done in the nonlinear Fano regime with the energy scale being rescaled to the near infrared. It is this non-linear high power regime where the mixing of states becomes very peculiar and rich with physics. Exploitation of the Fano resonances show that it is possible to use this phenomenon as a method of control over the electronic transport properties of a nanostructure. [96] [92] Even the possibility of new devices in the fields of quantum electronics or spintronic devices could exploit Fano interference. [97] Some devices could be Fano-transistors, spin

transistors and Fano filters for polarized electrons. Fano phenomena can also be used for lasing without the need for population inversion. [98]

From the educational standpoint Fano resonances are on par with other crucial wave phenomenas in modern physics such as Youngs interference in optics, and Aharonov-Bohm interference in quantum mechanics. The original manuscript on the Fano effect written by Ugo Fano describes the qualitative understanding of the autoionization process for helium. In his manuscript he provides the proper formulation of the observed asymmetric peaks that arise in helium absorption spectra. Fano does this by showing that the line shape occurs from the competing optical pathways, between a discrete state and a continuum. He derives quantum mechanically the Fano resonance formula as shown earlier and it demonstrates that the coupling parameter q is what defines the line shape. [90] Figure 5.1 displays the competing optical pathways that are present when a discrete and continuum of states are in resonance.

Recent research shows that the nonlinear Fano effect greatly changes as a function of excitation energy and power. [99] These asymmetric line shapes are readily available. At much higher powers there is particularly interesting physics occurring with the laser admixing with a number of states. This becomes apparent in the interplay of coherent nonlinear transitions. Kroner et. al. accesses the nonlinear Fano effect in engineered semiconductor quantum dots which have been grown via molecular beam epitaxy with a nearby continuum near the quantum dot. They showed that it is possible to engineer nanostructures where a QD with discrete energies is near a continuum of states. In which they could study the nonlinear Fano effect, by tuning the discrete energy levels in resonance with that of the continuum. Another claim that the paper makes is that the correlation between increasing power makes the Fano effect more pronounced by increasing the coupling of the two states and hence increasing the coupling parameter. [99] And they show that with the discrete states being tuned through the continuum at increasing powers the line shape becomes more asymmetric; which means that the discrete states and continuum's coupling are increasing. This paper gave great insight into the potential of making engineered nanostructures that could exploit the Fano resonance and open avenues to be used in devices. [99] This research is very comparable and in a very similar system as the research presented in

this thesis.

Another recent portrayal of the Fano effect gave evidence of the Fano effect in plasmonic nanostructures and metamaterials. [100] The paper is a review of new systems that have been studied and portray the Fano effect. Some of these systems such as plasmonic nanoparticles, are nanoparticles where the plasmons, the free electron oscillations that are causes by interaction with the electromagnetic waves cause interesting scattering and absorbance properties. Another unique system is photonic crystals which is a periodic optical nanostructure that effects the motion of the photons. And lastly electromagnetic metamaterials which are custom engineered structures that provide novel electromagnetic properties that can not be found in nature. All these systems show evidence of Fano resonance profiles and they promise to open a number of new potential applications in sensors, lasing, switching, nonlinear and slow light effects. This leads to the current research comprised within this thesis. This Fano interference in nanostructures such as the QDMs studied in this dissertation have the potential of also leading to a number of new potential applications by using the effects that will be described in the coming sections such as transparency and amplification of weak channels.

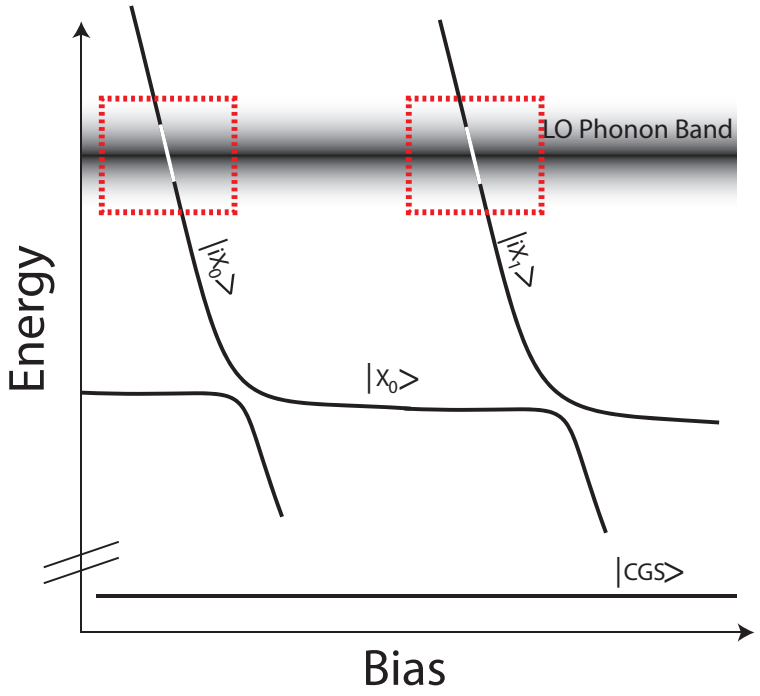

Figure 5.2: Schematic representation of the spectra of a QDM with the indirect transitions of interest labeled. Here the direct and indirect transitions of the neutral exciton are displayed along with the continuum of states of the optical polaron band. The region of interest where the formation of a molecular polaron are observed are in the boxed region where the discrete states of the indirect exciton intersects with the polaron band.

5.3 Fano Effect in QDMs

Semiconductor QDMs that were studied are described in chapter 2. Spectroscopy of the QDMs leads to the observation of Fano resonances that are clearly visible.

The Fano resonance in this system like other systems is between a discrete state and a continuum. The discrete state we refer to are one of the indirect neutral exciton states and the continuum is the LO phonon band. Both of these states are coupled to a common ground states. The benefit of using the QDMs indirect neutral exciton state is that thanks to their high tunability as a function of field, as mentioned in chapter 2, allows for their energy to be tuned across many meV which gives the possibility of tuning the indirect exciton in resonance with nearby continua. The closest continuum

to the ground state energies of the different charge ground states is the polaron band. The polaron band a hybridized phonon and electronic state which was described in greater detail in chapter 1. The polaron band of concern is the longitudinal optical phonon coupled with the neutral exciton. Figure 5.2 shows a schematic of the excited state (transition) spectrum of a QDM. In the spectra the indirect excitons with their large slope have the ability to be tuned across the polaron band. It is at this resonance that the Fano effect and Fano interference is clearly visible in the QDM system.

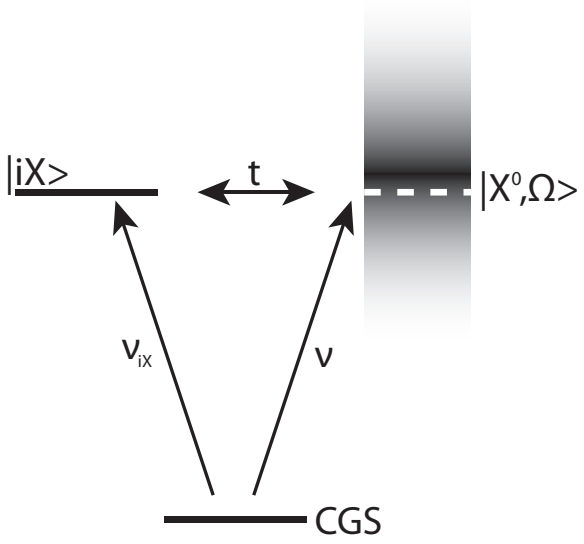

Figure 5.3: Model of the discrete indirect exciton and the optical polaron made up of a discrete exciton with phonon mode states both coupled to the crystal ground state that leads to a Fano resonance in the PLE spectra.

Figure 5.3 shows the states that are at play. Both states couple optically to a common ground state which is the crystal ground state (CGS). The discrete state of the indirect exciton is labeled $|iX_0>$. Though the diagram is only showing this for the ground state indirect exciton, the Fano resonances has been seen and is possible with any of the many excited indirect exciton states. The continuum state on the other hand is denoted by the LO phonon band, this polaron state is due to the neutral exciton ground state and a single optical phonon mode denoted by $|X_0, m>$ where the m describes an arbitrary phonon mode associated with it. Thus this process is viewed as a phonon assisted process. The addition of the optical phonon makes

the state continuous due to the dispersion of optical phonons. And when both the indirect exciton and polaron continuum are in resonance the final hybridized state is the molecular polaron state $|MP>=|iX_0>\pm|X_0,m>$. Figure 5.2 denotes theses states in pictographic form. Having the discrete state which is highly tunable in energy and the polaron continuum fulfills the one requirement for the Fano effect. With the high tunability of the indirect exciton it allows to tune the two states into resonance thus portraying the Fano resonance.

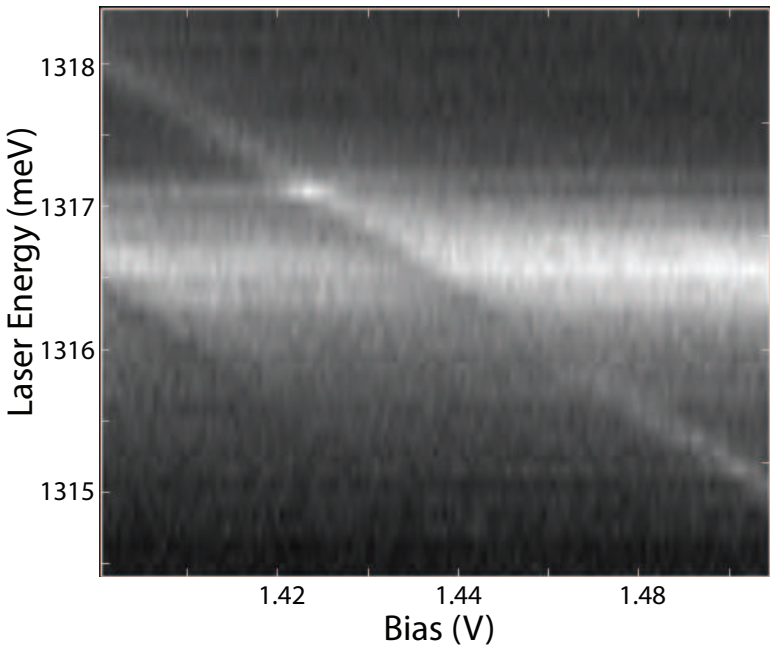

Figure 5.4: Fano interference between an indirect discrete state and polaron band. At the resonance between the continuum of states and the indirect exciton a transparency is visible.

5.4 Experiment

The optical methods used for the extent of these experiments were both PL and PLE spectroscopy as described in chapter 3. Fano interference has been viewed in a number of QDM, all of the QDMs exhibit the Fano effect at the optical phonon band. The data presented in this section is for a single QDM with 4nm barrier. [80] Figure

5.4 shows the PLE of the QDM of interest. At approximately 35.5 meV above the ground state neutral exciton the LO phonon band is clearly visible. As mentioned in chapter 2, it is the bias voltage that is able to greatly Stark shift the indirect states due to the large dipole moments. This in turn allows to tune the indirect states with the polaron continuum. In this polaron continuum a number of indirect exciton states come into resonance with the polaron band. The process is described as an indirect exciton being excited, the excited state then relaxes by non-radiative means, to the ground state which is detected. Similarly when exciting into the polaron continuum, non-radiative relaxation occurs with the emission of an optical phonon. Using PLE spectroscopy, the optical absorption of the excited states is in turn plotted for the varying laser excitation and bias values.

5.4.1 Experimental Parameters

The parameters for the experiment are defined by the energies and bias that the indirect exciton of interest and continuum have. The region of interest is at the resonance of the indirect exciton and polaron continuum. The laser was set to scan through the entirety of the polaron continuum. The laser step resolution achieved is around 0.1 meV per step due to the mode hop of our tunable diode laser. The voltage range was scanned from 0.5 to 2 V and the bias step size was able to reach as little as 1 mV steps. The CCD integration time for the PLE scans was set anywhere from 1 to 5 seconds. For resolving the anticrossings in the ground state exciton's PL integration times of as much as 120 seconds were used. These anticrossings at the high bias have weak spectral strength and require much longer integration times to be able to resolve. With the anticrossings visible the LACS method allows to identify the indirect neutral excitons ground state and excited states. Each corresponding anticrossing is a higher state and this allows to label the indirect excitons that are resonant with the phonon band. This is necessary to be able to fully map out the different excited states of the indirect neutral exciton. Level anticrossing spectroscopy [61] uses PLE to be able to map the full level diagram of the excited states of a QDM. This PLE method along with the anticrossings in the ground state allow for the ability to identify which

excited state level of the indirect exciton is crossing the polaron band.

5.5 Experimental Data

5.5.1 Phonon Induced Fano Interference

In the overview PLE spectra two polaron continua are clearly visible figure 5.5 The first continuum exists at 30 meV, the LO phonon energy of InAs, above the neutral exciton ground state. The second band is at 35 meV above the ground state and is attributed to the LO phonons associated with GaAs. These polaron bands are visible in figure 5.5. Similar to the original works of Ugo Fano, a number of discrete states can either come into resonance with the polaron band or a single discrete state which can also have a Fano interference effect with multiple continua. In semiconductor QDMs both of these cases are readily observed. Within the two polaron bands individual indirect states can interfere with both bands. Along with interference of a number of the indirect excited discrete states with a single polaron band.

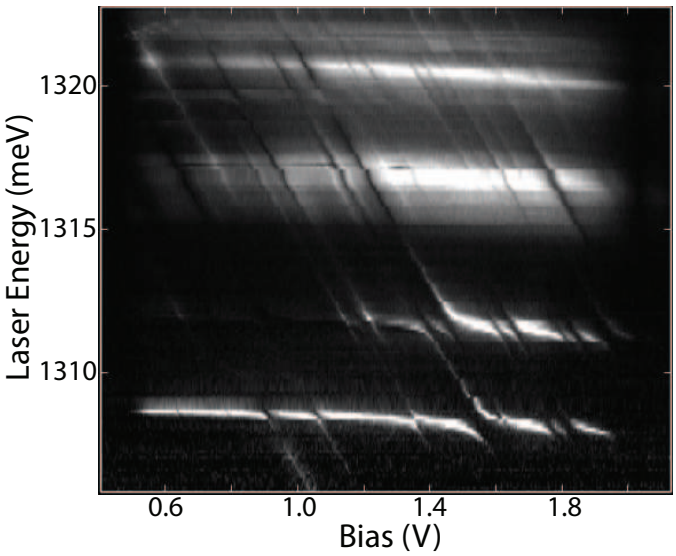

Figure 5.5: Excited state spectra of a QDM. Both excited states of the neutral exciton are visible along with the continuum of the optical polaron band. Fano resonances are visible at the intersections of the the indirect exciton and optical polaron band.

In the data and figure the different indirect excited states have been identified by the level anticrossing spectroscopy technique. This has been done for the neutral exciton of interest. Multiple excited states of the indirect neutral exciton have been identified. Theses indirect lines have a slope of 18.5 meV/V, and they are clearly seen in the PLE spectra. As the indirect neutral excitons cross the polaron band a decrease in intensity is seen; this Fano interference is not simply an addition of both the polaron and discrete state emissions.

Monitoring the various Fano interferences show many different Fano parameters at different excitation energies. Figure 5.6 shows the PLE spectra and various Fano parameters associated with the interference. At varying energies where the indirect state and continuum interact producing different q_{fano} parameters. This can be explained by the optical states having different coupling parameters between the indirect state and continuum. From the data Fano parameter values ranging from very small to large are seen, along with negative q_{fano} that just symmetrically flip the line profile.

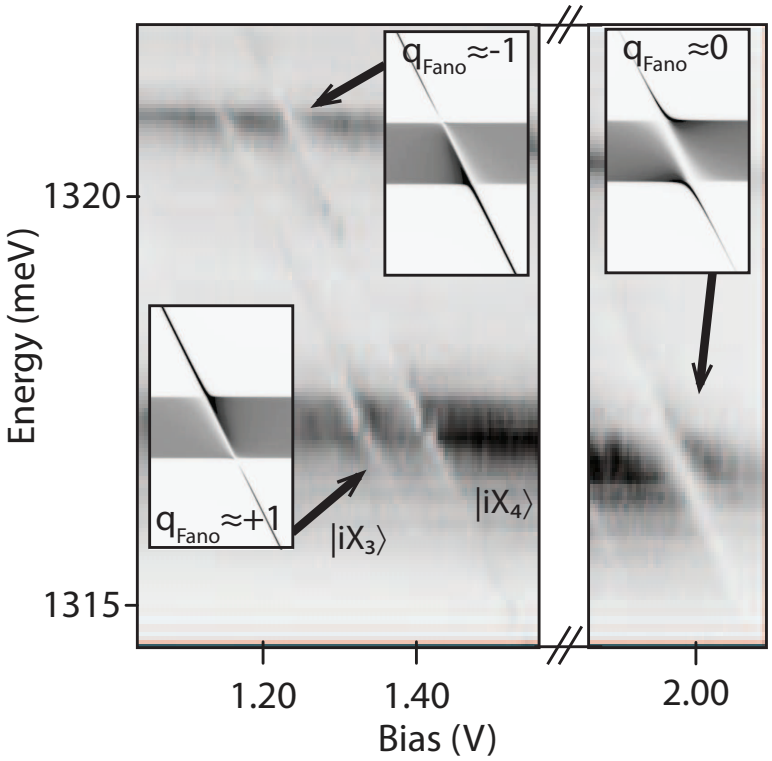

Figure 5.6: Experimental data showing Fano resonances at the polaron continuum for different Fano parameters. Inserts show the theoretical calculation of the Fano interferences and the corresponding Fano parameter.

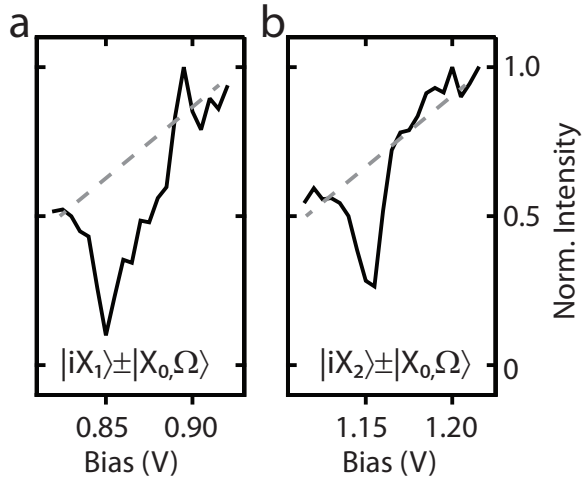

Figure 5.7: PLE spectra line cuts of the Fano interference through the polaron band. The line cuts of the spectra can show deep antiresonances where the absorption of the indirect exciton is reduced by up to 75% below the intensity of the background. a) The Fano transparency of the first excited indirect neutral exciton state, and b) The second excited indirect neutral exciton state.

5.5.2 Non-linear Fano Effect

The Fano effect can be tuned optically, by varying the power the driving states into the individual states can be controlled. The Fano interference is minimal at low laser powers. This is seen in figure /5.9 and 5.10 at low laser powers the line profile of the indirect transition becomes the typical Lorentzian profile for a discrete transition. But as the power increases the line shape changes to the asymmetric line shape typical of Fano interference. This non-linearity of the Fano effect can be explained by the different absorption pathways response to the excitation power. For a single excitation energy at the resonance point of the indirect state and continuum of states the state diagram is shown in figure 5.3. At low powers the transition of ν_{iX} of the indirect exciton and that of ν into the polaron band is minimal. This is due to minimal interaction between the two states. But as the excitation power is increased the line shape of the spectra becomes more asymmetric as is typical with the Fano line shape. This can be understood by looking at the transition amplitude of the different transitions. For the indirect exciton as the power increases it can saturate the indirect

state and the transition amplitude approaches to a constant value. Whereas on the other hand, the transition amplitude ν into the polaron continuum continues to grow at the higher excitation powers. This leads to greater phonon transparencies at greater excitation powers and a decrease of the Fano parameter.

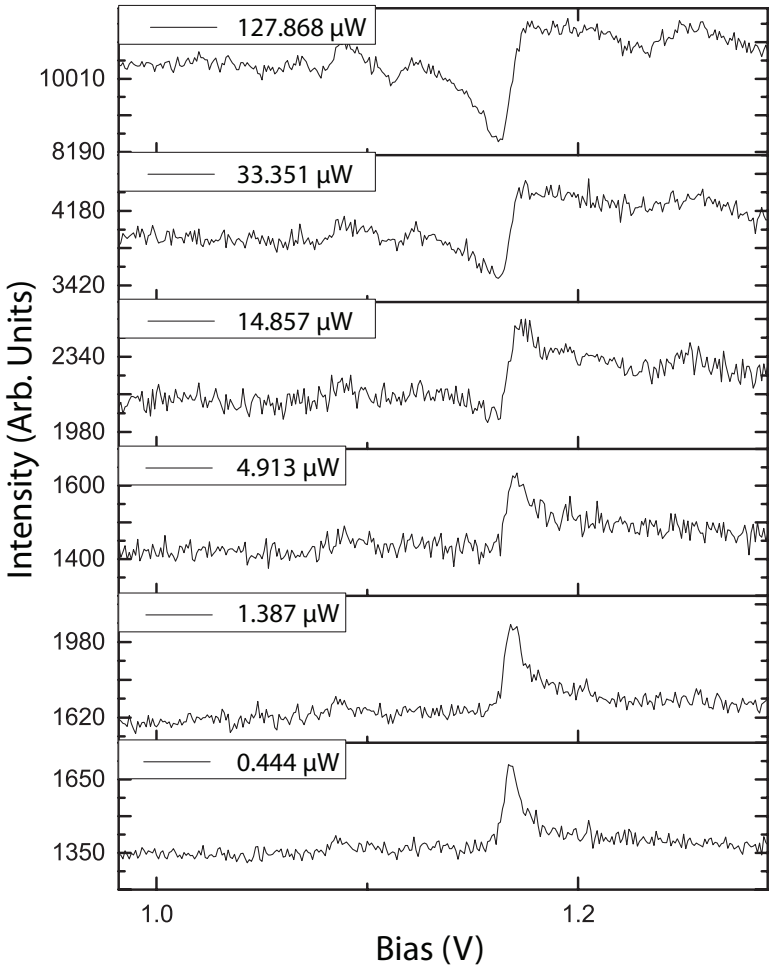

Figure 5.8: Non-linear Fano Resonance's power dependence where a through e are decreasing lase powers. At lower powers the Lorentzian profile dominates due to coupling with the discrete state dominates.

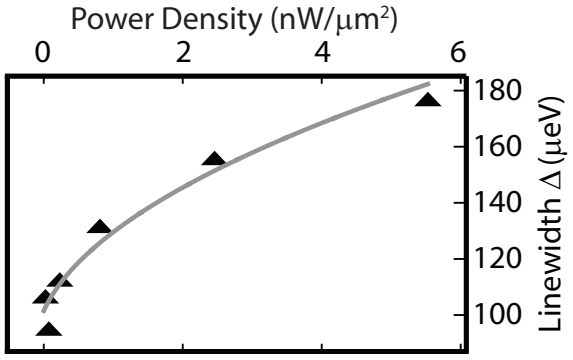

Figure 5.9: Line width as a function of excitation power density from fits of the indirect transition.

5.5.3 Fano Amplification

A nice feature of the non-linear Fano effect is that with the various parameters (i.e. excitation power, excitation energy, bias) it is possible to tune the parameters to adjust the Fano parameter. We can increase the coupling between the indirect exciton state and the polaron continuum by just tuning parameters such as the power. The ability to adjust the coupling can lead to using these parameters to amplify very weak optical channels. This can be seen were a very weak indirect neutral exciton that is practically undetectable is greatly amplified at resonance with the continuum of states. In figure 5.10 it is shown that outside the polaron band the relative intensity of the indirect exciton states over background is much weaker than when in resonance with the polaron band. Hence, the Fano interference amplifies and makes very faint small signals much more visible. Amplifications of 25 times have been seen at large excitation powers.

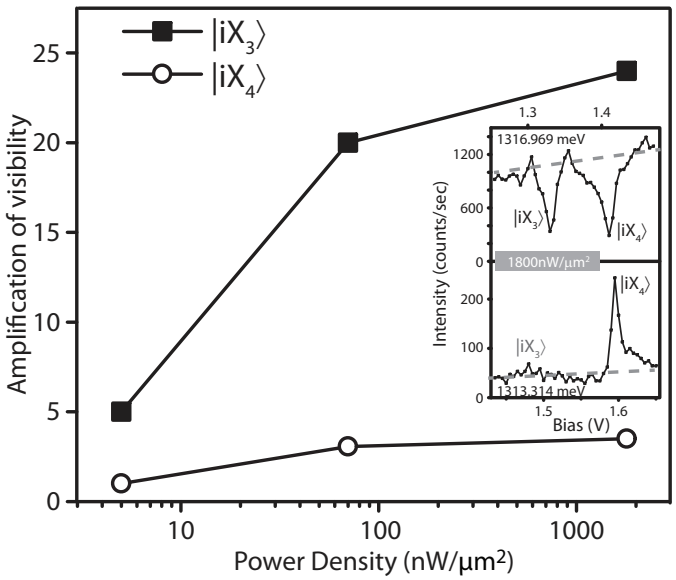

Figure 5.10: For the $|iX_3>$ and $|iX_4>$ shows the amplification of the signals over background when in resonance with the phonon band at varying powers. Inserts plot the states below and at resonance with the polaron band.

5.6 Theory

This phonon-induced Fano effect in QDMs has been modeled by a collaborator of ours Alexander O. Govorov from Ohio University. His model allows us to theoretically calculate the rate of absorption in a semiconductor QDM system, with the final result being the absorption line shape as a function of the Fano parameter. The set of states is shown in figure 5.2. Modeling the system the first step is to calculate Fermi's golden rule that describes the rate of the energy absorption for our states.

$$I(\omega) = \hbar\omega * W$$

$$W = \frac{2\pi}{\hbar} \sum_f | < f|v\hat{V}_{opt}|0 > |^2 * \delta(\varepsilon_f - E_{CGS} - \hbar\omega)$$

where ω is the photon frequency; and E_{CGS} is the crystal ground state that both the indirect exciton and polaron continuum are coupled to and we denote its wave

function as the $|CGS>=|0>$. The optical interaction operator is

$$\hat{V}_{opt} = V_{indirect}(\hat{c}^{+}_{CB,QD1}\hat{c}_{VB,QD2} + \hat{c}^{+}_{VB,QD2}\hat{c}_{CB,QD1})$$
$$+V_{direct}(\hat{c}^{+}_{CB,QD1}\hat{c}_{VB,QD1} + \hat{c}^{+}_{VB,QD1}\hat{c}_{CB,QD1})$$
$$V_{direct} = A_0 < \psi_{CB,QD1}|\psi_{VB,QD1} >$$
$$V_{indirect} = A_0 < \psi_{CB,QD1}|\psi_{VB,QD2} >$$
$$A_0 = -\frac{\mu_{cv}E_0}{2}$$

The optical interaction operator promotes the electrons from the ground state to the electronic states in both the QDs in the QDM. The second operator deals with electrons from the conduction and valence bands. The spatially direct and indirect optical transition elements include the wave function ψ , and the inter-band element A_0 where $\mu_c v$ is the inter-band atomic dipole and E_0 is the laser amplitude. Then using greens function $G(\omega)$ it is possible to define the function W as:

$$W = \frac{2}{\hbar} Im \sum_f G(\omega)$$
$$G(\omega) = \sum_f \frac{<0|\hat{V}^{+}_{opt}|f><f|\hat{V}_{opt}|0>}{\varepsilon_f - E_0 - \hbar\omega - i\gamma_f} = -<0|\hat{V}^{+}_{opt}\frac{1}{E_0 + \hbar\omega + i\gamma - \hat{H}}\hat{V}_{opt}|0>$$

With W defined we must now identify the electron-phonon operator that sum the interacting final states in the sum $G(\omega)$.

$$\hat{V}_{e-ph} = \hat{V}_{e-ph,QD1-QD1} + \hat{V}_{e-ph,QD1-QD2}$$

$$\hat{V}_{e-ph,QD1-QD1} = \sum_m (b_m + b_m^+) < \psi_{VB,QD1}|\Phi_m(r)|\psi_{VB,QD1} > \hat{c}^+_{CB,QD1}\hat{c}_{VB,QD1} +$$

$$+ \sum_k (b_m + b_{-m}^+) < \psi_{CB,QD1}|\Phi_m(r)|\psi_{CB,QD1} > \hat{c}^+_{CB,QD1}\hat{c}_{CB,QD1}$$

$$\hat{V}e - ph, QD1 - QD2 = \sum_m b_m^+ < \psi_{VB,QD2}|\Phi_m(r)|\psi_{VB,QD1} > \hat{c}VB, QD2^+\hat{c}_{VB,QD1} +$$

$$b_m < \psi_{VB,QD1}|\Phi_m(r)|\psi_{VB,QD2} > \hat{c}^+_{VB,QD21}\hat{c}_{VB,QD2}$$

Where b_m and b_m^+ are the phonon operators of modes m and $\Phi_m(r)$ are the *Fröhlich* potentials of the modes. For the QDM these come from localized phonon vibrations and are not known. Describing the weak electron-phonon (polaron) interaction for the exciton in QD1 we have $\hat{V}_{e-ph,QD1-QD1}$, this weak interaction is needed to describe phonon-assisted inter-band transitions in QD1. For the inter-QD operator of $\hat{V}_{e-ph,QD1-QD2}$, only the resonant terms are kept that describe the phonon-assisted tunneling between QDs. With this the final states can be calculated with electron-phonon operators and Hamiltonian of our system written as:

$$\hat{H} = \hat{H}_0 + \hat{V}_{e-ph,QD1-QD1} + \hat{V}_{e-ph,QD1-QD2}$$

The purely excitonic Hamiltonian is denoted as $\hat{H}_0$. To make the diagrammic calculations simpler diagonalizing the Hamiltonian by including only the intra-dot polaronic operator $\hat{V}_{e-ph,QD1-QD1}$ as a small perturbation. Then the states become:

$$|0>=|0_{CB,QD1};1_{VB,QD1};1_{VB,QD2}>|0_{phonons}>+$$
$$+\sum_m a_m|0_{CB,QD1};1_{VB,QD1};1_{VB,QD2}>|m>$$
$$|1>=|1_{CB,QD1};1_{VB,QD1};0_{VB,QD2}>|0_{phonons}>+$$
$$+\sum_m a_m|1_{CB,QD1};1_{VB,QD1};0_{VB,QD2}>|m>$$

The state $|0>$ is the common crystal ground state and $|1>$ is an exciton state in QD1. Both these states gain a polaronic wave function written from the regime of weak electron-phonon interaction. With the new states it is possible to calculate the optical amplitude for the polaron state $|X_0;\Omega_{ph,b}>$

$$v_m =<1,m|\hat{V}_{opt}|0>=A_) <\psi_{CB,QD1}|\psi_{VB,QD1}>\int dV\frac{\Phi_m(r)}{\hbar\omega_m}(\psi^2_{CB,QD1}-\psi^2_{VB,QD1}) \tag{5.4}$$

In terms of the new state the perturbation operator $V_{e-ph,QD1-QD2}$ and the total Hamiltonian is written $\hat{H}=\hat{H}_0^1+\hat{V}_{e-ph,QD1-QD2}$. This operator can easily be expanded:

$$\frac{1}{\hbar\omega+i\gamma-\hat{H}_0^1-\hat{H}_i nt}=$$
$$=\frac{1}{\hbar\omega+i\gamma-\hat{H}_0^1}+\frac{1}{\hbar\omega+i\gamma-\hat{H}_0^1}\hat{H}_{int}\frac{1}{\hbar\omega+i\gamma-\hat{H}_0^1}+$$
$$+\frac{1}{\hbar\omega+i\gamma-\hat{H}_0^1}\hat{H}_{int}\frac{1}{\hbar\omega+i\gamma-\hat{H}_0^1}+...$$

The interaction Hamiltonian takes the form of $\hat{H}_{int}=\hat{V}_{e-ph,QW1-QW2}$, now with the groundstates defined and $G(\omega)$ as a infinite series. The sum of the series can be expressed in the following equations:

$$G = -Im[\frac{(\nu_{ix} + \Sigma_{\nu t})^2}{\hbar\omega + i\gamma - \varepsilon_{iX} - \Sigma_{tt}} + \Sigma_{\nu\nu}]$$
$$\Sigma_{tt} = \sum_m (\frac{t_m t_m}{\hbar\omega + i\gamma - \varepsilon_m})$$
$$\Sigma_{\nu t} = \sum_m (\frac{\nu_m t_m}{\hbar\omega + i\gamma - \varepsilon_m})$$
$$\Sigma_{\nu\nu} = \sum_m (\frac{\nu_m \nu_m}{\hbar\omega + i\gamma - \varepsilon_m})$$
$$\varepsilon_m = \varepsilon_{X_0} + \varepsilon_{ph,m}$$

Here $\nu_{iX} = A_0 < \psi_{CB,QD1}|\psi_{VB,QD2} >$ and ν_m is the optical transition amplitude from the crystal ground state to the polaron state $|1, m >$ given earlier. The phonon assisited tunneling amplitude is taken from:

$$t_m =< 1, m|\hat{V}_{e-ph}|2 >=< \psi_{VB,QD2}|\Phi_m|\psi_{VB,QD1} > \tag{5.5}$$

We assume that the optical phonon bands have a flat density of states in the interval $\varepsilon_{ph,0} - D/2 < \varepsilon_{ph,m} < \varepsilon_{ph,0} + D/2$. This model matches up well with the experimental data which show the optical phonon band as stripes. This lets the sums be turned into integrals:

$$\sum_m (...) \rightarrow \int_{\varepsilon_{ph,0}-D/2}^{\varepsilon_{ph,0}+D/2} (...)\rho_0 d\varepsilon_{ph} \tag{5.6}$$

Now assuming the transition amplitudes are constant we obtain the Green's function and the absorption rate:

$$I(\omega, V_g) = -2\omega\pi v^2 \rho_0 * Im[q_{fano}^2 \frac{\Delta(1 + \frac{1}{q_{fano}} F(\omega))^2}{\hbar\omega - \varepsilon_{iX} + i\gamma_{iX} - \Sigma_{ph}} + F(\omega)] \tag{5.7}$$

$$F(\omega) = \int_{-D}^{+D} d\delta\varepsilon_{ph} \frac{1}{\hbar\omega - \varepsilon_{X_0} - \hbar\omega_{ph,0} - \delta\varepsilon_{ph} + i\gamma_{X_0\Omega}} \tag{5.8}$$

$$\Sigma_{ph} = \Delta_{ph} * F(\omega) \tag{5.9}$$

Where Δ_{ph} is the broadening of the indirect exciton due to its interaction with the phonon band. The q_{fano} is the Fano parameter that controls the asymmetry of the line shape. In figure 5.10 the theoretical plot of the line shape at varying biases for both indirect exciton and polaron band is plotted at varying applied voltages. Clearly seen is the discrete line of the indirect moves through the phonon band. Under certain driving conditions varying q_{fano} values are attainable and line shapes from anti-resonances, to asymmetries to Lorentzian profiles are attainable.

5.7 Conclusion

The Fano effect's asymmetric line shape comes from two competing optical pathways, one with a discrete state and the other with a continuum of states. Recent research has shown that the Fano effect is present in a number of different systems particularly with engineered nanostructures. The potential use for Fano resonance would allow for us to better understand a materials electronic transport properties and optical spectra with the potential to integrate it in a plethora of modern devices.

The chapter shows how within a QDM an indirect exciton can come into resonance with the optical phonon band a continuum of states and can lead to Fano interference. This arises due to the discrete state and continuum being coupled to a common ground state along with to each other. With the ability to modify a number of experimental parameters a number of different q_{fano} factors are attainable leading to numerous different attainable line profiles.

Asymmetric line shape is visible in the spectra. When driving the system at larger powers large optical transparencies up to 75% are seen. Along with this phonon induced optical transparencies the Fano effect can also be exploited in QDMs to amplify very weak optical channels such as these excited indirect states that are very short lived and weak. This research leads the way in addressing the idea that phonons which are normally viewed as negative attributes to quantum systems due their ability

of decohering quantum systems actually have advantages that can be exploited. Even paving the way to be used as an electric field driven control element for the flow of phonons like a phonon transistor.

Chapter 6

Optical Charging

This chapter focuses on optically selective charging of QDMs. We observe enhancement of the photoluminescence of charged excitons in the excited state spectra. These enhancements occur when exciting at resonances between the neutrally and singly charged excitons and indicates an optical charging process is occurring. By garnering an understanding of the overall system, in terms of the charge stability of the specific charge states along with the band structure alignment (i.e. considering the dot levels relative to the Fermi sea and each other), we will better understand the PL enhancement and the charge dynamics between the trion (singly charged) and neutral exciton states. Analysis of these resonances provides insight into charging dynamics of the QD(M)s and properties that will lead to better designs of QD(M) structures. The ability to manufacture structures with more efficient optical charging could be implemented in photonic circuit technologies. We present both the experimental results and mathematical model to describe this charging process.

6.1 Introduction

Optical generation of selective exciton emissions has many useful features such as the ultrafast and wireless generation and of a desired charge state. The ability to generate particular charge states in an ultrafast fashion could lead to applications in quantum cryptography, quantum information, and technologies involving photonic circuitry.

Under regular conditions, it takes some combination of the three different charging methods, optical, doping and electrical leads, (described in chapter 2) to produce a net charge on the QD(M). However, these methods of charging QDs have drawbacks; they have additional growth challenges and are slower than optical processes. The major challenge to optical charging is that optical excitation under standard conditions introduces electron-hole pairs, which maintain the QD(M)'s charge state. Additional challenges to overcome with optical charging are different charge states have emission energies that vary greatly due to Coulomb interaction between the electrons and holes within the QD, and non-resonant excitation leads to nondeterministic charging of the QD(M). Even under monochromatic excitation, a variety of QD(M) charge states are typically generated. This makes it impossible to deterministically prepare the QD(M) in a specific charge state by optical means. QDMs offer unique features over QDs that can circumvent these challenges. We present experimental data showing under certain conditions the possibility to optically generate a single charge state. Our observed optical charging of QDMs is explained in this chapter.

An interdot transition, as mentioned in chapter 2 are widely tunable in energy. By completely mapping out the excited state spectra and identifying the corresponding states [101] we can expand on the functionality of the underlying process, namely the tunneling of individual charges. [52] It is easy to see how tunneling between two dots of a CQD pair can lead to charging of the individual dots. The tunneling only needs to be unidirectional, leading to a separation of charges. The overall system, however, retains its charge state. For tunneling to lead to a net charging of the system, the number of charges must not be conserved between the two QDs, i.e., individual charges must be allowed to enter or leave the system. The question being proposed is if it is possible to promote or initiate this tunneling out of the QDM system by purely optical means. To better understand the optical charging it first is necessary to understand the charge stability regions for the various charge states.

6.2 Charging Plateaus

First, we investigate across what electric field range a charge state is stable. To understand the charge stability region of the different charge states it is necessary to look closely at the energy levels detuning from the Fermi level of the heavily n-doped substrate. It is important to note that at low reverse bias (0.5 V) the Fermi level is near resonant with the electron energy states of the bottom dot; this leads to higher probability of electrons tunneling into the bottom dot through the barrier. When a QDM starting with an electron in the system absorbs a photon this produces a negative trion state. The offset between energy levels and Fermi levels governs the likelihood of having an electron in the QDM. As the bias is increased the levels are even more detuned and the probability of electrons tunneling into the QD is much smaller. This feature and charging structure is clearly seen in the PL map, figure 6.2b. PL maps show the charging plateaus of the individual charge states, and these plateaus correspond to where they are most stable. As the bias is increased in reverse bias, the electron levels in the conduction band increase due to the band alignment, thus leading to them having a much larger detuning from the Fermi sea. This leads to it being less and less likely to find an electron in the QDM and leaving positive charge states to dominate at higher biases.

The visibility of different charge states is generally governed by their charge stability region. The charge stability occurs when an exciton charge state is in its lowest energy at a given electric field; this yields the strongest PL transitions. [56] The charge stability region is explained by looking at the band structure and the band alignment due to the applied bias. The relative intensity of the various resulting photoluminescence transitions depends on the overall band alignment of the structure the QD is contained in. By embedding the QDM in a Schottky diode structure, an electric field can be applied. With the electric field the charging of the different charge states follows the charging of a capacitor. Much like the honeycomb patterns found in electro-statically defined QDs charge stability regions can then be identified for self-assembled QDs. [55] At high electric fields the energy difference from the Fermi sea to bottom dots conduction band is large and it is easier for electrons to tunnel out

of the QDM. As the field is lowered it is more and more probable to find an electron in the bottom dot. Each charge configuration has a range of biases where it is most stable. Negative charge states are most stable at lower reverse bias fields, as the field is increased this raises the band alignment lifting the electron energy levels further away from the Fermi level. As the bias is increased this leads to it being unlikely to find electrons in the QDM. This charging structure is apparent in the PL maps of QDMs, figure 6.2.

6.2.1 Calculation of Charge Stability

A particular charge configuration's stability can be calculated by comparing the lowest energy for all the charge configurations of interest. We can distinguish the different charge configurations by $\binom{n_{eb} \quad n_{et}}{n_{hb} \quad n_{ht}}$. The calculations do not include tunneling and electron-hole spin exchange. The energy for a specified charge is given by

$$E\binom{n_{eb} \quad n_{et}}{n_{hb} \quad n_{ht}} = \sum_{i=B,T} \left(n_i^h(\varepsilon_i + \Gamma_i) - n_i^e\varepsilon_i + n_i - m_i\right) \times \frac{s_i}{L}\left(\frac{L\gamma}{d}U + \frac{\Gamma_{GaAs}}{2}\right)\Big) + ... \sum_{i,j=B,T;\alpha,\beta=e,h} (n_i^\alpha n_j^\beta - 3\delta_{\alpha\beta}\delta_{ij})V_{ij}^{\alpha\beta} \tag{6.1}$$

where we have $\delta_{\alpha\beta}, \delta_{ij} = 1$ when $\alpha = \beta, i = j$ otherwise $\delta_{\alpha\beta}, \delta_{ij} = 0$. Comparing the calculated charge stability regions with that of the experiments shows good agreement between the two at low powers, compared two figure 6.1. The parameters used for the fit are shown in table 1. With the charge stability results being shown in figure 6.1.

V_{TT}^{ee}	V_{BB}^{ee}	V_{TT}^{eh}	V_{TB}^{eh}, V_{TB}^{ee}
20 meV	16 meV	27 meV	10 meV
ε_B	ε_T	Γ_T	
110 meV	140 meV	1270 meV	
s_B	d	s_T	L
40 nm	20 nm	80 nm	369 nm

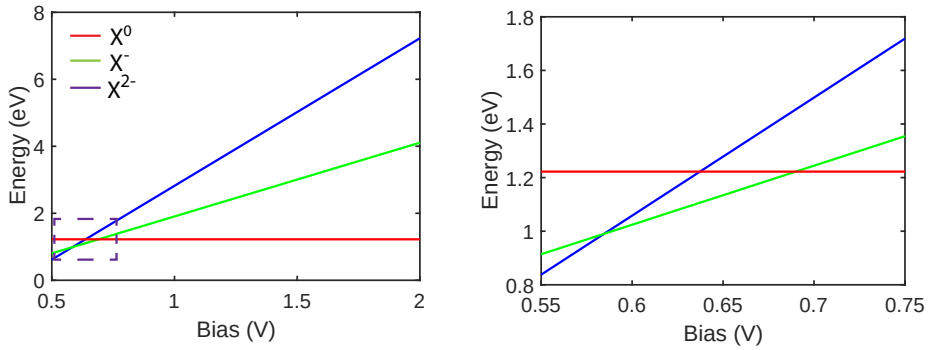

Figure 6.1: Calculated charge stability for X^{2-}, X^{-} and X^{0} states.

If we follow the charging of the QDM as a function of increasing bias we see in figure 6.2b that at low bias values the doubly negative exciton is the dominant transition in the spectrum, indicating that in this region an excess of two electrons is most stable. By analyzing the relative intensities of the different charge stability regions in a PL it is possible to compare the charge stability regions with that of the calculation. The calculated charge stability regions matches with the experimental values very well at low powers. But at large powers a discrepancy lies at the negative trion's region of metastability.

6.3 Experiment

Figure 6.2a shows a schematic representation of the excited state spectra for the neutral exciton X^0. In the spectra two excited neutral exciton states and a number of indirect neutral exciton states are visible. At the higher excitation energies the

polaron bands are visible. In figure6.2b shows the summed ground state PL for the excitation range of the excited state spectra. Analyzing the transitions between which charge state is most intense allows to plot their charge stability region. When looking at the different charge states they are more visible at specific biases. These biases are where a QDM is in its charge stability plateau and will be at its lowest energy in a particular charge state. An example of these charge stability regions is clearly shown below figure 6.2b.

Experimentally analyzing these charge stability plateaus at different excitation energies can provide information regarding the dynamics between the charge states, where they are most stable, and how that is dependent on where we optically excite. It is important to note that the transition of these charge stability regions shifts slightly for excited states due to an additional electron and hole pair that shifts the charging transitions. Figure 6.2c shows the experimentally collected excited state spectra for the negative trion, X^- is plotted this time for a much larger range. Examining the plots of the charge stability regions for the X^- and X^0 for different summed excitation energy ranges are plotted. The PL is then summed over three different energy ranges. In the first range, which is for the entire excitation energies (figure 6.2d), the negative trion and neutral exciton transition occurs at a large bias. Then the range is excited into is a smaller range of the excitations (figure 6.1e). Here we notice that the stability of the negative trion begins to diminish and the transition point between the two charge states shifts to lower biases. Finally, we show an excitation region that is only in the discrete excited states (figure 6.2f). It is apparent that due to the small range we pick up specific resonances where the laser is exciting into specific charge states. In addition to these resonances a shift is also seen in the transition of the charge states stabilities. This suggests a few processes that could be happening. Depending on the region being summed we can compare the charge stabilities for exciting into a continuum of states or into only discrete states.

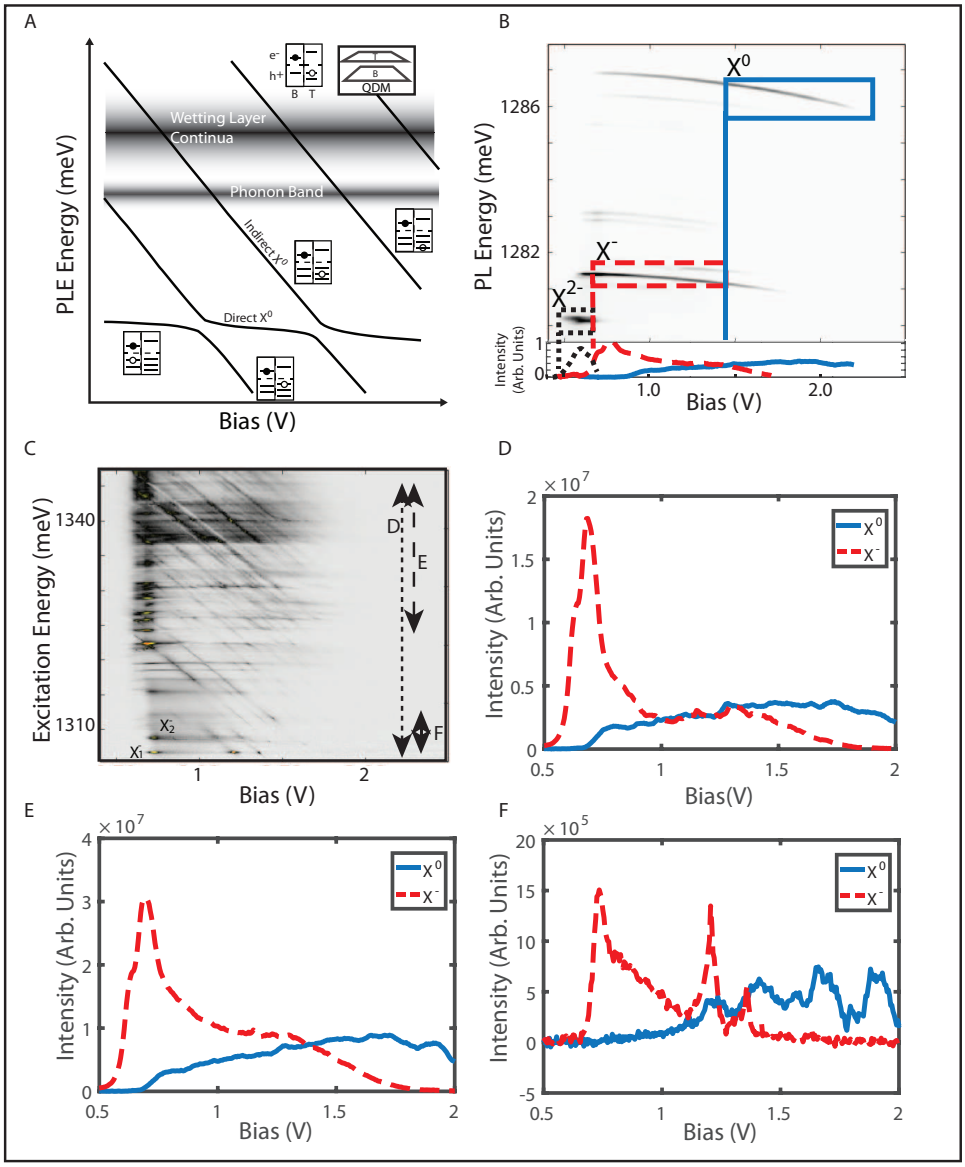

Figure 6.2: a) Schematic of simplified excited state spectra for the neutral exciton b) Summed PL of a QDM with the charge stability plateaus for each charge state boxed. c) Experimentally gathered excited state spectra for the negative trion. d) Summed PL for both the neutral and negative trion states for the entire range of the excited state spectra (1306.47-1342.37 meV) e) Summed PL for both the X^0 and X^- interactions for a smaller subset of the excited state spectra (1321.77-1342.37 meV), shift in stability is apparent. f) Summed PL for the X^0 and X^- states over the excited discrete states the energy range being (1306.47-1308.54 meV).

The shift in the transition leads to a few possible causes. The first can be due to the density of states available at that energy range. The summed PL for the large energy range can be looked at as exciting into a continuum; there are many more states that can be excited. This governs the dynamics of the charge carriers, whether it is due to a two photon absorption process and escape of a hole or just the tunneling of an extra electron into the QDM that provides the negative trion with a larger stability plateau. These situations would increase the possibility of generating more negative trions. But as the summed energy range is decreased toward the discrete case then the charge stability region decreases. In the example shown in figure 6.2d, where the excitation is purely in the discrete case, interesting resonances arise into the charged state where a strong signal in the negative trions PL is not expected. These enhancements are optical charging into the negative trion.

6.4 Experimental Results

We have witnessed such discrete enhancements of the negative trion PL outside the singly negative stability region in a few QDMs. These enhancements are indicative of an optical charging process. Figure 6.3 shows one QDM where optical charging is populating the ground state of the negative trion. The figure shows the excited state spectra for two different charge states. The states are denoted in the notation of $X^{chargestate}_{energylevel}$ where the charge states are either the neutral exciton or negative trion denoted by a '0' or '-', and the energy level where '0' specifies the ground state and larger natural numbers specify the corresponding excited state. If the specified state is an indirect state then it is labeled similarly by $iX^{chargestate}_{energylevel}$. In the PL the two charge states of interest are the neutral exciton X^0 and negative trion X^-. A charge selective PLE for both charge states is generated. The first two excited states of the neutral exciton ($|X^0_1>$ and $|X^0_2>$) spectra are visible, and corresponding anti-crossings with the indirect neutral exciton states ($|iX^0_0>$ and $|X^0_1>$). Within the same excitation energy range the excited state spectra of the negative trion's also has excited states ($|X^-_1>$ and $|X^-_2>$) that are also visible. An interesting feature appears at the resonances between the neutral exciton's indirect and negative

trions excited states. At their intersection a strong increase of the X^- ground state PL is witnessed. This charging must be due to a tunneling process that is feeding the population of the negative trion. There is indeed a large enhancement in the negative trion's ground state emission where typically no signal is expected. Making it particularly interesting due to the signal being at higher biases out of the negative trion's typical charge stability region.

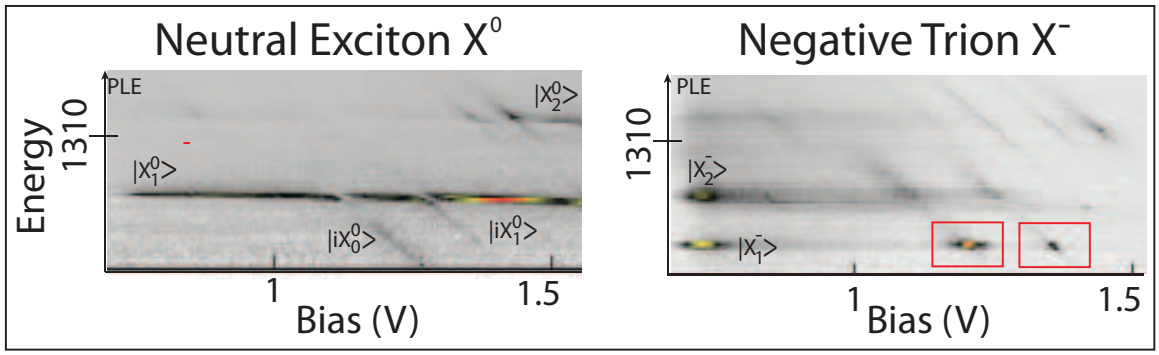

Figure 6.3: Close up of region of interest in the photoluminescence excitation (PLE) for the neutral exciton and negative trion charge states. The spectra reveals an anti-correlated behavior between the neutral exciton and negative trion charge states. At the resonance point for both transitions a charging into the negative trion's ground state is seen.

The enhancement into the negative trion occurs at the first few resonances between the excited discrete states of the QDM's neutral exciton and excited negative trion as seen in figure 6.4. Note that this occurs outside the regular bias region where the negative trion is typically stable defined in figure 6.1.

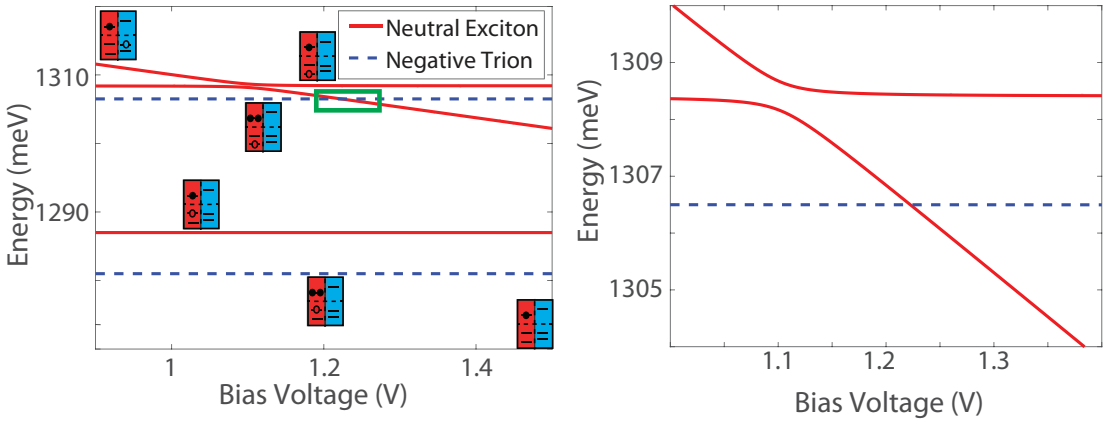

Figure 6.4: a) Calculated spectrum for ground state and first excited state of the QDM. Boxed region of the indirect excitons intersection with the excited negative trion shows where the charging occurs. b) PLE map across the neutral exciton's 1st and 2nd excited state. c) PLE map across the negative trion's 1st and 2nd excited state. Optical charging occurs at the location that the neutral exciton and negative trion intersect. d) A normalized difference map or polarization mapping that clearly shows the charging of the negative trion.

6.5 Mathematical Model

To better understand the optical charging in this discrete state region of the PLE, it is important to analyze the states that are interacting and all the different paths that the electrons and holes can take. Figure 6.5 depicts the various charge states that are in play and the different possible radiative and non-radiative process that govern the behavior of our system. We start with assuming that the system has no charges within it and starts with the crystal ground state. With the absorption of a photon at the energy of the indirect neutral exciton the process is denoted as (a). Once in the indirect neutral exciton state non-radiative relaxation occurs, for InAs/GaAs QDMs this process is on the order of 40 ns or in terms of rates 0.025 MHz. [102] [103] The excited states and the non-radiative relaxation is much shorter than the radiative lifetime leading to very low quantum efficiency of the excited states emitting, and thus we neglect emission from the excited states in this model. From the indirect exciton therefore we have two options either a non-radiative process (c)

to the ground state neutral exciton then we have radiative recombination (e) to the crystal ground state.

On the second side of the process tree a photon can be absorbed from the single electron state as process (b) into the excited negative trion. Here once again the non-radiative relaxation dominates to the ground state negative trion. The non-radiative relaxation of the negative trion to the groundstates is on the order of 40 ps or 25 MHz. The emission collected is from the electron hole recombining in process (e) leaving the single electron state. The final process that is leads to the formation of the negative trion is based on a tunneling process whereby the hole tunnels out of the QDM. This process (h) has a hole tunnel out. This leaves the QDM with a single electron. It is this process that feeds the PL enhancement of the negative trion.

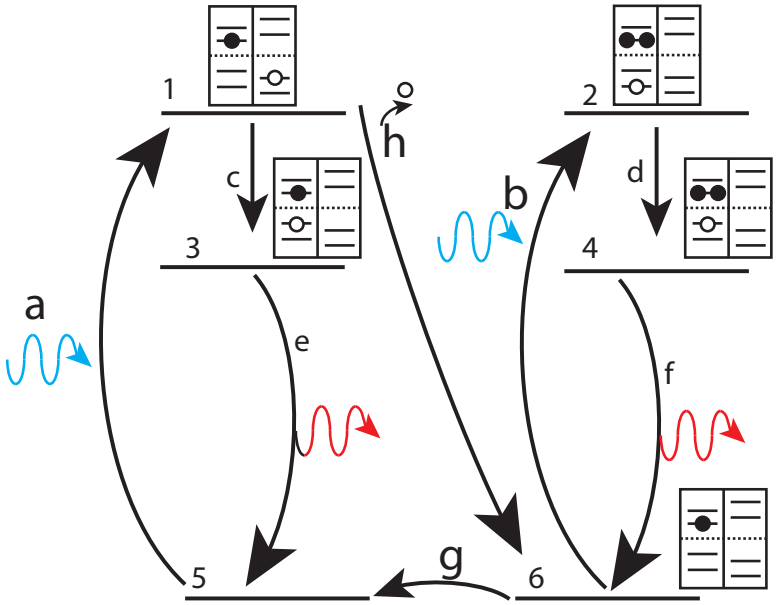

Figure 6.5: Schematic of the different charge states and possible transitions occurring between the neutral exciton and negative trion at the optical charging point of their resonance.

Now with the depiction of the various states and processes that can occur within our system we can begin to write the mathematical rate equation. The coupled differential equation is specified below with N_x where x can be 1 thru 6 representing the population of the given state. And the subscript corresponds to the rate of the

process feeding the states.

$$\frac{dN_1}{dt} = -(c+h)N_1 + aN_5 \tag{6.2}$$

$$\frac{dN_2}{dt} = -dN_2 + bN_6 \tag{6.3}$$

$$\frac{dN_3}{dt} = cN_1 - eN_3 \tag{6.4}$$

$$\frac{dN_4}{dt} = dN_2 - fN_4 \tag{6.5}$$

$$\frac{dN_5}{dt} = eN_3 - aN_5 + gN_6 \tag{6.6}$$

$$\frac{dN_6}{dt} = hN_1 + fN_4 - (b+g)N_6 \tag{6.7}$$

As mentioned processes (a) and (b) are control parameters of our model, for the resonant situations the optical driving rates into both these transitions is equal. The magnitude of the driving field is represented and controlled by the excitation power. In the model calculation the driving rate of (b) varies. The other processes (c), (e), (d), and (f) are set to their corresponding rates of 0.025 MHz, 25 MHz, 1000 MHz, and 1000 MHz respectively. These rates are due to the lifetimes of the non-radiative relaxation set to 10 picoseconds and the emission lifetime typically on the order of a nanosecond is set to 1 nanosecond for the extent of the modeling. [102] [103] This leaves the process (g) of the tunneling of an electron out of the QDM and (h) where a hole can tunnel out from the indirect exciton state. With all the lifetimes either known or controlled except for both (g) and (h) we can solve the system of differential equations finding the values that match up with our experimental data by varying the optical driving into the excited negative trion state.

For the model the initial populations of the states is set by the ratio of the intensities for the two states at the given bias. The experimental data allows for comparing the ratios of the steady states of all the different conditions when driving into both states. Experimentally the two steady state populations we collect are for the neutral exciton's and negative trion's ground state. Plotted is the ratio $\frac{X_0^-}{X_0^0}$. Solving for this ratio shows that for varying optical driving rates and electron tunneling rates we

have a parameter space where it is likely to see charging into the negative trion. The small wave function overlap of the indirect exciton leads to (a) being a slow rate so reducing the power moderately does not change the process. But changing the power moderately may change process (b) due to its direct nature and being a fast process. The competition between the two process (b) and (g) determine if the negative trion is formed or not. By changing the power appropriately may switch the negative trion on and off. Running the model for varying rates of (b) and electron tunneling rates (g) we see the regions where the negative trion is charged.

Figure 6.6 shows that the model for certain electron tunneling rates and optical driving rates can charge the negative trion. Using the ratio of the negative trion and neutral exciton allows for direct comparison with experimental results. To experimentally verify this we further investigate power series and look at the rates effect of the also the charge stability plateaus.

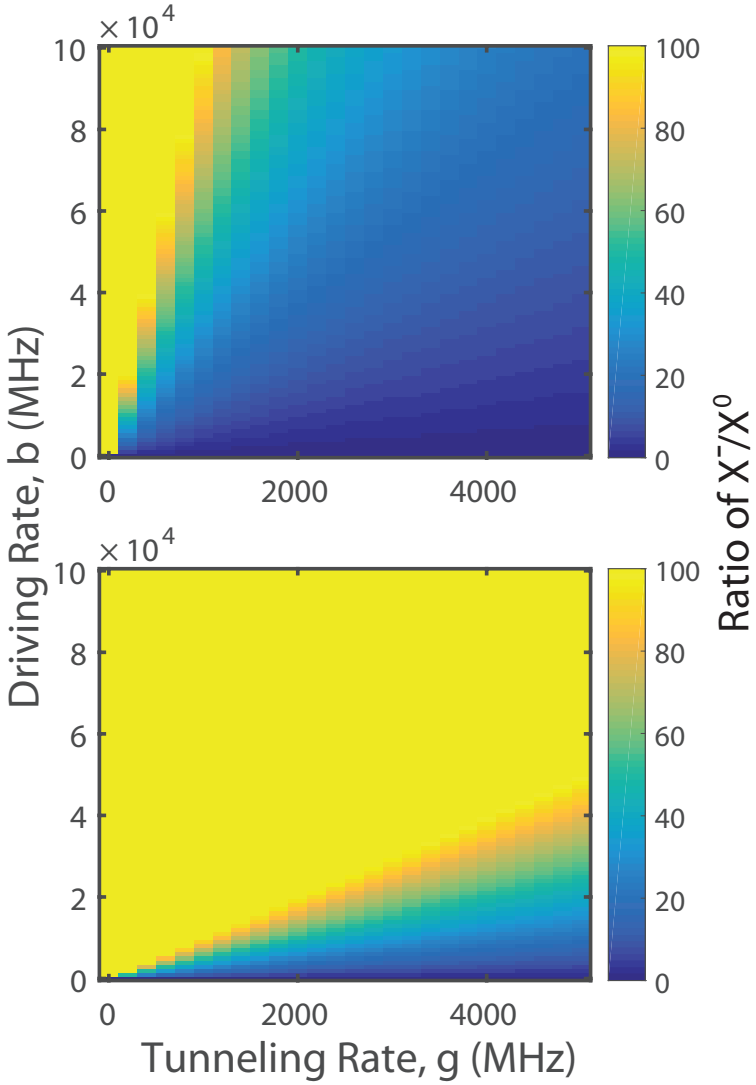

Figure 6.6: Model calculation of the intensity ratio X^-/X^0 for varying competing rates of the optical driving into the negative trion and the electron escape rate. This governs the likelihood of the single electron in the QDM being excited into the negative trion. A) Is plotted with a slow hole escape rate of 250 MHz, the ratio of the $\frac{X^-}{X^0}$ is plotted as a function of driving rate (b) and electron tunneling rate (g). B)Is plotted with a faster hole escape rate of 2500 MHz, the ratio of the $\frac{X^-}{X^0}$ is plotted as a function of driving rate (b) and electron tunneling rate (g).

6.6 Excitation Power

To understand these resonances it is important to look at the power dependence for the different states. Not only is it crucial to the understanding of the onset of the charge states, but also understanding their metastable regions. The experimental data shows that the charge stability between the two charge states can change with excitation power. The charge stability regions in figure 6.7 for the same QDM shows both low power and high power plots for the excitation energies for the discrete excited states. For only the high power excitation condition are the strong resonances noticeable in the negative trion. In the low power regime the negative trion's stability region is only at very low biases and the neutral exciton dominates everywhere else. Comparison between the two charge states show that in the low power's stability the intensity of the neutral exciton is more intense and metastable throughout the bias range and is more likely to dominate the emission spectra.

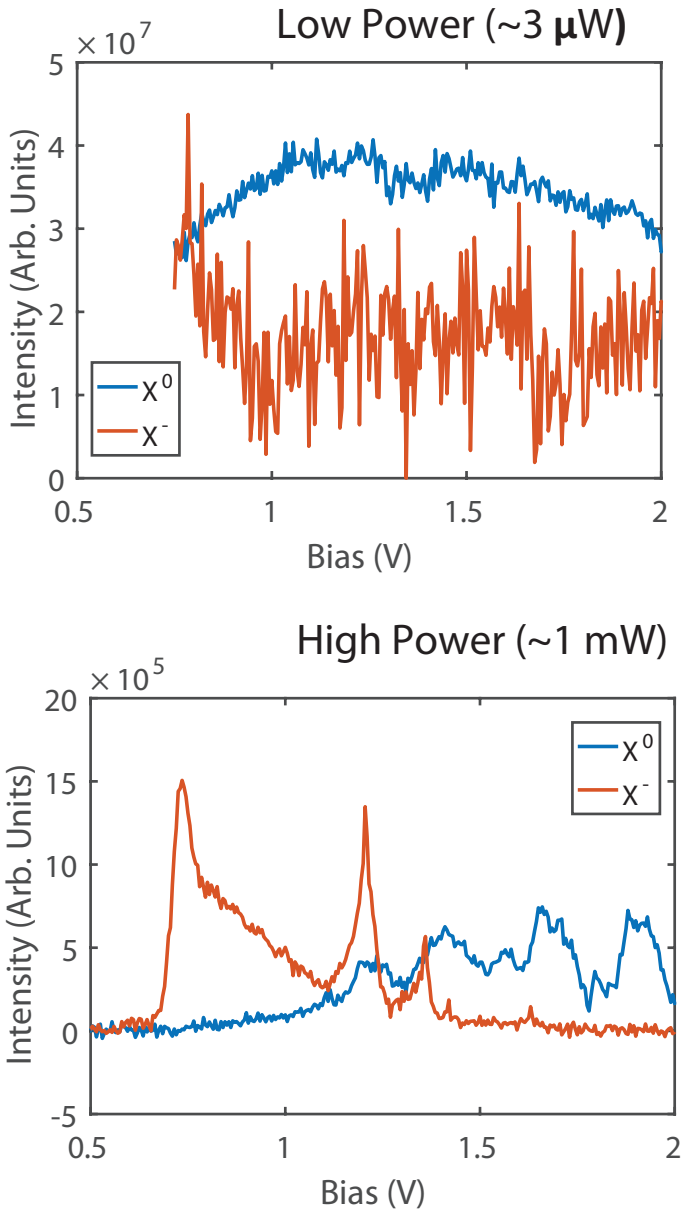

Figure 6.7: Excitation in the QDM's discrete state range for two excitation powers the first at low power and the second at the higher power. The strong resonance signals are only visible at the high power.

The ground state's charge stability has large regions where the two charge states overlap and make the existence of both states more probable. Interestingly, the excited state spectra shows a different story for the excited states. These regions

have slightly altered charge stabilities due to the additional separation of the holes excited energy levels. In the excited state spectra, figure 6.5, the charge stability plateau for the negative trion appear to be much smaller and a metastable region does not exist. The excited state charge plateaus agree with the calculated charge plateaus.

From the experimentally collected data it appears that two conditions are responsible for the optical charging into the negative trion charge state. The first is the large metastable charge ground states and the second is large powers. This leads to the hypothesis that this charging is due to a tunneling process of an extra electron coming into the QDM with large powers the optical driving is more likely to populate the excited negative ground states thus optically charging into the negative trion. The mechanism behind this occurring at the larger powers is two competing rates: the tunneling of an electron out of the QDM and the rate of exciting into the negative trion.

At high powers, when we start with an empty QDM in the charge stability plateau of the neutral exciton, this leads to the absorption of photons into the excited neutral exciton state. If the excited neutral exciton is in resonance with a negative trion state at high powers then there is a likelihood of getting an electron into the QDM. If the optical field driving rate is faster than the electron escape rate due to it being in the neutral exciton's stability plateau, this can lead to optically charging the negative trion.

Comparison of low and high power excitation of the QDMs shows that the optical charging process is non-existent when the negative trion and neutral exciton do not have overlapping metastable states. Similarly, even when metastable states exist, the optical charging occurs only at high powers. At the low powers the excess electron is more likely to tunnel out of the QDM (portrayed in figure 6.7). In this figure we see the optical charging is clearly visible for the metastable state QDM. But at low powers and for another QDM that lacks the metastable states, no optical charging is witnessed. This leads to the conclusion that the two factors that control the optical charging of the negative trion are: the rate of the hole escaping and leaving a single electron in the QDM, and a driving rate that is is fast enough such that the negative

trion is generated over that of the neutral exciton when the two are at resonance. Large excitation powers leads to a much larger rate of exciting into the negative trion than the neutral exciton when the competing hole escape and electron tunneling rates are favorable.

6.7 Conclusion

In this chapter we demonstrate the ability to optically charge QDMs. At certain resonances of the excited states, optical charging occurs into specific charge configurations. The excitation energies at the resonance point of an indirect neutral exciton and a direct excited negative trion state lead to charging of the ground state negative trion. This optical charging process has been described by a mathematical rate equation model, where the two competing processes are that of the electron leaving the QDM and the driving rate into the excited negative trion. If the driving rate is fast enough this leads to generation of the negative trion and is seen as an enhancement in the PL, whereas at low powers the neutral exciton dominates.

The future direction of this research will be to conduct more thorough power dependence measurements to be able to resolve the rates for both branches of the processes, both the indirect exciton and the negative trion. By resolving the rates for these individual optical cycles experimentally the next step would be to consolidate with the model and calculate both tunneling rates for both (g) and (h). Additionally, we aim to fully model the charging process for a larger parameter space of different driving fields and tunneling rates. The goal being to align and garner a full understanding of the PL enhancement into the negative trion. It would also be beneficial to experimentally acquire time-resolved spectroscopy that can give additional information regarding the process and lifetimes for each of the individual states. This research has the potential to lead to new nanostructure designs where controlled optical charging can be governed by excitation power. This could also lead to structures that could be engineered such that at specified resonances specific charge states could be generated.

Optical charging in semiconductor nanostructures offers these systems many advantages. Optically charging is wireless, ultrafast, and allows for the fast manipulation of quantum states. Systems such as quantum dots (QDs), have been shown to hold enormous potential for shaping novel quantum technologies. [104] The ability to work with fundamental excitation in QDs paired with recent developments in controlled coupling between two QDs make highly intriguing prospects of building quantum networks for information processing. [105] Optical charging can bring us a step closer to the realization of quantum information and communication by allowing for a quick way to prepare initial quantum charge state.

Chapter 7

Conclusion

Quantum dots and quantum dot molecules hold great potential for furthering modern technologies. With the recent trend toward quantum enhanced technologies, QDs are becoming more incorporated in consumer electronics. QDs and QDMs have found a place in different technology sectors from photovoltaics to bioimagery; enhancing current methods. They also hold promise for many new emerging devices like quantum enhanced sensors that are near fruition. QDMs hold great potential for quantum information and new extremely sensitive detectors by exploiting the quantum properties such as coherence and entanglement. To fully exploit the potential of these nanostructures a complete understanding of the physics is needed. Garnering a full understanding would allow us to incorporate these findings and lead the way to major technological breakthroughs. This dissertation presents a new measurement method that allows for high spectral resolution spectra, continues research into understanding interaction between different resonant states, and presents a new optical charging phenomena that is experimentally witnessed in these systems. This research will take QDMs a step closer to fully understanding how these systems work and takes them a step closer to utilization in modern quantum enhanced technologies.

To date, single QDs or coupled QDs such as QDMs, have led to a new realization of solid state devices [106] such as single-photon sources, [107] optically controlled electron spin memory devices [108] and an all optical quantum gate [109]. For quantum computing, a bit can be any state of a qubit, and these qubits can be realized

using a two-level system such that can be defined in a QDM. For quantum computing to become a reality, it is necessary to employ quantum gate operations, which are reliant on coherently interacting qubits. [105] The purpose of these quantum gates is to control the quantum states of the system and providing the opportunity to manipulate them. This realization is necessary for quantum algorithms, which will outperform classical algorithms. [110] Current challenges for quantum computing are scaling qubit processors to more than a dozen qubits, high fidelity for a universal set of quit transformation and long-living qubits for memory and communications and then to accomplish all three of these challenges without low temperatures to make it cost effective. Therefore, to further progress the fields of solid-state based quantum computation and quantum cryptography, more innovation is necessary to upscale the number of coherently interacting QDs.

Other applications that QDs are mode-locked lasers to generate optical pulse trains as pulse sources for a variety of features [111]. They have been also used for semiconductor optical amplifiers, where research toward future large optical networks has fueled the research [112]. In the single dot realm they have seen major steps toward the realization of single-photon sources. [113, 114] They have also lead to their potential use as a source for entangled photon pairs that would have plenty of application in the fields of quantum information. [115, 116]

The research into expanding these systems of QDs is also motivated by the search for new metamaterials, artificial materials engineered to have properties that are not found in nature. The ability to form a large array of coupled QDs would lead to a number of novel material properties, enabling basic research into cooperative many-body systems and opening the door toward the further development of programmable matter. This new matter could be controlled via fields and light-matter interactions, allowing for the further study of phenomena such as superfluidity, sub- and superradiance. It could open the door to new devices such as superradiant lasers, tunable single photon emitters, and other materials that are tunable for any desired number of tasks [117].

The dissertation's two major focuses are studying and finding functionalization of resonant interactions between different states, and examining phonon interactions

with the electronic states of a QDM.

The first section of the research focuses on a phonon-assisted quasi-resonant fluorescence spectroscopy method that was developed in our lab. The approach leads to high spectral resolutions of up to 1 μeV all with a very common single spectrometer experimental setup. The method is a combination of laser and photoluminescence spectroscopy. With the excitation laser set to resonantly excite through a transition and the PL is monitored an optical phonon energy below the excitation. The resolution of the system is laser linewidth limited, as a signal is only resolved as the laser is scanned resonantly across a transition. This experimental method future will assist research in other nanostructures and will be used to study, other quantum dot or quantum dot molecule structures, nitrogen vacancy sites in diamond, defects in silicon carbide and other zero-dimensional nanostructures. This method has the potential to greatly assist current research methods due to the methods easy incorporation into commonplace optical spectroscopy set-ups.

The second major discussion of the dissertation is the ability to coherently couple electronic states with optical phonons. This is clearly seen in the formation of the molecular polaron state and experimentally portrayed when discrete indirect excitons are in resonance with the LO phonon bands; here we get Fano resonances that occur. The absorption line shapes are governed by the value of the q_{fano} parameter and are easily controlled via the electronic and optical means in our QDMs, such as power and excitation. These molecular polarons give us nice features of being able to cloak the indirect discrete states along with the ability to amplify very weak coupling channels. This result has great potential for future research. Potential future direction can be to investigate if similar molecular polaron formation occurs for electron tunneling samples. All research presented in this dissertation dealt with hole tunneling between the QDs, with electrons the mobility increases with their smaller mass and makes resolving this a greater challenge. Taking this a step further would be to look at the time dynamics of the molecular polaron formation. Resolving the time constants of the molecular polaron would lead to a deeper understanding of the mechanism behind the formation of the molecular polaron and the time constants relationship to the Fano parameter (q_{fano}). To provide this time constant information, ultra-fast

laser spectroscopy is needed to measure these values.

The last focus of the dissertation in on optical charging that occurs at resonances between charged excited states, such as the negative trion and the excited neutral exciton. At the resonances of the two excited states a specific charging of the ground state occurs. A mathematical model is used to model and understand the charging process, we tie the process to the charge stability regions for the different charge states and their impact on the tunneling of charge carriers into and out of the QDMs. Future direction for this research would be to first investigate further resonant interactions for other charge states (i.e. positive trion, biexciton and neutral exciton), to further characterize the optical charging that occurs. Future experiments employing ultra-fast optical spectroscopy would allow to extract the charge states time constants and allow to compare with the rates used in our mathematical model. This would allow to further understand this charging process and would allow to also devise laser pulse techniques that could optically initialize optical charging into desired QD charge states.

In conclusion, the research covered in this dissertation pushes toward the goal of new and expanding quantum enhanced technologies. From developing a new optical measurement method to study zero-dimensional nanostructures with extremely high spectral resolutions. Along with the formation of the molecular polaron and using phonons coherently being a large step for the new field of phononics. And finally optical charging that gives the ability to switch between change states in a selective fashion and find application in quantum information technologies and quantum cryptography.

Appendix A

Phonon-Assisted Quasi-Resonant Fluorescence Protocol

Note: The methodology described is specific to a particular software, although other software packages may be used instead.

1) Sample preparation and cool down

1.1) Fabricate the sample.

1.1.1) Grow the sample, using the Stranski-Krastanov growth method via molecular beam epitaxy creating two vertically-stacked self-assembled InAs/GaAs QDs that are separated by a 4nm tunnel barrier as previously described. [118] Embed the QDs in an electric field effect structure (i.e. Schottky diode) allowing for an electric field to be applied to the QDMs. [52] Note: The use of QDMs is not a requirement for the method. Also, the semiconductors InAs/GaAs are not necessary, the technique will work for QDMs or QDs made from any semiconductor combination.

1.1.2) Fabricate the samples so that individual QDs can be optically addressed. Do this by either adding an aperture mask to the top of the sample or making a low density sample with 108 QDs/cm2 or less depending on the focal spot size.18

1.2) Mount the sample into the chip header.

1.2.1) Apply an alloy consisting of 50 Bismuth, 26.7 Lead, 13.3 Tin, and 10 Cadmium on the ceramic chip header. Heat the chip using a hot plate until the alloy liquefies. Place the bottom of the sample onto the liquefied alloy attaching it to the

chip header. Note: The bottom of the sample is one of the electrodes of the Schottky diode and the solder point to the chip header is connected to a pin. Another alternate for attaching the sample is conductive silver epoxy.

1.3) Adhere 40 gauge gold wire from a point (top corner) of the sample to a pin on the chip.

1.3.1) Place a droplet of silver epoxy on the top corner of the sample and one droplet on one of the pin pads on the chip.

1.3.2) Carefully lay the gold wire in the two droplets. Note: The top of the sample is the other electrode of the Schottky diode that allows for application of an electric field.

1.4) Mount the chip and sample into the cryostat and ensure the sample has good thermal contact with the copper sample holder.

1.4.1) Apply indium foil between the chip and the cryostats cold finger.

1.4.2) Pressure mount the chip to the cold finger. Use two screws with washers and tighten firmly to ensure good thermal contact with the cryostats copper cold finger.

1.5) Attach wires from the chip pins that are connected to both the top and bottom electrodes on the sample. Run these wires through the cryostat to the source meter. Note: The source meter applies a bias to the samples electrodes, exposing the QDs to an external electric field.

1.6) Evacuate and bring the cryostat and sample chamber to vacuum. Start the turbo pump, evacuating to about 10-6 torr in preparation for the cool down of the sample. Note: Cooling and temperature control for the experiment is accomplished with the cryostat which is composed of a closed cycle refrigerator and an attached microscopy sample chamber.

1.7) Start the cryostats compressor. Allow the cryostat to cool the system until reaching the desired temperature. Note: For the presented results the temperature was approximately 18K. Once the sample is cooled, the setup is ready for the installation of the optics that will allow for the optical measurement to be taken.

2) Optics setup Note: For all set up procedures, run the laser, source meter, spectrometer and CCD by either using the software provided by the manufacturer or

other custom program.

2.1) For PL collection, place a long working distance 50X microscope objective and collimation lens in line with the lens that focuses the PL signal onto the spectrometer. Collect the spectrum through a 0.75m monochromator where the signal is dispersed by an 1100 mm-1 grating and detected using a liquid nitrogen cooled 1340x100 pixel CCD camera.

2.2) Using a white light source, illuminate the sample.

2.2.1) Focus the image of the sample through an external camera and the spectrometer by properly aligning the all optics on the detection side (i.e. collimation and focusing lens) and at zero wavelength get a clean focused image of the sample on the spectrometer CCD. Note: It is helpful to have another external imaging camera to help with alignment and getting a crisp image of the sample.

2.3) After the detection side is set up, focus the laser onto the sample. Focus the beam spot to the smallest size possible on the sample by using a lens. Use a tunable diode laser with an excitation range that contains the ground state transition energies. Set the laser incident to the sample at an oblique angle. An advantage of oblique incidence is that it helps get rid of a large portion of the scattered laser light.

2.4) Excite the sample at a higher non-resonant energy. Optimally, do this by exciting at an energy below the wetting layer. For the InAs/GaAs QDMs in this study this corresponds to 75 meV or more above the ground state transitions.

2.5) Run the spectrum acquisition software in focus mode. Scan the sample across the laser spot using an X-Y translation stage which is attached to the cryostat microscopy sample housing. Do this until the spectrometer CCD captures the discrete lines of the ground-state transitions. Center the detection on one of the QDMs. Note: Once a QDM is found, the optical setup is completed. For the samples used the ground state energies are around 1300 meV.

2.6) Generate a bias map.

2.6.1) Apply a potential via the source meter (step 1.5) connected to the electrodes on the sample; this applies a bias across the electrodes in turn generating an electric field to the QDMs. Note: The bias range applied to the sample is 0-2V across the Schottky diode structure. This is when the device is in reverse bias, and the electric

field limits the amount of charges in the QDM allowing for the individual charge states to be visible.

2.6.2) Take individual spectra at different incremented voltage values, depending on desired resolution this normally ranges from hundredths to thousandths of a volt. Combine these individual spectra together by using a custom program (e.g. LabView). Note: The program can be easily coded using a wide range of different programs to combine the vector columns of the individual spectra into a matrix, in the presented experiment this has been added in to stitch together the data in real-time.

2.6.2.1) Click the run button to take a bias map. This takes spectra at a set bias and make it a column vector, then adds each incremented bias spectra as another column. Note: This generates a data matrix where the intensity values correspond to the PL intensity, rows represents energy/wavelength, and columns correspond to voltage. The bias map should be viewable as it is being run, thus allowing live feedback on the quality of the data. Note: A bias map helps to identify different charge configurations and gives the proper information to complete the setup of both the excitation and detection paths.

2.7) Identify the transition that will be excited. Note the energy of the transition and the bias range of interest.

2.7.1) At this point decide how the laser excitation will be tuned through the transition. There are three different options to get the laser to excite into the ground state transition:

2.7.1.1) Tune the transition energy by temperature.18

2.7.1.2) Use the Stark shift of the transition to achieve resonance with the laser energy.19 Note: A nice feature of the two methods mentioned above is that a tunable laser source is not needed, since the QDM transitions are tuned through a fixed laser energy.

2.7.1.3) Alternatively, use a tunable laser source, stepping the laser energies through the transition. A detection signal will be present when the laser is resonant with the transition, this gives the measurement its laser limited spectral resolution. This will be the focus for the rest of the protocol.

2.8) With the transition identified and the experimental parameters set, select

both excitation and detection energies for the measurement.

2.8.1) Choose the excitation energy as that of the transition. Choose the detection as the excited transitions energy minus the energy of the longitudinal optical (LO) phonon associated with the semiconductor alloy. Using these values, choose the proper edge pass filters for the measurement; they must have cutoffs in between the excitation and detection energies. Note: For the experimental results presented, the driven transition was the neutral ground state exciton shown in Fig.3, observed at 1301.7 meV and the -1 LO phonon emission is located at 1266 meV, corresponding to 952.5nm and 979.3 nm, respectively. We therefore use a 960 nm short pass filter for the excitation and a 960 nm long pass filter for the detection. Interference cut-off filters are ideal for this purpose since they can be tuned by adjusting the angle.

2.9) Set the laser to excite at the transition energy of interest, which is done simply by entering the desired laser wavelength value in the appropriate input field on the front panel of the laser control software.

2.10) Set the center wavelength to the predetermined value to monitor the -1LO photon emission by entering the desired center wavelength value in the appropriate input field on the front panel of the spectrometer control software. Note: The -1 LO photon emission for InAs/GaAs is approximately 36 meV below the exciton transition that will be excited.

2.11) Using the camera software, start collection with the CCD by running the spectrum acquisition software in continuous mode by clicking the focus mode button. A signal should be visible or could still be hidden by the laser scatter.

2.12) Maximize the signal. CRITICAL STEP: Tune the excitation short pass filter, by slightly adjusting its angle so that it has the proper wavelength cutoff. Note: The optimal angle is established by monitoring the signal while adjusting the angle of the short pass filter. By changing the angle of the filter this changes the cut-off wavelength. The key is to make sure that as much laser light as possible is suppressed from the collection.

3) Set up the quasi-resonance measurement.

3.1) Enter the following values into the custom software (e.g. LabView) that runs the experimental equipment and data collection for the experiment.

3.1.1) Enter the laser energy into the software to excite roughly 50 eV above the transition energy.

3.1.2) Set the range that the tunable laser diode will scan. The key is to have the laser step through the transition, covering a 50 eV range above and below the transition should be sufficient. The detection PL will only be visible when the laser excitation is resonant with the transition.

3.1.3) Select a reasonable integration time for the CCD. Experiment with the integration time to get a good signal. The larger the integration time the better signal averaging that is obtainable.20 Note: Integration times used for the experiment were 10 seconds. But, integration times can be as low as 0.5 seconds, depending on the strength of the PL signal. At times it is not even necessary to see the signal in individual scans but upon stitching the spectra together the data summation plus the capability of the eye to interpolate will reveal the transitions in the photoluminescence excitation (PLE) map.

4) Data Acquisition

4.1) Set experimental parameters on the computer controls using the custom softwares main screen. To do so, start the collection program and click on the Step Polarization, Temp, or WL tab. This sets all the experimental values and once run, collects data through the various parameters. Note: For our experiments data taking all computer controls were custom programmed. The key is to have a software or program able to set the center wavelength of the spectrometer, control the CCD and source meter, and step the laser energy through the transition while collecting a range of spectra at different biases.

4.1.1) Input the established laser energy range that the laser will scan through: from about 50 eV above the neutral exciton transition energy of 1301.7 meV, to 50 eV below. Set the initial Wavelength to start the scan using the Desired WL (nm) field. Set the end range of the laser to scan over (End Motor Unit).

4.1.2) Set the bias range that the source meter will scan through by clicking on the Voltage Settings tab. Set the starting bias value (Voltage Start (V)), the end bias value Voltage End (V) and the bias step size Voltage Step (V). Here, the bias range scanned was 1.68 to 1.82V.

4.1.3) Input the integration time chosen by clicking on the Camera Settings tab. Set the integration time for the CCD under Exposure (s) (Refer to step 3.3).

4.2) Once the experimental parameters are established begin the experiment. Start collection by clicking the run button Note: At each laser energy the software varies the bias taking a spectrum and a background spectrum. This is done for each bias step. Then the laser energy is varied and the process continues until the entire range chosen is complete.

4.3) Post-process the data.

4.3.1) Take the additional background scans that are taken at the end of every bias map and subtract the average from each of the bias columns. Use a background subtraction program, or write a program that takes the background columns, averages them together and subtract this averaged background spectra from each bias column in the data matrix. Note: This removes other spurious signals caused by any remaining scattered laser light, greatly improving the bias map.

4.4) Analyze the data.

4.4.1) For example, to extract the characteristic parameters of the spectral line use a mathematical fitting software to run a Lorentzian fitting at each bias slice of the PL map.21 Once the fitting procedure has been completed all information will be in the coefficients of the fitting such as the maximum intensity, spectral location and FWHM.

Appendix B

Equipment List

List of experimental equipment used for the research presented in this dissertation: Spectra Physics DL pro tunable diode laser, Cryo Industries of America Inc. closed cycle cryogen free refrigerator system for microscopy, 2611A Keithley sourcemeter, Mitutoyo America Corporation 50x Mitutoyo Plan Apo NIR infinity-corrected objective, Pfeiffer Vacuum turbo pump, NIR coated mirrors, Thorlabs polarizers, various Thorlabs AR coated achromatic lens, various Thorlabs long pass filter, various Thorlabs short pass filters, Meadowlark Optics liquid crystal variable retarder, Princeton Instruments Trivista 0.75m triple spectrometer, Princeton Instruments liquid nitrogen cooled camera, Watec external camera,Lake Shore Cryotronics Ostoalloy, Surepure Chemetals Gold wire (40 gauge), A.I. Technology silver epoxy, National Instruments program software, Bristol Instruments 671 series wavelength meter, Thorlabs Inc. motorized filter wheel, assorted Thorlabs neutral density filters, Thorlabs power meter.

Bibliography

[1] Gordon E Moore. Cramming more components onto integrated circuits, reprinted from electronics, volume 38, number 8, april 19, 1965, pp. 114 ff. *IEEE Solid-State Circuits Society Newsletter*, 20(3):33–35, 2006.

[2] N Hinkley, JA Sherman, NB Phillips, M Schioppo, ND Lemke, K Beloy, M Pizzocaro, CW Oates, and AD Ludlow. An atomic clock with 10–18 instability. *Science*, 341(6151):1215–1218, 2013.

[3] Xiao-Song Ma, Thomas Herbst, Thomas Scheidl, Daqing Wang, Sebastian Kropatschek, William Naylor, Bernhard Wittmann, Alexandra Mech, Johannes Kofler, Elena Anisimova, et al. Quantum teleportation over 143 kilometres using active feed-forward. *Nature*, 489(7415):269–273, 2012.

[4] Trevor Lanting, AJ Przybysz, A Yu Smirnov, Federico M Spedalieri, Mohammad H Amin, Andrew J Berkley, R Harris, Fabio Altomare, Sergio Boixo, Paul Bunyk, et al. Entanglement in a quantum annealing processor. *Physical Review X*, 4(2):021041, 2014.

[5] Takafumi Ono, Ryo Okamoto, and Shigeki Takeuchi. An entanglement-enhanced microscope. *Nature communications*, 4:2426, 2013.

[6] Michael A Nielsen and Isaac L Chuang. *Quantum Computation and Quantum Information (Cambridge Series on Information and the Natural Sciences)*. Cambridge University Press, 2004.

[7] Artur K Ekert. Quantum cryptography based on bells theorem. *Physical review letters*, 67(6):661, 1991.

[8] Louis E Brus. Electron–electron and electron-hole interactions in small semiconductor crystallites: The size dependence of the lowest excited electronic state. *The Journal of chemical physics*, 80(9):4403–4409, 1984.

[9] J-Y Marzin and G Bastard. Calculation of the energy levels in inasgaas quantum dots. *Solid state communications*, 92(5):437–442, 1994.

[10] D Gammon, ES Snow, BV Shanabrook, DS Katzer, and D Park. Fine structure splitting in the optical spectra of single gaas quantum dots. *Physical review letters*, 76(16):3005, 1996.

[11] M Bayer and Alfred Forchel. Temperature dependence of the exciton homogeneous linewidth in in 0.60 ga 0.40 as/gaas self-assembled quantum dots. *Physical Review B*, 65(4):041308, 2002.

[12] PW Fry, JJ Finley, LR Wilson, A Lemaitre, DJ Mowbray, MS Skolnick, M Hopkinson, G Hill, and JC Clark. Electric-field-dependent carrier capture and escape in self-assembled inas/gaas quantum dots. *Applied Physics Letters*, 77(26):4344–4346, 2000.

[13] CA Duque, N Porras-Montenegro, Z Barticevic, M Pacheco, and LE Oliveira. Effects of applied magnetic fields and hydrostatic pressure on the optical transitions in self-assembled inas/gaas quantum dots. *Journal of Physics: Condensed Matter*, 18(6):1877, 2006.

[14] Alexander Hogele, Stefan Seidl, Martin Kroner, Khaled Karrai, Richard J Warburton, Brian D Gerardot, and Pierre M Petroff. Voltage-controlled optics of a quantum dot. *Physical review letters*, 93(21):217401, 2004.

[15] TH Stievater, Xiaoqin Li, D Gammon Steel, D Gammon, DS Katzer, D Park, C Piermarocchi, and LJ Sham. Rabi oscillations of excitons in single quantum dots. *Physical Review Letters*, 87(13):133603, 2001.

[16] Gregor Jundt, Lucio Robledo, Alexander Hogele, Stefan Falt, and Atac Imamoglu. Observation of dressed excitonic states in a single quantum dot. *Physical review letters*, 100(17):177401, 2008.

[17] Cyprian Czarnocki, Mark L Kerfoot, Joshua Casara, Andrew R Jacobs, Cameron Jennings, and Michael Scheibner. High resolution phonon-assisted quasi-resonance fluorescence spectroscopy. *JoVE (Journal of Visualized Experiments)*, 112:e53719–e53719, 2016.

[18] Charles Kittel. *Introduction to solid state*, volume 162. John Wiley & Sons, 1966.

[19] Neil W. Ashcroft and N. David Mermin. *Solid State Physics*. Thomson Learning, Inc., 1976.

[20] David L Sidebottom. *Fundamentals of Condensed Matter and Crystalline Physics: An Introduction for Students of Physics and Materials Science*. Cambridge University Press, 2012.

[21] http://www.ioffe.ru/SVA/NSM/Semicond/InAs/. Inas, 2017.

[22] http://www.ioffe.ru/SVA/NSM/Semicond/GaAs/. Gaas, 2017.

[23] Robert Eisberg and Robert Resnick. *Quantum physics*. John Wiley New York, 1974.

[24] Ramamurti Shankar. *Principles of quantum mechanics*. Springer Science & Business Media, 2012.

[25] Jun John Sakurai and Eugene D Commins. Modern quantum mechanics, revised edition, 1995.

[26] G Eber, K Von Klitzing, K Ploog, and G Weinmann. Two-dimensional magneto-quantum transport on gaas-alxga1-xas heterostructures under non-ohmic conditions. *Journal of Physics C: Solid State Physics*, 16(28):5441, 1983.

[27] Jakub Kedzierski, Jeffrey Bokor, and Erik Anderson. Novel method for silicon quantum wire transistor fabrication. *Journal of Vacuum Science & Technology B: Microelectronics and Nanometer Structures Processing, Measurement, and Phenomena*, 17(6):3244–3247, 1999.

[28] Jianfang Wang, Mark S Gudiksen, Xiangfeng Duan, Yi Cui, and Charles M Lieber. Highly polarized photoluminescence and photodetection from single indium phosphide nanowires. *Science*, 293(5534):1455–1457, 2001.

[29] RC Ashoori. Electrons in artificial atoms. *Nature*, 379:413–419, 1996.

[30] Marius Grundmann, Oliver Stier, and Dieter Bimberg. Inas/gaas pyramidal quantum dots: Strain distribution, optical phonons, and electronic structure. *Physical Review B*, 52(16):11969, 1995.

[31] Arkadiusz Wojs and Pawel Hawrylak. Charging and infrared spectroscopy of self-assembled quantum dots in a magnetic field. *Physical Review B*, 53(16):10841, 1996.

[32] Gustavo A Narvaez and Alex Zunger. Calculation of conduction-to-conduction and valence-to-valence transitions between bound states in (in, ga) as/ ga as quantum dots. *Physical Review B*, 75(8):085306, 2007.

[33] Margaret A Hines and Philippe Guyot-Sionnest. Synthesis and characterization of strongly luminescing zns-capped cdse nanocrystals. *The Journal of Physical Chemistry*, 100(2):468–471, 1996.

[34] Christopher B Murray, CR Kagan, and MG Bawendi. Synthesis and characterization of monodisperse nanocrystals and close-packed nanocrystal assemblies. *Annual Review of Materials Science*, 30(1):545–610, 2000.

[35] Nir Tessler, Vlad Medvedev, Miri Kazes, ShiHai Kan, and Uri Banin. Efficient near-infrared polymer nanocrystal light-emitting diodes. *Science*, 295(5559):1506–1508, 2002.

[36] Richard J Warburton. Self-assembled semiconductor quantum dots. *Contemporary Physics*, 43(5):351–364, 2002.

[37] Christopher B Murray, Shouheng Sun, Wolfgang Gaschler, Hugh Doyle, Theodore A Betley, and Cherie R Kagan. Colloidal synthesis of nanocrystals and nanocrystal superlattices. *IBM Journal of Research and Development*, 45(1):47–56, 2001.

[38] A Zrenner. A close look on single quantum dots. *The journal of chemical physics*, 112(18):7790–7798, 2000.

[39] Ronald Hanson, Leo P Kouwenhoven, Jason R Petta, Seigo Tarucha, and Lieven MK Vandersypen. Spins in few-electron quantum dots. *Reviews of Modern Physics*, 79(4):1217, 2007.

[40] AY Cho and JR Arthur. Molecular beam epitaxy. *Progress in solid state chemistry*, 10:157–191, 1975.

[41] PB Joyce, TJ Krzyzewski, GR Bell, TS Jones, S Malik, D Childs, and R Murray. Effect of growth rate on the size, composition, and optical properties of inas/gaas quantum dots grown by molecular-beam epitaxy. *Physical Review B*, 62(16):10891, 2000.

[42] JH Neave, BA Joyce, PJ Dobson, and N Norton. Dynamics of film growth of gaas by mbe from rheed observations. *Applied Physics A*, 31(1):1–8, 1983.

[43] Gert Schedelbeck, Werner Wegscheider, Max Bichler, and Gerhard Abstreiter. Coupled quantum dots fabricated by cleaved edge overgrowth: From artificial atoms to molecules. *Science*, 278(5344):1792–1795, 1997.

[44] DJ Eaglesham and M Cerullo. Dislocation-free stranski-krastanow growth of ge on si (100). *Physical Review Letters*, 64(16):1943, 1990.

[45] HJ Krenner, M Sabathil, EC Clark, A Kress, D Schuh, M Bichler, G Abstreiter, and JJ Finley. Direct observation of controlled coupling in an individual quantum dot molecule. *Physical review letters*, 94(5):057402, 2005.

[46] Thomas Unold, Kerstin Mueller, Christoph Lienau, Thomas Elsaesser, and Andreas D Wieck. Optical control of excitons in a pair of quantum dots coupled by the dipole-dipole interaction. *Physical review letters*, 94(13):137404, 2005.

[47] CR Kagan, CB Murray, and MG Bawendi. Long-range resonance transfer of electronic excitations in close-packed cdse quantum-dot solids. *Physical Review B*, 54(12):8633, 1996.

[48] Lijuan Wang, Armando Rastelli, Suwit Kiravittaya, Mohamed Benyoucef, and Oliver G Schmidt. Self-assembled quantum dot molecules. *Advanced Materials*, 21(25-26):2601–2618, 2009.

[49] Andreas Wensauer, Oliver Steffens, Michael Suhrke, and Ulrich Rössler. Laterally coupled few-electron quantum dots. *Physical Review B*, 62(4):2605, 2000.

[50] GJ Beirne, C Hermannstadter, L Wang, A Rastelli, OG Schmidt, and P Michler. Quantum light emission of two lateral tunnel-coupled (in, ga) as/gaas quantum dots controlled by a tunable static electric field. *Physical review letters*, 96(13):137401, 2006.

[51] Sv Fafard, ZR Wasilewski, C Ni Allen, D Picard, M Spanner, JP McCaffrey, and PG Piva. Manipulating the energy levels of semiconductor quantum dots. *Physical Review B*, 59(23):15368, 1999.

[52] Eric A Stinaff, Michael Scheibner, Allan S Bracker, Ilya V Ponomarev, Vladimir L Korenev, Morgan E Ware, Matt F Doty, Thomas L Reinecke, and Dan Gammon. Optical signatures of coupled quantum dots. *Science*, 311(5761):636–639, 2006.

[53] Authors AS Bracker, M Scheibner, MF Doty, EA Stinaff, IV Ponomarev, JC Kim, LJ Whitman, TL Reinecke, and D Gammon. Engineering electron and hole tunneling with asymmetric inas quantum dot molecules. *arXiv preprint cond-mat/0609147*, 2006.

[54] Tomonori Ishikawa, Tetsuya Nishimura, Shigeru Kohmoto, and Kiyoshi Asakawa. Site-controlled inas single quantum-dot structures on gaas surfaces patterned by in situ electron-beam lithography. *Applied Physics Letters*, 76(2):167–169, 2000.

[55] RH Blick, RJ Haug, J Weis, D Pfannkuche, K v Klitzing, and K Eberl. Single-electron tunneling through a double quantum dot: The artificial molecule. *Physical Review B*, 53(12):7899, 1996.

[56] Michael Scheibner, Allan S Bracker, Danny Kim, and Daniel Gammon. Essential concepts in the optical properties of quantum dot molecules. *Solid State Communications*, 149(35):1427–1435, 2009.

[57] M Ediger, PA Dalgarno, JM Smith, BD Gerardot, RJ Warburton, K Karrai, and PM Petroff. Controlled generation of neutral, negatively-charged and positively-charged excitons in the same single quantum dot. *Applied Physics Letters*, 86(21):211909, 2005.

[58] Nicolas H Bonadeo, John Erland, D Gammon, D Park, DS Katzer, and DG Steel. Coherent optical control of the quantum state of a single quantum dot. *Science*, 282(5393):1473–1476, 1998.

[59] MF Doty, JI Climente, M Korkusinski, M Scheibner, AS Bracker, P Hawrylak, and D Gammon. Antibonding ground states in inas quantum-dot molecules. *Physical review letters*, 102(4):047401, 2009.

[60] M Bayer, Pawel Hawrylak, K Hinzer, S Fafard, Marek Korkusinski, ZR Wasilewski, O Stern, and A Forchel. Coupling and entangling of quantum states in quantum dot molecules. *Science*, 291(5503):451–453, 2001.

[61] M Scheibner, M Yakes, AS Bracker, IV Ponomarev, MF Doty, CS Hellberg, LJ Whitman, TL Reinecke, and D Gammon. Optically mapping the electronic structure of coupled quantum dots. *Nature Physics*, 4(4):291–295, 2008.

[62] KP ODonnell and X Chen. Temperature dependence of semiconductor band gaps. *Applied physics letters*, 58(25):2924–2926, 1991.

[63] Yatendra Pal Varshni. Temperature dependence of the energy gap in semiconductors. *Physica*, 34(1):149–154, 1967.

[64] Henry Crew. Fact and theory in spectroscopy. *Science*, pages 1–12, 1907.

[65] M Moskovits and JE Hulse. Optical spectroscopy of copper clusters: Atom to bulk. *The Journal of Chemical Physics*, 67(9):4271–4278, 1977.

[66] Hyron Spinrad. Spectroscopic research on the major planets. *Applied Optics*, 3(2):181–186, 1964.

[67] R Heitz, I Mukhametzhanov, A Madhukar, A Hoffmann, and D Bimberg. Temperature dependent optical properties of self-organized inas/gaas quantum dots. *Journal of electronic materials*, 28(5):520–527, 1999.

[68] Savvas Germanis, Alexios Beveratos, George E Dialynas, George Deligeorgis, Pavlos G Savvidis, Zacharias Hatzopoulos, and Nikos T Pelekanos. Piezoelectric inas/gaas quantum dots with reduced fine-structure splitting for the generation of entangled photons. *Physical Review B*, 86(3):035323, 2012.

[69] Jeff A Valenti and Debra A Fischer. Spectroscopic properties of cool stars (spocs). i. 1040 f, g, and k dwarfs from keck, lick, and aat planet search programs. *The Astrophysical Journal Supplement Series*, 159(1):141, 2005.

[70] Brian Oetiker, Nebojsa Duric, John Mcgraw, Tom Williams, Dale Jackson, H-J Deeg, Michael Scheibner, M Tepper, D Garcia, and E Wilcox. Searching for companions to late type m stars. In *From Giant Planets to Cool Stars*, volume 212, page 88, 2000.

[71] Thomas Belhadj, Claire-Marie Simon, Thierry Amand, Pierre Renucci, Beatrice Chatel, Olivier Krebs, Aristide Lemaître, Paul Voisin, Xavier Marie, and Bernhard Urbaszek. Controlling the polarization eigenstate of a quantum dot exciton with light. *Physical review letters*, 103(8):086601, 2009.

[72] SM Ulrich, R Hafenbrak, MM Vogel, L Wang, A Rastelli, OG Schmidt, and P Michler. Control of single quantum dot emission characteristics and fine structure by lateral electric fields. *physica status solidi (b)*, 246(2):302–306, 2009.

[73] A Nick Vamivakas, C-Y Lu, C Matthiesen, Y Zhao, S Falt, A Badolato, and M Atature. Observation of spin-dependent quantum jumps via quantum dot resonance fluorescence. *Nature*, 467(7313):297–300, 2010.

[74] E Poem, J Shemesh, I Marderfeld, D Galushko, N Akopian, D Gershoni, BD Gerardot, A Badolato, and PM Petroff. Polarization sensitive spectroscopy of charged quantum dots. *Physical Review B*, 76(23):235304, 2007.

[75] Edward B Flagg, Andreas Muller, JW Robertson, Sebastien Founta, DG Deppe, Min Xiao, Wenquan Ma, GJ Salamo, and Chih-Kang Shih. Resonantly driven coherent oscillations in a solid-state quantum emitter. *Nature Physics*, 5(3):203–207, 2009.

[76] M Scheibner, G Bacher, A Forchel, T Passow, and D Hommel. Spin dynamics in cdse/znse quantum dots: Resonant versus nonresonant excitation. *Journal of superconductivity*, 16(2):395–398, 2003.

[77] Stefan Falt, Mete Atature, Hakan E Tureci, Yong Zhao, Antonio Badolato, and Atac Imamoglu. Strong electron-hole exchange in coherently coupled quantum dots. *Physical review letters*, 100(10):106401, 2008.

[78] AN Vamivakas, M Atature, J Dreiser, ST Yilmaz, A Badolato, AK Swan, BB Goldberg, A Imamoglu, and MS Unlu. Strong extinction of a far-field laser beam by a single quantum dot. *Nano letters*, 7(9):2892–2896, 2007.

[79] Edward D Palik. Gallium arsenide (gaas). *Handbook of optical constants of solids*, 1:429–443, 1985.

[80] Mark L Kerfoot, Alexander O Govorov, Cyprian Czarnocki, Davis Lu, Youstina N Gad, Allan S Bracker, Daniel Gammon, and Michael Scheibner. Optophononics with coupled quantum dots. *Nature communications*, 5, 2014.

[81] EA Stinaff, Swati Ramanathan, Kushal C Wijesundara, Mauricio Garrido, M Scheibner, AS Bracker, and D Gammon. Polarization dependent photoluminescence of charged quantum dot molecules. *physica status solidi (c)*, 5(7):2464–2468, 2008.

[82] F Jelezko and J Wrachtrup. Single defect centres in diamond: A review. *physica status solidi (a)*, 203(13):3207–3225, 2006.

[83] Marcus W Doherty, Neil B Manson, Paul Delaney, Fedor Jelezko, Jörg Wrachtrup, and Lloyd CL Hollenberg. The nitrogen-vacancy colour centre in diamond. *Physics Reports*, 528(1):1–45, 2013.

[84] Michael Scheibner, Sophia E Economou, Ilya V Ponomarev, Cameron Jennings, Allan S Bracker, and Daniel Gammon. Two-photon absorption by a quantum dot pair. *Physical Review B*, 2015.

[85] Wei Zhang, Alexander O Govorov, and Garnett W Bryant. Semiconductor-metal nanoparticle molecules: Hybrid excitons and the nonlinear fano effect. *Physical review letters*, 97(14):146804, 2006.

[86] M Kroner, AO Govorov, S Remi, B Biedermann, S Seidl, A Badolato, PM Petroff, W Zhang, R Barbour, BD Gerardot, et al. The nonlinear fano effect. *Nature*, 451(7176):311–314, 2008.

[87] A Christ, Y Ekinci, HH Solak, NA Gippius, SG Tikhodeev, and OJF Martin. Controlling the fano interference in a plasmonic lattice. *Physical Review B*, 76(20):201405, 2007.

[88] R Murray, RC Newman, RS Leigh, RB Beall, JJ Harris, MR Brozel, A Mohades-Kassai, and M Goulding. Fano profiles of absorption lines from the localised vibrational modes of be acceptors in gaas and b acceptors in silicon. *Semiconductor science and technology*, 4(6):423, 1989.

[89] J Kessler and J Lorenz. Experimental verification of the fano effect. *Physical Review Letters*, 24(3):87, 1970.

[90] Ugo Fano. Effects of configuration interaction on intensities and phase shifts. *Physical Review*, 124(6):1866, 1961.

[91] Uta Naether and Mario I Molina. Fano resonances in magnetic metamaterials. *Physical Review A*, 84(4):043808, 2011.

[92] Jin-Hui Wu, Jin-Yue Gao, Ji-Hua Xu, L Silvestri, M Artoni, GC La Rocca, and F Bassani. Ultrafast all optical switching via tunable fano interference. *Physical review letters*, 95(5):057401, 2005.

[93] Ennio Arimondo, Charles W Clark, and William C Martin. Colloquium: Ettore majorana and the birth of autoionization. *Reviews of Modern Physics*, 82(3):1947, 2010.

[94] ARP Rau. Perspectives on the fano resonance formula. *Physica Scripta*, 69(1):C10, 2004.

[95] Yong S Joe, Arkady M Satanin, and Chang Sub Kim. Classical analogy of fano resonances. *Physica Scripta*, 74(2):259, 2006.

[96] AA Clerk, X Waintal, and PW Brouwer. Fano resonances as a probe of phase coherence in quantum dots. *Physical review letters*, 86(20):4636, 2001.

[97] H Schmidt and A Imamoglu. Nonlinear optical devices based on a transparency in semiconductor intersubband transitions. *Optics communications*, 131(4-6):333–338, 1996.

[98] Jonathan P Marangos. Electromagnetically induced transparency. *Journal of Modern Optics*, 45(3):471–503, 1998.

[99] M Kroner, AO Govorov, S Remi, B Biedermann, S Seidl, A Badolato, PM Petroff, W Zhang, R Barbour, BD Gerardot, et al. The nonlinear fano effect. *Nature*, 451(7176):311, 2008.

[100] Boris Luk'yanchuk, Nikolay I Zheludev, Stefan A Maier, Naomi J Halas, Peter Nordlander, Harald Giessen, and Chong Tow Chong. The fano resonance in

plasmonic nanostructures and metamaterials. *Nature materials*, 9(9):707–715, 2010.

[101] M Scheibner, M Yakes, AS Bracker, IV Ponomarev, MF Doty, CS Hellberg, LJ Whitman, TL Reinecke, and D Gammon. Optically mapping the electronic structure of coupled quantum dots. *Nature Physics*, 4(4):291–295, 2008.

[102] R Heitz, A Kalburge, Q Xie, M Grundmann, P Chen, A Hoffmann, A Madhukar, and D Bimberg. Excited states and energy relaxation in stacked inas/gaas quantum dots. *Physical Review B*, 57(15):9050, 1998.

[103] Robert Heitz, Michael Veit, Nikolai N Ledentsov, Axel Hoffmann, Dieter Bimberg, Viktor M Ustinov, Petr Sergeevich Kopev, and Zh I Alferov. Energy relaxation by multiphonon processes in inas/gaas quantum dots. *Physical Review B*, 56(16):10435, 1997.

[104] Jason R Petta, Alexander Comstock Johnson, Jacob M Taylor, Edward A Laird, Amir Yacoby, Mikhail D Lukin, Charles M Marcus, Micah P Hanson, and Arthur C Gossard. Coherent manipulation of coupled electron spins in semiconductor quantum dots. *Science*, 309(5744):2180–2184, 2005.

[105] A Imamog, David D Awschalom, Guido Burkard, David P DiVincenzo, Daniel Loss, M Sherwin, A Small, et al. Quantum information processing using quantum dot spins and cavity qed. *Physical Review Letters*, 83(20):4204, 1999.

[106] Antonio Badolato, Kevin Hennessy, Mete Atature, Jan Dreiser, Evelyn Hu, Pierre M Petroff, and Atac Imamoglu. Deterministic coupling of single quantum dots to single nanocavity modes. *Science*, 308(5725):1158–1161, 2005.

[107] P Michler, A Kiraz, C Becher, WV Schoenfeld, PM Petroff, Lidong Zhang, E Hu, and A Imamoglu. A quantum dot single-photon turnstile device. *Science*, 290(5500):2282–2285, 2000.

[108] Miro Kroutvar, Yann Ducommun, Dominik Heiss, Max Bichler, Dieter Schuh, Gerhard Abstreiter, and Jonathan J Finley. Optically programmable electron

spin memory using semiconductor quantum dots. *Nature*, 432(7013):81–84, 2004.

[109] Xiaoqin Li, Yanwen Wu, Duncan Steel, D Gammon, TH Stievater, DS Katzer, D Park, C Piermarocchi, and LJ Sham. An all-optical quantum gate in a semiconductor quantum dot. *Science*, 301(5634):809–811, 2003.

[110] Daniel Loss and David P DiVincenzo. Quantum computation with quantum dots. *Physical Review A*, 57(1):120, 1998.

[111] Matthias Kuntz, Gerrit Fiol, Matthias Laemmlin, Christian Meuer, and Dieter Bimberg. High-speed mode-locked quantum-dot lasers and optical amplifiers. *Proceedings of the IEEE*, 95(9):1767–1778, 2007.

[112] Christian Meuer, Jungho Kim, Matthias Laemmlin, Sven Liebich, Gadi Eisenstein, Rene Bonk, Thomas Vallaitis, JÜrg Leuthold, Alexey Kovsh, Igor Krestnikov, et al. High-speed small-signal cross-gain modulation in quantum-dot semiconductor optical amplifiers at 1.3*mu* m. *IEEE Journal of Selected Topics in Quantum Electronics*, 15(3):749–756, 2009.

[113] Zhiliang Yuan, Beata E Kardynal, R Mark Stevenson, Andrew J Shields, Charlene J Lobo, Ken Cooper, Neil S Beattie, David A Ritchie, and Michael Pepper. Electrically driven single-photon source. *Science*, 295(5552):102–105, 2002.

[114] Christelle Monat, Blandine Alloing, Carl Zinoni, Lianhe H Li, and Andrea Fiore. Nanostructured current-confined single quantum dot light-emitting diode at 1300 nm. *Nano letters*, 6(7):1464–1467, 2006.

[115] Andrei Schliwa, Momme Winkelnkemper, Anatol Lochmann, Erik Stock, and Dieter Bimberg. In (ga) as/gaas quantum dots grown on a (111) surface as ideal sources of entangled photon pairs. *Physical Review B*, 80(16):161307, 2009.

[116] CL Salter, RM Stevenson, I Farrer, CA Nicoll, DA Ritchie, and AJ Shields. An entangled-light-emitting diode. *Nature*, 465(7298):594–597, 2010.

[117] Justin G Bohnet, Zilong Chen, Joshua M Weiner, Dominic Meiser, Murray J Holland, and James K Thompson. A steady-state superradiant laser with less than one intracavity photon. *Nature*, 484(7392):78–81, 2012.

[118] Michael Scheibner, Allan S Bracker, Danny Kim, and Daniel Gammon. Essential concepts in the optical properties of quantum dot molecules. *Solid State Communications*, 149(35):1427–1435, 2009.